

PETROLOGIC STUDY  
OF THE  
“CHILL” ZONE OF THE LAYERED SERIES AT DULUTH:  
TESTING A POSSIBLE PLUTONIC – VOLCANIC  
CORRELATION WITHIN THE MIDCONTINENT RIFT

A THESIS  
SUBMITTED TO THE FACULTY OF THE GRADUATE  
SCHOOL  
OF THE UNIVERSITY OF MINNESOTA  
BY

Sarah Kathleen Sauer

IN PARTIAL FULFILLMENT OF THE REQUIRMENTS  
FOR THE DEGREE OF  
MASTER OF SCIENCE

Advisor: James Miller

October 2015



© Sarah Kathleen Sauer 2015

## **Acknowledgments**

I would like to thank my advisor Dr. James Miller. Without his guidance, suggestions, edits and continued encouragement, this project would not have been possible. I would also like to thank Dr. John Goodge and Paul Siders for serving on my committee and providing critical feedback on the final drafts and with other hang-ups along the way.

Thanks also go to my friends and colleagues and the department faculty and staff for making my time at UMD a great experience.

Finally, thanks to my family, especially my mother and grandmother, for their continued love and support

## Abstract

The Duluth Complex is a multiple intrusive mafic complex that represents the largest exposed plutonic component of the 1.1 Ga Midcontinent rift. Results from extensive field mapping and petrologic studies (Miller and Green, 2008a, 2008b; Green and Miller, 2008) of the mafic cumulates comprising the type locality of the Duluth Complex at Duluth have confirmed that it is composed of two fundamentally distinct rock series, the Anorthositic Series (DAS) and the Layered Series at Duluth (DLS). The DAS had long been interpreted to be significantly older than the DLS based on the abundance of DAS inclusions in the DLS and, especially, on the occurrence of a fine-grained mafic rock that occurs at the sharp upper contact of the DLS with the overlying DAS, referred to as the DLS “chill”. However, high precision U-Pb ages from DAS and DLS samples (Paces and Miller, 1993) have shown that these two rock series are essentially identical in age within uncertainty ( $\pm 0.5$  Ma) at 1099 Ma relative to the 30 m.y. window of MCR magmatism.

Because the similar ages of the DLS and DAS preclude the DLS “chill” being a thermal quench of DLS parental magma against the DAS, Miller and Ripley (1997) and Miller (2011) have suggested that quenching of DLS magma was caused by the decompression of a volatile-saturated magma accompanying volcanic venting from the subvolcanic DLS chamber. Several features lend evidence in support of a decompression quenching of hydrous magma interpretation, including: 1) the evolved composition of the DLS “chill”, 2) the presence of biotite phenocrysts in the “chill”, and 3) the extensive hydrothermal alteration of overlying DAS rocks. It has been further suggested that periodic venting of hydrous magma may have played an important role in the formation

of the cyclic zone in the medial part of the DLS, particularly the occurrence of microgabbro cumulates in the upper parts of phase-layered macrocycles.

This study seeks to test the decompression quenching model proposed by Miller and Ripley (1996) and evaluate if the DLS “chill” composition is in equilibrium with the cyclic zone cumulates and whether possible volcanic products are represented in the North Shore Volcanic Group (NSVG) overlying the Duluth Complex. To accomplish this, the lithological, petrographic and geochemical attributes of the DLS “chill”, microgabbros and flows from the NSVG were evaluated. The chemostratigraphy of the overlying NSVG, documented in a previous study by Brannon (1984), provided the means to compare the DLS “chill” composition with eruptive products of the layered series. A suite of lavas was identified whose composition and position above the DLS (4.5-5 km) are consistent with being the volcanic products of volcanic venting from the DLS magma chamber.

To evaluate the comagmatic relationship between the DLS “chill” and cyclic zone microgabbros, the “chill” composition was applied to the MELTS based modeling program, PELE (Boudreau, 1999) to evaluate the equilibrium mineral phases of the “chill.” PELE was also used to determine oxidation state, water contents and simulate the proposed pressure fluctuations (devolatilization and venting) occurring with the DLS magma chamber. This study concludes the DLS chill formed by venting and decompressional quenching of hydrous roof zone magma. In addition, phase equilibrium modeling shows that cyclical pressure fluctuations caused by crystallization-driven volatile build-up and venting can also explain the macrocyclic cumulus phase layering and microgabbro intervals observed in the cyclic zone.

# TABLE OF CONTENTS

Acknowledgements.....	i
Abstract.....	ii
Table of Contents.....	iv
List of Figures.....	vi
List of Tables.....	ix
List of Appendices.....	x
<b>1. Introduction.....</b>	<b>1</b>
1.1 Geologic Setting.....	3
1.1.1 The Midcontinent Rift.....	4
1.1.2 North Shore Volcanic Group.....	10
1.1.3 Duluth Complex.....	12
1.1.4 The Layered Series at Duluth.....	15
1.2 Previous Studies of the Layered Series at Duluth.....	19
<b>2. Goals and Objectives of Study.....</b>	<b>25</b>
<b>3. Methods of Investigation.....</b>	<b>27</b>
3.1 Sampling.....	27
3.2 Petrography.....	29
3.3 Mineral Chemical Analysis.....	29
3.4 Lithogeochemical Analysis.....	30
3.5 Geochemical Modeling.....	30
<b>4. Results.....</b>	<b>31</b>
4.1 Petrographic Attributes of the DLS “Chill” and Related Rocks.....	31
4.1.1 DLS chill and related UCZ rocks.....	32
4.1.2 Cyclic zone microgabbro.....	44
4.1.3 North Shore Volcanic Group Basalt Flows.....	47
4.2 Mineral Chemistry.....	50
4.3 Whole-Rock Chemistry.....	53
4.4 Geochemical Modeling.....	59
<b>5. Discussion.....</b>	<b>65</b>

5.1 Petrologic Significance of the DLS “chill” .....	65
5.2 Volcanic Equivalents of the DLS chill.....	75
5.3 Evaluating the formation of the DLS chill by decompression of a volatile-saturated magma at low pressure.....	83
5.3.1 Evidence of water saturation in the DLS roof zone.....	84
5.3.2 Effects of decompression under water saturated conditions.....	86
5.3.3 Development of volatile saturated conditions in the DLS magma system.....	89
5.4 Correlation of the DLS Chill and DLS Cumulates.....	96
5.5 Formation of the cyclic zone.....	97
5.5.1. Phase and cryptic layering of the cyclic zone.....	98
5.5.2. Occurrence of anorthositic xenoliths in the cyclic zone.....	107
5.5.3. Significance of microgabbro cumulates.....	108
5.5 Proposed model for the origin of the DLS chill and cyclic zone.....	117
<b>6. Conclusions.....</b>	<b>121</b>
<b>References.....</b>	<b>122</b>



## List of Figures

Figure 1: Geology of the Midcontinent Rift around Lake Superior.....	5
Figure 2: Tectono-magmatic evolution of the Midcontinent Rift.....	8
Figure 3: Generalized Geology of the Duluth Complex.....	11
Figure 4: Geology of the Layered Series at Duluth.....	17
Figure 5: Field photograph of DLS “chill” against coarse-grained DAS rocks.....	22
Figure 6: Map of Upper Contact Zone sample sites.....	33
Figure 7: Photomicrographs of DLS chill.....	38
Figure 8: Photomicrographs of Category 2 rock types.....	40
Figure 9: Photomicrographs of Category 3 rock types.....	42
Figure 10. Photomicrographs of Category 4 rock types.....	43
Figure 11. Map of Cyclic Zone microgabbro sample sites.....	45
Figure 12. Photomicrographs of Cyclic Zone microgabbro.....	46
Figure 13. Map of North Shore Volcanic Group sample sites.....	48
Figure 14. Photomicrographs of North Shore Volcanic samples.....	49
Figure 15. Ternary diagram of En-Wo-Fs components in augite.....	51
Figure 16. Histograms displaying range in mg# in biotite in chill, microgabbro and gabbro zone.....	52
Figure 17. Histograms displaying range in Fo content in olivine in microgabbro and gabbro zone.....	53
Figure 18. Plot of Brannon’s data vs. SSV samples.....	55
Figure 19. Partition coefficients of REE between minerals and mafic magmas.....	56

Figure 20. DLS chill REE variation diagram (normalized to Chondrites).....	58
Figure 21. Upper contact zone REE variation diagram (normalized to Chondrites).....	58
Figure 22. Microgabbro REE variation diagram (normalized to Chondrites).....	59
Figure 23. Histograms displaying range in En' in augite in chill, microgabbro and Gabbro Zone.....	67
Figure 24. AFM diagram of Layered Series intrusions.....	70
Figure 25. Category 2 REE variation diagram (normalized to Chondrites).....	72
Figure 26. Category 3 REE variation diagram (normalized to Chondrites).....	73
Figure 27. Category 4 REE variation diagram (normalized to Chondrites).....	74
Figure 28. NSVG spider diagram (normalized to average chill).....	76
Figure 29. NSVG spider diagram (normalized to average chill).....	77
Figure 30. NSVG REE variation diagram (normalized to Chondrites).....	79
Figure 31. Trace element ratio diagram.....	80
Figure 32. Concentration of MgO vs. TiO <sub>2</sub> .....	81
Figure 33. Water – Albite diagram.....	87
Figure 34. Decompression experiments performed to verify the effects of water on the liquidus temperature.....	89
Figure 35. The solubility of water in basalt.....	93
Figure 36. Lithostatic decompression calculations.....	95
Figure 37. Histograms displaying mineral chemistries calculated by PELE.....	97
Figure 38. Geology of the cyclic zone of the DLS.....	99
Figure 39. Cyclic zone cryptic variation.....	101
Figure 40. Influence of pH <sub>2</sub> O on phase boundaries.....	104

Figure 41. Clinopyroxene stability with increasing pressure.....	106
Figure 42. Outcrop geology of macrocycle units within the cyclic zone.....	108
Figure 43. Photomicrograph and field photograph of microgabbro.....	109
Figure 44. Mass balance variation diagram.....	113
Figure 45. Histograms displaying mineral chemistries calculated by PELE.....	114
Figure 46. Histograms displaying mineral chemistries calculated by PELE.....	116
Figure 46. Proposed decompression quenching model.....	118

## **List of Tables**

Table 1: Locations, field descriptions and geologic settings of UCZ samples.....	34
Table 2: Petrographic attributes of samples collected from the UCZ.....	37
Table 3: PELE devolatilization and venting runs.....	62
Table 4: PELE mineral chemistries.....	64
Table 5: Whole rock lithochemical data for DLS “chill” .....	68

## **List of Appendices**

Appendix 1: Complete list of sampling locations.....	131
Appendix 2: SEM Mineral Analysis.....	132
Appendix 3: Whole rock data.....	147

## **1. Introduction**

The Mesoproterozoic 1.1 Ga Midcontinent Rift (MCR), when active, produced enormous amounts of intrusive and associated volcanic rocks. The aborted attempt at rifting of the MCR offers a unique opportunity to study potential comagmatic relationships between plutonic and volcanic systems, particularly in northeastern Minnesota where the Duluth Complex and related intrusions underlie 10 kilometers of similar-aged volcanics.

Previous studies of the Duluth Complex (Grout, 1918; Taylor, 1964; Phinney, 1972; Miller et al., 2002) noted distinct lithologic and structural differences between the two main lithodemic components of the Duluth Complex, the Anorthositic Series and the Layered Series. This led most early investigators to consider the Anorthositic Series to be petrogenetically and temporally distinct from the Layered Series (Weiblen and Morey, 1980; Miller and Weiblen, 1990). Supporting this interpretation is the consistent observation that inclusions of Anorthositic Series rocks commonly occur within Layered Series intrusions throughout the complex.

Seeming to support this interpretation in the type locality of the Duluth Complex in the Duluth area is the occurrence of a fine-grained mafic rock associated with the Layered Series at Duluth (DLS) that can be observed to sharply cut coarse-grained Anorthositic Series rocks. This fine-grained mafic rock (the DLS “chill”) was initially interpreted to represent thermal quenching of the Layered Series when it was emplaced into the cooler, older anorthositic rocks (Taylor, 1964). This interpretation was debunked, however, when Paces and Miller (1993) acquired coeval high-resolution U-Pb ages from zircons in Anorthositic and Layered Series rocks from two areas of the Duluth

Complex. This study showed that within the full 30 m.y. age range of MCR magmatic activity (1111 – 1086 Ma, Davis and Paces, 1990), the Anorthositic and Layered Series are essentially identical in age within uncertainty at 1099 Ma. This result was more recently confirmed by U–Pb age dating by Hoaglund (2011). This revelation, of similar ages, warranted a significant reinterpretation of the relationship between the two series, along with a reevaluation regarding the origin of the DLS “chill.” A closer look at the DLS “chill” shows it to be a compositionally evolved, biotitic ferrodiorite, and thus not primitive enough to be parental to the Layered Series (Miller and Ripley, 1996). Therefore, it must have formed late in the differentiation of the DLS.

A new interpretation, proposed by Miller (Miller and Ripley; 1996, Miller and Severson, 2002; Miller, 2011), suggests that the DLS “chill” is not the product of thermal quenching, but instead was formed by decompressional quenching of an evolved hydrous magma during volcanic venting events. Numerous features occurring within the Layered Series and Anorthositic Series lend evidence in support of this reinterpretation for quenching of a hydrous magma. These include: 1) the mineralogy of the DLS “chill” contains mineral assemblages stable under hydrous conditions; 2) the Anorthositic Series (DAS) overlying the Layered Series at Duluth (DLS) displays extensive hydrothermal alteration; 3) the “chill” bulk chemistry is in equilibrium with an evolved mineral assemblage of intermediate plagioclase, augite and Fe-Ti oxide, which is the assemblage found in the medial section of the well differentiated Layered Series at Duluth, termed the cyclic zone. This new interpretation of decompression quenching could explain the cyclic phase layering that characterizes the cyclic zone, as well as the occurrence of microgabbro cumulates that cap many of the cycles. Miller (2011) also speculated that

the “chill” composition may be found in volcanic units of the overlying NSVG, providing a petrologic link between intrusive and extrusive components of the MCR magma system.

This study seeks to revisit and re-evaluate these features in order to provide a better understanding of the origin of the DLS “chill” zone and its relationship to the magmatic evolution of the Layered Series at Duluth and to the overlying volcanic edifice. To accomplish this, petrographic observations and geochemical analyses (mineral chemistry, litho-geochemistry, and Sm-Nd isotopic chemistry) were conducted on DLS “chill” samples collected from numerous exposures in the Duluth Heights quadrangle (Miller and Green, 2008a) and the Duluth quadrangle (Green and Miller, 2008). In addition, the chemostratigraphy of the overlying NSVG was searched for compositions that match the DLS “chill” and thus may represent the eruptive products of the Layered Series. This task was made easier because of the efforts of Brannon (1984), who analyzed the geochemistry of 160 successive lava flows of the NSVG between 2 and 7 kilometers stratigraphically above the top of the Duluth Complex. Lastly, this study will rigorously test whether the cyclic zone cumulates of the Layered Series are in equilibrium with the DLS “chill” compositions. The “chill” compositions were applied to the program PELE (Boudreau, 1999) to determine the equilibrium liquidus phases, which were then compared to the phases and compositions of the cyclic zone.

### **1.1 Geologic Setting**

The Layered Series at Duluth (DLS) is the southernmost Layered Series intrusion of the Duluth Complex, which is a multiply-intruded mafic igneous complex occurring in northeastern Minnesota, and is the largest exposed plutonic component of the 1.1 Ga



Midcontinent Rift. The Duluth Complex and related intrusions were emplaced between Paleoproterozoic and Archean footwall rocks and lava flows forming the North Shore Volcanic Group. Described below is a brief summary of the general geologic features of the Midcontinent Rift, North Shore Volcanic Group and Duluth Complex.

### **1.1.1 The Midcontinent Rift**

The 1.1 Ga Midcontinent Rift (MCR) is one of the largest and best preserved examples of continental rifting due in large part to its failure to fully develop into an ocean basin. Exposure of the intrusive, volcanic and sedimentary rocks associated with the MCR are confined in the Lake Superior region (Fig. 1), but geophysical investigations have helped delineate the buried limbs of the rift, which extend from Lake Superior southwest to Kansas and southeast into Michigan, a total distance of more than 2,000 km. Active from 1115-1086 Ma, the MCR records a multi-stage history of extension and subsidence, voluminous magmatism, and sediment infilling (Hinze et al., 1992; Heaman et al., 2007; Miller and Nicholson, 2013).

Geophysical evidence in the form of seismic reflection data in the Lake Superior basin, along with gravity and magnetic anomalies, have revealed a robust image of the 3-dimensional structure and stratigraphy of the MCR (Hinze et al., 1997). Seismic reflection surveys show the rift basin reached depths of at least 30 km, allowing for the infilling of 20 kilometers of volcanic rocks overlain by 10 kilometers of sedimentary rocks (Hinze et al., 1997). Cannon (1992) estimated the total volume of rift-related volcanic rocks in the Lake Superior region to be  $\sim 2 \times 10^6 \text{ km}^3$ . In addition to this great thickness of rift volcanism, modeling of Bouguer gravity anomalies over the MCR in the

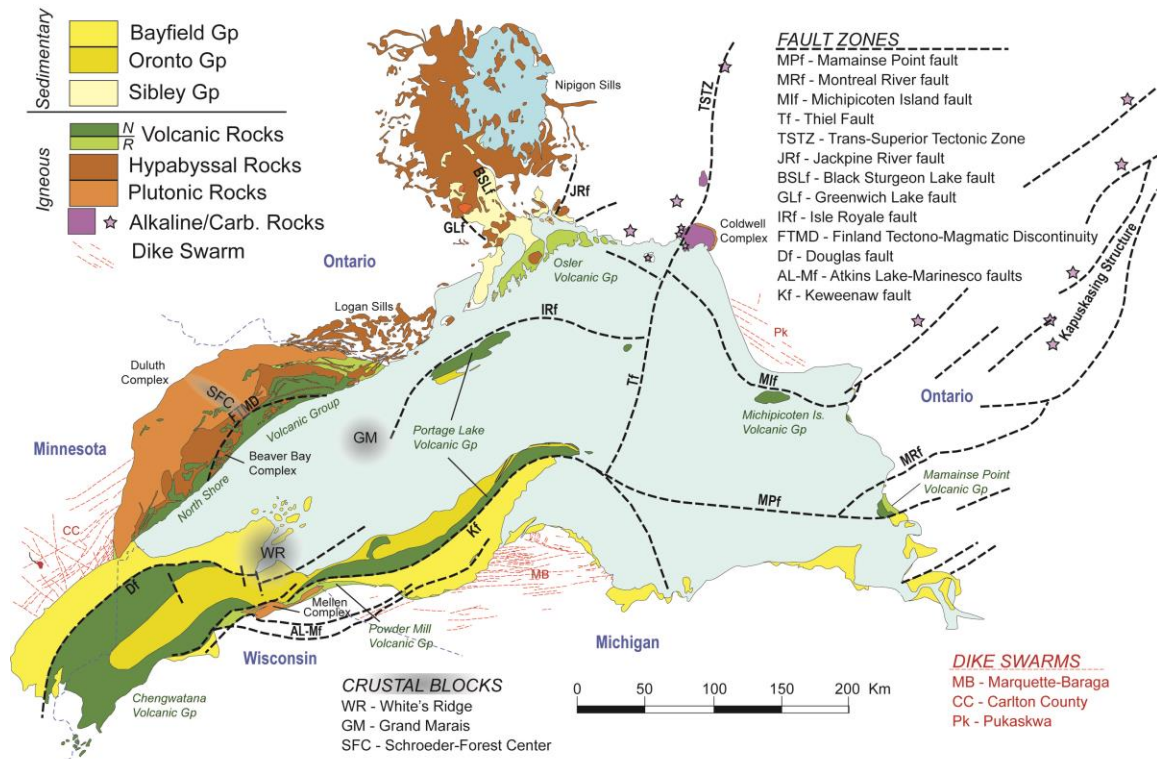


**Figure 1:** Geology of the Midcontinent Rift exposed in the Lake Superior region (from Miller and Nicholson, 2013).

Lake Superior area imply a significant volume of mafic rocks forming a 10-15 kilometer thick crustal underplate at the base of the rift zone (Trehu et al., 1991; Hinze et al., 1992).

Over the last 25 years, numerous studies have sought to define the catalyst for initiation of rifting along with the reason rifting was aborted. The extensive geological, geochemical and geophysical attributes of the Midcontinent Rift lend evidence supporting the widely held interpretation that the MCR was initiated by lithospheric extension driven by the head of a starting mantle plume (Hutchinson et al., 1990; Nicholson and Shirey, 1990; Cannon and Hinze, 1992; Nicholson et al., 1997). The main evidence in support of this model include the enormous volume of material erupted,

estimated to be more than 2 million km<sup>3</sup> (Cannon, 1992), along with an equivalent amount of magma that was underplated and intruded into the crust (Hinze et al., 1992). The large volume of mantle-derived flood basalts, generated by moderate extension, would require an anomalously hot mantle source, which would be explained by a starting mantle plume. Geochemical evidence from isotopic, major and trace element analysis of MCR related rocks indicate they were produced largely from an enriched mantle source which would be expected during plume-influenced rifting (Nicholson and Shirey, 1990; Lightfoot et al., 1991; Klewin and Shirey, 1992; Shirey et al., 1994; Shirey, 1997; Nicholson et al., 1997; Hollings et al., 2007 A and B). Nicholson and Shirey's (1990) isotopic study on tholeiitic basalts from the Portage Lake Volcanic rocks recorded consistently undepleted to enriched Sr, Nd and Pb isotopic signatures, which argue against lithospheric mantle as a source. Although the tectonomagmatic effects of the rising mantle plume are generally interpreted to have been responsible for crustal extension and subsequent generation of voluminous lava flows, Hollings et al. (2012) have questioned the role of a mantle plume.

Regardless of the mantle processes involved, geochronologic and geochemical data from volcanic and intrusive rocks indicate the frequency and duration of magmatism, as well as compositional characteristics, were not constant. This realization has led many to divide the magmatic activity of the MCR into several stages (Miller and Vervoort, 1996; Nicholson et al., 1997; Heaman et al., 2007; Vervoort et al., 2007). Miller and Nicholson (2013) recently proposed a six-stage tectono-magmatic model in order to reflect thermodynamic changes of the rising mantle plume and interactions between plume and surrounding lithosphere and continental crust, based on the observed geochemical,

geochronologic and structural attributes (Fig. 2). The following description of the MCR stages are taken from Miller and Nicholson (2013).

*Stage I (1115-1110 Ma) Initiation Stage* – This stage is characterized by ultramafic to mafic intrusions occurring in the Nipigon Embayment area. This stage also lacks volcanic rocks of similar age; in fact no volcanics related to the MCR have been dated to be older than  $1108 \pm 2$  Ma. However, it is speculated that 1115-1110 Ma-aged volcanics may exist but are buried beneath the Lake Superior basin. These intrusions have geochemical signatures indicative of an undepleted mantle derived from a deep source (Hollings et al., 2007a and 2007c). The arrival of a plume head would result in a large thermal anomaly resulting in uplift and crustal doming, which could explain the lack of similar-aged volcanics as they would be eroded during this period of crustal doming.

*Stage II (1110-1105 Ma) Early Stage* – This stage is represented by a period of reversed magnetic polarity and is characterized by voluminous eruption of initially primitive magmas followed by evolved and crustally contaminated mafic and felsic melts. This stage represents the impact of a mantle plume head into the base of a cool brittle lithosphere. The plume head rapidly heated the continental lithosphere causing the crust to thin, resulting in the voluminous eruptions of primitive, plume-derived magmas. Crustal staging of these primitive magmas gave way to evolved, crustally contaminated melts due to partial melting of the lower crust which is responsible for the generation of the felsic melts. Subsequently, melting of the lower crust generating felsic melts created a low density barrier prohibiting the rise of mantle derived melts, resulting in extensive mafic underplating.

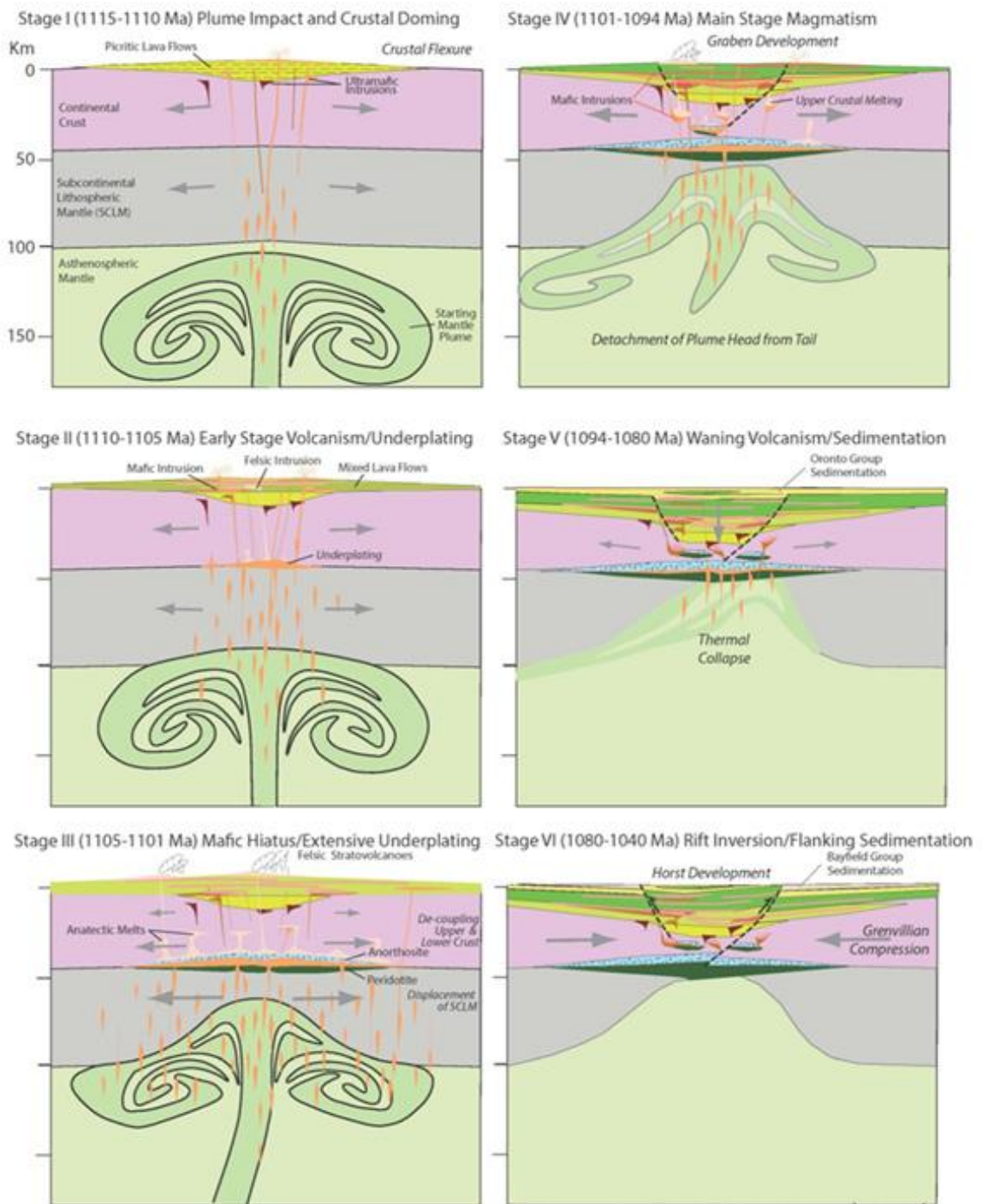


**Figure 2:** Tectono-magmatic evolution of the Midcontinent Rift (from Miller and Nicholson, 2013)

*Stage III (1105-1101 Ma) Hiatus Stage* – Stage three is characterized by a hiatus of mafic intrusive and volcanic activity except for localized felsic volcanism. Some vertical subsidence and graben-bounding faulting also occurred, based on observed deposits of high energy sediments. During this stage there was continued mantle plume activity, crustal melting and extensive crustal underplating. Felsic melts produced by partial melting of the lower crust created a rheological and density barrier which impeded the upward movement of mafic magmas, causing them to pond and form magma chambers. Mantle derived melts continued to rise and become trapped in lower crustal magma chambers, which resulted in more partial melting, trapping more mantle-derived magmas in a feedback system that prevented mafic magmas from traversing the crust for a 7 million year period.

*Stage IV (1101-1094 Ma) Main Stage* – During the main magmatic stage, magnetic polarity returned to normal conditions and mafic volcanic activity was once again initiated. Volcanic activity resulted in the production of nearly 10 kilometers of North Shore Volcanic Group lavas in Minnesota, and over 5 kilometers of Portage Lake Volcanics in Michigan. It also resulted in the emplacement of major intrusive complexes including the Beaver Bay and Duluth Complex. This stage is characterized by rapid to moderate eruption rates of uncontaminated, diverse magmas along with crustally derived felsic melts. This stage is thought to represent upper crustal separation, the evacuation of the crustal magma chambers, created during latent stage crustal underplating, along with waning mantle plume activity.

*Stage V (1094-1080 Ma) Late Stage* – The late magmatic stage represents a period of decreasing volcanic activity and subsidence of the rift basin. This stage is

characterized by the formation of evolved composite volcanoes with interbedded lava flows and basin sediments. The waning volcanic activity is thought to be caused by the overlying plate drifting away from the mantle plume heat source, which caused thermal collapse and sediment loading of the rift basin, which became filled with as much as 8 km of sediments.

*Stage VI (1080-1040 Ma)* – The final stage of the MCR is represented by compression and tectonic inversion. As the last volcanic eruptions were occurring, the area began to experience reverse faulting on originally normal faults, thought to be initiated by compression from the Grenville Orogen and resulting in 30 kilometers of shortening (Cannon, 1994). As the mantle plume continued to lose substantial mechanical and thermal energy, the compressional forces associated with the Grenville Orogeny overcame the crustal extension, effectively disabling the rift and preventing full separation (Cannon and Hinze, 1992).

Rocks formed during active periods of the MCR are exposed exclusively around Lake Superior and comprised of intrusive complexes, volcanic packages and sedimentary formations (Fig. 1). In northeastern Minnesota, the volcanic sequence is represented by the North Shore Volcanic Group which forms the hanging wall for the intrusive rocks of the Duluth Complex. (Fig. 3).

### **1.1.2 North Shore Volcanic Group**

Extending along the north shore of Lake Superior from Duluth to Grand Portage exists a 7-10 km thick package of mafic to felsic lava flows with interbedded sediments that comprise the North Shore Volcanic Group (NSVG; Fig. 3). The NSVG contains two “limbs” which dip shallowly (10-20°) toward the rift axis and arcs from a southerly dip in

its northeast limb and to an easterly dip in its southwestern limb. The two limbs vary slightly in thickness with the northeast limb containing a 7.2 km stack of volcanic rocks while the southwestern limb contains an approximate 9.7 km stack of volcanic rocks.

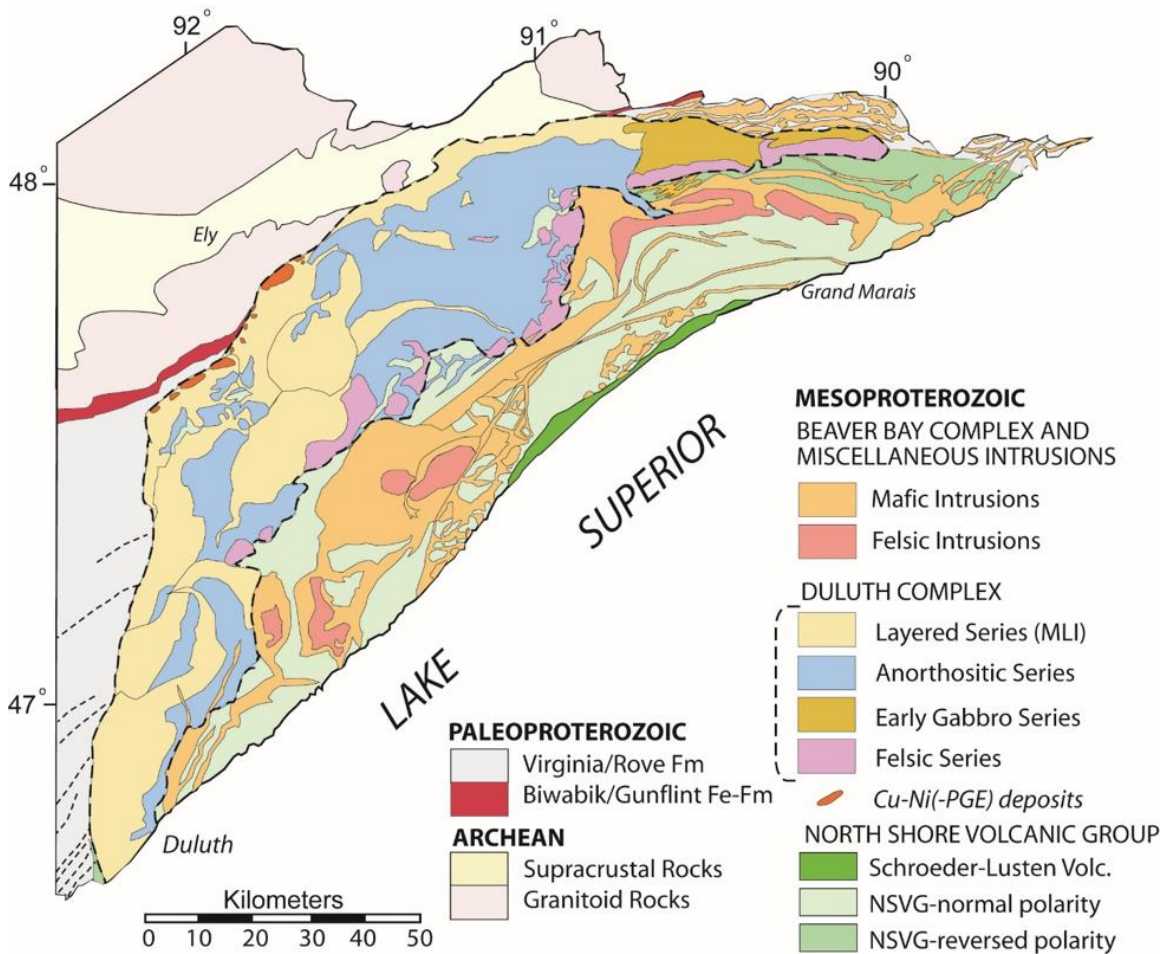


**Figure 3:** Geology of northeastern Minnesota showing the volcanic and intrusive components of the Midcontinent Rift (modified from Miller and Severson, 2002).



Compositionally, the NSVG contains tholeiitic to subalkalic lavas that follows a tholeiitic enrichment trend from primitive olivine tholeiite to rhyolite (Green, 2002). As with most of the rocks associated with the MCR, paleomagnetic polarity is used for correlation of rock units. Paleomagnetic reversals have been used to distinguish between upper and lower sequences (Fig. 3), but U-Pb dating has allowed for more precise correlation. These dates show that lower reversed polarity lavas erupted between 1109-1106 Ma, and that upper normal polarity lavas erupted between 1099-1094 Ma (Davis and Green, 1997).

### **1.1.3 Duluth Complex**

The Duluth Complex in northeastern Minnesota is a large multiply-intruded mafic igneous complex and is the largest exposed plutonic component of the 1.1 Ga Midcontinent Rift (Fig. 3). The Duluth Complex is typically divided into four general series based on age, lithology, internal structure and position (Miller and Severson, 2002). These series are the Felsic Series, Early Gabbro Series, Anorthositic Series, and Layered Series.

The Felsic Series is characterized by granophyric granite and rocks of intermediate composition that formed a semi-continuous mass of intrusions extending along the eastern and central roof zone (Fig. 3). A majority of the felsic series granophyre is homogenous, composed of reddish, micrographic leucogranite, typically with less than five percent mafic phases. Age dates along with contact relationship between the felsic series and other units suggest the felsic series was emplaced during the early magmatic stage of the MCR (1109 - 1106 Ma; Vervoort et al., 2007), making them the earliest intrusions of the Duluth Complex (Miller and Severson, 2002). Radiogenic isotopic data

from the granophyre indicate moderately negative  $\epsilon_{\text{Nd}}$  values (-0.5 to -3.7; Vervoort et al., 2007). This implies that felsic series magmas were likely generated from partial melting of early MCR related rocks or from partially melted early Proterozoic crust (Vervoort et al., 2007).

The Early Gabbro Series consists of layered oxide-rich gabbroic cumulates occurring along the northeastern contact of the Duluth Complex. Like the Felsic Series, the Early Gabbro Series was emplaced during early stage magmatism of the MCR ( $1106.9 \pm 0.6$  Ma; Paces and Miller, 1993). It is composed of two poorly studied mafic intrusive bodies, the Poplar Lake intrusion to the west (Nathan, 1969) and, the Crocodile Lake intrusion to the east (Babcock, 1959). The Early Gabbro Series resides stratigraphically below the felsic series and where exposed, the contacts between the two series are typically gradational and, less commonly, some chilling of the gabbro is observed. The similar age of the Early Gabbro and Felsic Series, along with the gradational contacts, suggest that the felsic series was emplaced first to create the Misquah Hills and Crocodile Lake granophyre bodies and, due to its low density, acted as a barrier which impeded the rise of gabbroic magmas of the Early Gabbro Series (Miller and Severson, 2002).

The Anorthositic Series was emplaced during main stage magmatism of the MCR (~1099 Ma; Paces and Miller, 1993; Hoaglund, 2010) and is a suite of structurally complex plagioclase rich gabbroic rocks. The average rock type is a coarse-grained, foliated, olivine gabbroic anorthosite to olivine leucogabbro (70-98% plagioclase) that forms a stratigraphic cap for most of the Duluth Complex. Although variations in plagioclase mode, mafic mineral proportions, olivine habit, and grain size can be discerned on a small (outcrop) scale, it is difficult to distinguish intrusive components on

a regional scale. The salient features of the Anorthositic Series are 1) its erratic internal structure defined by well-developed but variably oriented foliation, 2) the occurrence of various anorthositic lithologies in sharp, unchilled contact with other Anorthositic Series rock types, 3) variably zoned cumulus plagioclase, and 4) a lack of evidence for in-situ differentiation. Based on these observations, Miller and Weiblen (1990) proposed the Anorthositic Series formed by multiple intrusions of plagioclase crystal mush derived from lower crustal magma chambers during main stage magmatism (Fig. 2).

The Layered Series of the Duluth Complex is composed of at least eleven discrete, 1- 4 km-thick, sheet-like mafic layered intrusions that show a range of differentiated lithologies including dunite, troctolite, olivine oxide gabbro, apatite ferrogabbro, and ferromonzodiorite. These bodies typically exhibit igneous foliation and layering, which gradually dip southeastward toward the axis of the MCR. Most of the Layered Series intrusions occur between Anorthositic Series rocks and Paleoproterozoic and Archean footwall rocks, while a few intrusions were emplaced completely within the Anorthositic Series. Although cross-cutting relationships indicate that Layered Series intrusions are younger than the Anorthositic Series rocks (Fig. 3), U-Pb ages indicate near contemporaneity between the two series at 1099Ma (Paces and Miller, 1993; Hoaglund, 2010).

All Layered Series rocks display some degree of magmatic differentiation evidenced by phase layering of cumulate mineral assemblages and cryptic layering. Differences in the extent of differentiation among Layered Series intrusions can be attributed to degree of country rock assimilation, difference in parental magma composition, and frequency of magmatic recharge and venting events, along with the efficiency of fractional

crystallization (Miller and Ripley, 1996). The Layered Series at Duluth, which is the focus of this study, is one of the best-exposed and well-documented Layered Series intrusions, as will be described below.

#### **1.1.4 The Layered Series at Duluth**

The Layered Series at Duluth (DLS) is the southernmost Layered Series intrusion of the Duluth Complex and is comprised of a 3-4.5 km thick, well differentiated, stratiform sequence of troctolitic to gabbroic cumulates with an approximate 60 km north-south strike length and an average 25° easterly dip (Miller and Severson, 2002; Miller, 2011). The hanging wall to the DLS at Duluth is composed of olivine gabbroic and troctolitic anorthosite comprising the Anorthositic Series at Duluth (DAS). The footwall is composed of lowermost, reversed polarity NSVG lavas termed the Ely's Peak basalts. Based on lithology and stratigraphic position, the DLS can be divided into five major zones: basal contact, troctolitic, cyclic, gabbroic and upper contact (Fig. 4)

*Basal Contact Zone* – The lower 200-300 meters of the DLS consists of macrolayers (50-150 m thick) which grade from medium-grained, well-laminated troctolitic cumulates to coarse-grained, taxitic, ophitic olivine gabbro. The base of each macrocycle is typically defined by modally layered melatroctolite in sharp contact with the olivine gabbro below (Miller and Ripley, 1996; Miller, 2011). These macrolayers have been traced over 3-5 km along strike and are interpreted to be the result of cooling of the magma against the footwall producing the coarse olivine gabbro, followed by periodic recharge of a more primitive magma to produce the melatroctolitic rocks (Ross, 1985; Miller, 2011).

*Troctolite Zone* – This zone is characterized by a 1-1.5 km thick sequence of homogeneous, medium- to coarse-grained, moderately laminated, ophitic augite troctolite and troctolite. Locally, predominantly in the lower part of the zone, modal layering of cumulus olivine and plagioclase occurs, but is variable throughout the extent of the troctolitic zone. Other notable features of the troctolitic zone include the indiscriminate enrichment of augite oikocrysts (1-5 cm) and Fe-Ti oxide clots (<2 cm) up to as much as 15% through the zone along with minor and unsystematic cryptic variation in olivine and augite (Miller and Ripley, 1996; Miller and Severson, 2002).

*Cyclic Zone* – The medial section of the DLS is composed of a 1-km-thick interval distinguished by at least five, 50 to 200 m thick, cyclic variations in rock type which transition from two phase troctolitic (Pl+Ol) cumulates to three- to four-phase olivine oxide gabbroic cumulates (Pl+Cpx+Ox±Ol). The contacts between individual macrocycles are narrowly gradational to sharp, whereas within the macrocycle the contacts are more commonly gradational. Gabbroic anorthosite inclusions are commonly found at macrocycle boundaries, and also throughout the olivine oxide gabbro cumulate intervals. Another distinguishing feature of the cyclic zone is the occurrence of fine-grained, moderately laminated, intergranular oxide-olivine gabbro (microgabbro), commonly found just below macrocycle boundaries, with sharp to gradation contacts on a centimeter scale.

The base of the cyclic zone is marked by the gradation from medium-grained augite troctolite (troctolite zone), into a coarse-grained, poorly laminated subophitic to ophitic olivine gabbro. Transitions from subophitic olivine gabbro to a microgabbro

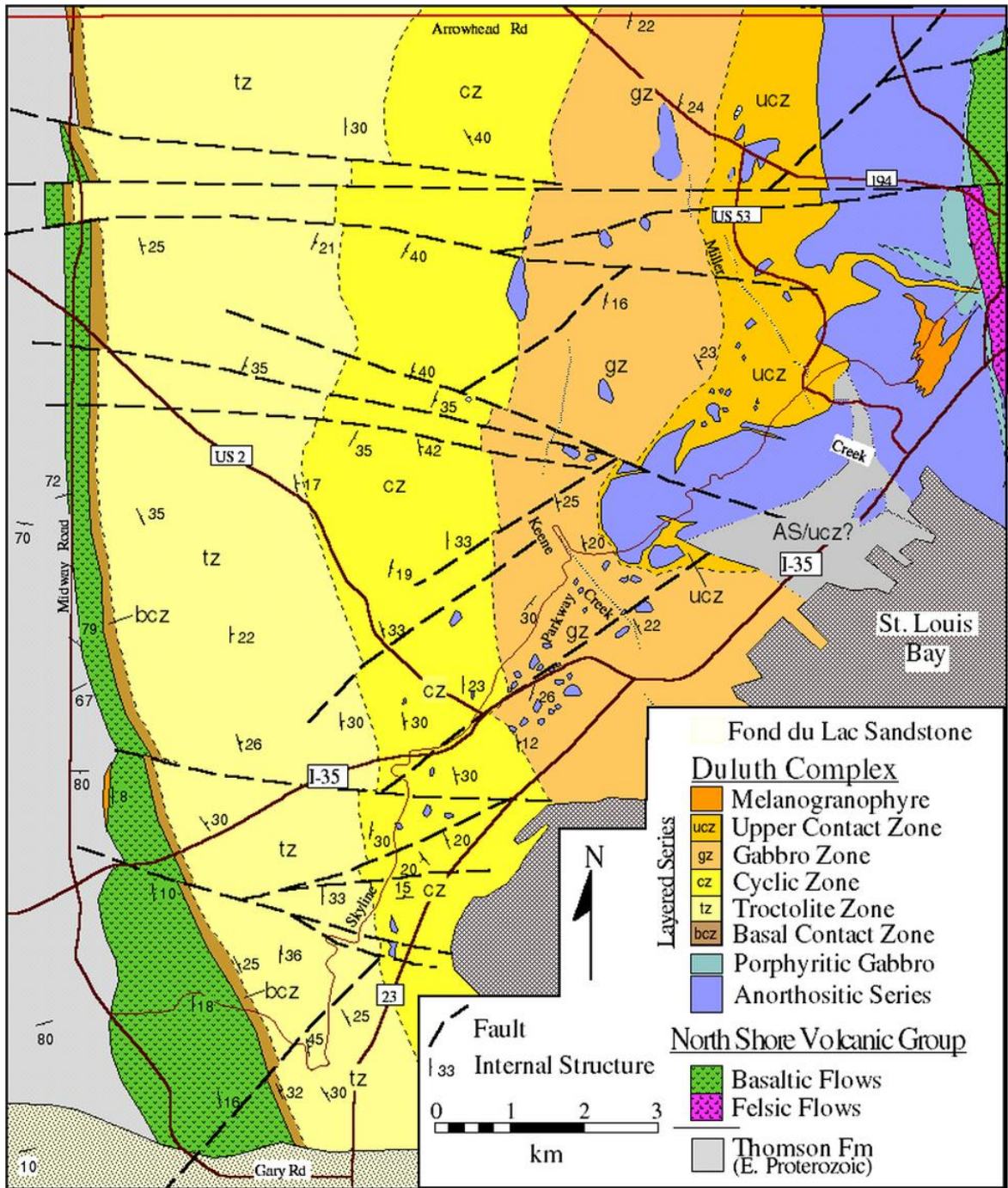


**Figure 4:** Geology of the Duluth Complex in the Duluth area (after Miller, 1995).

intermittently occur within medium-grained, well-laminated, intergranular olivine oxide gabbro. The top of macrocycle one is marked by the abrupt transition from the olivine oxide gabbro cumulate to a medium-grained, augite-poor troctolite cumulate leading into the second macrocycle. The lower portion of the second macrocycle is composed of homogeneous troctolitic cumulates. A 2-meter thick transition interval is distinguished by the abrupt appearance of subophitic augite and ilmenite clots, which grade into a well-laminated four-phase cumulate interval. As with macrocycle one, near the top of the four-phase cumulate interval exists a 2-10 m thick interval of microgabbro. The microgabbro of the second macrocycle is more laterally continuous, texturally homogeneous, olivine-rich, and locally enriched in Cu-Fe sulfide (~ 0.5%). The microgabbro grades upward from a fine-grained troctolite into a medium-grained ophitic augite troctolite which marks the transition into the third macrocycle. The upper three cycles are similar, characterized by troctolitic cumulates with abundant intercumulus augite and Fe-Ti oxide that abruptly grade upward into four-phase olivine oxide cumulates. Microgabbro intervals are also found marking the boundary between overlying macrocycles (Miller, 1995, 2011; Miller and Ripley, 1996).

*Gabbroic Zone* – This zone contains a 700-1200 m thick interval of medium-grained, poorly to well-laminated, intergranular oxide gabbro cumulate which may locally contain cumulus olivine, inverted pigeonite and/or apatite. The gabbroic zone commonly contains many DAS inclusions. Cryptic layering of solid solution minerals is significant in the gabbroic zone, varying by as much as 20 mole % in Fo and En content of olivine and augite. The contact between the gabbro zone and overlying

upper contact zone is defined approximately where obvious foliation in the gabbroic rocks is lost (Miller and Ripley, 1996).

*Upper Contact Zone* – The uppermost zone of the DLS contains hybridized non-cumulate mixtures of fine-grained biotitic ilmenite ferrodiorite, medium-grained apatitic quartz ferromonzodiorite, ferromonzonite and melanogranophyre. The ilmenite ferrodiorite is very fine to medium-grained, felty-textured and locally contains as much as 10% biotite which occurs as 3 to 5 mm clots. The fine-grained ferrodiorite typically occurs directly in sharp contact with coarse-grained DAS rocks, and was previously interpreted to be the chill of the DLS parent magma (Grout, 1918b; Taylor, 1964). However, as mentioned previously, U-Pb age dating shows that the DAS and DLS are irresolvable in age.

In some locations near the upper contact with the DAS, the fine-grained ferrodiorite (hereafter referred to as the DLS chill) is irregularly mixed with masses of medium-grained melanogranophyre along sharp lobate contacts. This has been interpreted by Miller (1995; 2011) to represent incomplete mixing of mafic and felsic magmas due to their highly contrasting viscosities in the roof zone of the DLS. Elsewhere in the upper contact zone, the fine-grained ferrodiorite has been observed to be cross-cut by more evolved compositions of ferromonzodiorite to ferromonzonite (Miller and Ripley, 1996).

## **1.2 Previous Studies of the Layered Series at Duluth**

Geologic interest of the Duluth Complex has existed since 1872 when, headed by geologist N.H. Winchell, the Minnesota geological and natural history survey began detailed mapping of the area. As a result, the first reconnaissance-scale geologic maps



were created which defined the framework of the Duluth Complex and distinguished the basic felsic and mafic rock types in the area (Winchell, 1900).

It was later, during the early part of the 1900's, through the pioneering efforts of Frank Grout, that a major understanding of the Duluth Complex was established. In 1918 Grout published five papers (Grout, 1918 a-e) with the focus to address and define the physical and chemical processes associated with the intrusive igneous rocks of the Duluth Complex at Duluth. Through his studies Grout recognized igneous processes such as convection in magmas, crystal settling and filter pressing; mechanisms which he used to explain the occurrence of igneous structures and features such as fluxion structure, modal layering, or banding, and differentiated rock types (Grout 1918c, d). Despite interpreting the Duluth Complex to be a continuous intrusion defining the classic shape of a lopolith, which has since been disproven, he did recognize that the complex is composed of two distinct mafic suites of rock, a feldspathic gabbro and a main, or banded, gabbro. From observations of the DLS "chill" against coarse-grained DAS rocks (Fig. 5), Grout inferred a distinct temporal relationship, stating " At Duluth, it is evident that a feldspathic gabbro was intruded and cooled before the main mass of more basic gabbro was intruded" (Grout 1918e, p. 627).

Further geologic understanding of the Duluth Complex at Duluth was established in the mid-1950's from the work completed by Richard Taylor (Taylor, 1959). Taylor's field work, petrographic descriptions, geochemical characterization and petrologic interpretation of the Duluth Complex in the Duluth area further defined the two distinctive rock series first recognized by Grout (1918d). His work was summarized in a Minnesota Geological Survey Bulletin (Taylor, 1964), which included the first color,

detailed (1:48,000 scale) bedrock geologic map of the type locality of the Duluth Complex at Duluth (MGS Miscellaneous Map 1). Taylor (defined the two rock types as the anorthositic gabbro (Grout's feldspathic gabbro) and the Layered Series (Grout's main gabbro). Within the anorthositic gabbro, Taylor noticed the common occurrence of inclusions of anorthositic rocks within other anorthositic rocks, equating the appearance to that of an igneous breccia. He also noted well developed igneous lamination along with the mineralogical and textural variability and concluded the origin of the anorthositic gabbro to have been due to multiple intrusions of a plagioclase crystal mush.

Within the Layered Series (Grout's main gabbro), Taylor further recognized internal structures such as rhythmic layering, gravity stratification and fluxion structures, which he attributed to upward fractional crystallization in an environment of active magmatic convection. He also noted only minor cryptic variation, which he cited as of evidence of magmatic recharge into the magma chamber. As with Grout (1918 b), Taylor (1964) interpreted the gabbroic rocks (now the Anorthositic Series and Layered Series) to have formed during different times. Taylor noted "The gabbroic rocks were formed in two major periods of intrusions that were sufficiently separated in time for the older gabbro to have become cold before intrusion of the younger gabbro" (Taylor 1964, p. 8).

While Grout's (1918) and Taylor's (1964) interpretation of the DLS "chill" (Fig. 5) as a thermal quench prompted the interpretation that the Anorthositic Series is significantly older than the Layered Series, this interpretation was reinforced by field



**Figure 5:** Outcrop of the DLS “chill” (fine-grained ilmenite ferrodiorite) cutting coarse-grained anorthositic series rocks (DAS) with irregular masses of granophyre in a road cut on Skyline Parkway in Duluth (UTM (NAD83) – 564888N/5179669E; photo from Jim Miller).

mapping and petrologic studies in other areas of the Duluth Complex. Mapping studies by Phinney, Davidson, Bonnicksen and Weiblen, which were summarized in contributions to the Minnesota Geological Survey's Centennial Volume in 1972 consistently noted the distinct lithological and structural attributes of the Anorthositic and Layered Series and recognized that Anorthositic Series inclusions routinely occur in Layered Series intrusions, with the opposite being rarely observed. As implied by models proposed by Wieblen and Morey (1980) and Miller and Weiblen (1990) for the emplacement history of the Duluth Complex, the notion that the Anorthositic Series was significantly older than the Layered Series was a well-accepted paradigm for the Duluth Complex. However, the acquisition of precise U-Pb zircon ages by Paces and Miller (1993) compelled a paradigm shift when it revealed that the two series are effectively identical in age at  $1099 \pm 0.5$  Ma (a fact later confirmed by Hoaglund, 2010).

The contemporaneity of the two series not only compelled a reevaluation of the genesis of these two distinctive suites, with the possibility that they may be genetically linked, but it also compelled a reevaluation of the significance of the DLS chill. For the DLS chill to have formed due to thermal quenching would require 1) that the Anorthositic Series had cooled significantly before emplacement of the Layered Series, all of which would need to have happened within less than one million years, and 2) that the composition of the DLS chill is parental to the DLS, in other words would be capable of generating the entirety of the Layered Series through fractional crystallization. The first requirement is theoretically possible given the shallow crustal setting of the Duluth Complex. However, a cursory petrographic and geochemical examination of the DLS chill following on a mapping study in the Duluth area begun by Miller and Green in 1992

(maps published in 2008 – Miller and Green, 2008a,2008b, and Green and Miller, 2008) showed the chill to be a fine-grained, intergranular, biotitic ilmenite ferrodiorite that is compositionally an evolved high-Ti, ferro-basalt. It is clear that this rock is mineralogically and geochemically too evolved to be parental magma to the Layered Series (Miller and Ripley, 1996).

As an alternative interpretation, Miller (1993, 1995, 2011; Miller and Ripley, 1997) has proposed that the quenching of the DLS chill resulted from devolatilization and decompression attending magma venting events. He further suggested that such a process could also explain the macrocyclical phase layering of the DLS cyclic zone and the occurrence of microgabbro cumulates at the tops of macrocyclic intervals. A decompression-quench model better explains the similar ages between the DAS and DLS and the evolved composition of the chill. This model can also be used to explain the compositional and textural changes and the occurrence of anorthositic inclusions within the cyclic zone along with the microgabbro intervals found at the top of each macrocycle.

One hypothesis for the formation of the cyclic zone and the observed transition from two-phase, troctolitic cumulates (PO) to four phase gabbroic cumulates (PCFO) followed by the abrupt regression back to troctolitic cumulates is due to normal fractional crystallization with periods of magmatic recharge. However, the lack of consistent systematic cryptic variation in mineral chemistry argues against both of these and suggests other processes played a role in the development of the cyclic zone. Instead the cyclic zone is better explained by the combined effects of fractional crystallization, over-pressurization and magmatic venting followed by re-pressurization of the magma

chamber (Miller 1993, 1995, 2011a, 2011b; Miller and Ripley, 1996; Miller and Severson, 2002).

In 1984, Joyce Brannon documented the petrography and analyzed the geochemistry of successive lava flows of the NSVG up section of the Duluth Complex. The purpose of Brannon's (1984) study was to evaluate and determine whether the chemical variability within this genetically related, compositionally varied volcanic suite can be attributed to partial melting of multiple mantle sources or to fractional crystallization of a single parent magma. Brannon chose the NSVG based on: 1) the compositional variation which ranges from primitive olivine tholeiite to rhyolite as documented by Green (1972); 2) the flows are exposed along the north shore of Lake Superior and accessible in stratigraphic order; 3) the ability to sample different regions from individual flows, making it possible to document heterogeneity within single flows; and 4) alteration being minor for most flows. As a result, Brannon analyzed the geochemistry of 160 successive lava flows of the NSVG between 2 and 7 kilometers stratigraphically above the top of the Duluth Complex. Given the proposed model cited above that the DLS chill formed by decompressional quenching of a hydrous magma during venting events, it raises the question as to whether the chill composition could be found in the NSVG which lies conformably over the Duluth Complex at Duluth.

## **2. Goals and Objectives of Study**

The goal of this study is to evaluate the potential comagmatic relationship between plutonic and volcanic systems associated with the 1.1 Ga Midcontinent Rift, specifically testing the model proposed by Miller (Miller and Ripley, 1996; Miller and Severson,

2002; Miller, 2011, 2012) regarding the origin of the fine-grained mafic rock occurring in the upper contact zone of the Layered Series at Duluth (DLS chill). As mentioned above, this model hypothesizes that the DLS chill was not produced by thermal quenching, but rather formed by decompression quenching of an evolved hydrous magma during a volcanic venting event. Furthermore, this model suggests that the decompression attending magma venting was responsible for the phase layering that characterizes the cyclic zone. Another implication of this model is that if this composition can be linked to a flow or package of flows overlying the Duluth Complex, it will give an estimate to the depth of emplacement for the DLS within the volcanic edifice of the NSVG.

The specific objectives of this study that will test this model are:

- 1) Characterize the lithological, petrographic, and geochemical attributes of the DLS chill in numerous exposures mapped by in the Duluth Heights quadrangle and the Duluth quadrangle.
- 2) Use Brannon's (1984) geochemical data as an initial guide to search the chemostratigraphy of the NSVG occurring above the Duluth Complex at Duluth for compositions matching the DLS chill. Flows that seem to show a good match to the DLS chill composition will be reanalyzed by the same analytical protocols compared to the lithologic, petrographic and geochemical attributes of the DLS chill.
- 3) Determine the phase equilibrium of the DLS chill using PELE (Boudreau, 1999), a modified version of MELTS (Ghiorso and Sacks, 1995). This will be used to establish the degree to which the chill was water-saturated, the effect of pressure change on that composition, and to evaluate whether the chill is in equilibrium with

cyclic zone cumulates, particularly microgabbros, or perhaps the more evolved gabbro zone cumulates.

### **3. Methods of Investigation**

In order to accomplish the objectives outlined above, several methods of investigation were employed in order to characterize this comagmatic, plutonic-volcanic system. The analytical methods used include petrographic observation, lithochemical analysis, and mineral chemistry of samples collected from the DLS chill, the cyclic zone cumulates, and select NSVG samples. In addition, geochemical modeling using the modeling program PELE (Boudreau, 1999) were also applied to the geochemical data.

#### **3.1 Sampling**

A total of 37 samples were collected at numerous exposures previously mapped by Green and Miller in the West Duluth, Duluth Heights and Duluth 7.5' quadrangles (Miller and Green, 2008; Green and Miller, 2008). Within the Duluth Complex, 22 samples were collected from the DLS chill and related upper contact zone rocks, 13 samples from the microgabbro occurrences within the cyclic zone and two samples of granophyre (found in contact with the chill and Anorthositic series). Data compiled by Miller, which included field and petrographic descriptions from sample sites within the West Duluth, Duluth Heights and Duluth quadrangles, were reviewed for descriptions closely resembling the chill (fine- medium fine-grained, biotite  $\pm$  hornblende ferrodiorite/gabbronorite) in order to determine potential sampling locations. ArcGIS was used to plot outcrop locations and sample sites. In total, 23 samples were collected from 14 sites, which resembled the chill and spanned the lateral extent of the upper contact



zone (UCZ). The same selection process was used when selecting microgabbro sample sites. A number of samples previously collected by Miller and Green (2008a & b), which were also studied in thin section and geochemically analyzed, were also incorporated in this study.

In addition to the chill and microgabbros, seven samples from the overlying NSVG were collected that geochemically resemble the DLS chill. In order to find flows from the NSVG, geochemical data from 160 successive lava flows collect by Brannon (1984) were normalized to the average chill composition, previously reported by Miller and Ripley (1996), and plotted on spider diagrams. As will be shown below, two series of flows (Brannon's flows 28-38 and 58-65) were identified that showed the best fit for most major and trace elements, particularly flow 28 and 65. Notably, flow 65 not only shows a good fit to the chill composition, but also is the upper-most flow of an 8 flow sequence which defines a progressively evolved differentiation cycle (flows 58-65).

Given these compositional similarities, new samples from Brannon's (1984) flows 28-38 and 58-65 were collected for reanalysis for this study. Using inset maps sketched by Brannon along with utilizing detailed geologic maps of the French River, Lakewood and Knife River 7.5' quadrangles (Boerboom et al., 2002), samples were collected from the massive interiors in order to avoid amygdaloidal flow tops and bottoms. Unfortunately, complete sampling from flow sequence 58-65 was not possible due to poor shoreline exposure and recent construction of a harbor at Knife River, which obstructed most of the sequence. Only flows 64 and 65 of this sequence could be re-sampled. A complete resampling of flows 28-38 was also not possible due to poor exposure or the inability to collect a sample without significant amygdules. It should be

noted there is slight uncertainty regarding the actual flow sampled. Sampling locations for selected flows were determined using inset maps which were sketched by Brannon and though these maps delineated individual flow boundaries, Brannon's exact sampling locations are unknown.

### **3.2 Petrography**

All 43 samples collected from the DLS chill, upper contact zone, cyclic zone microgabbro intervals, and selected flows from the NSVG were cut into billets at UMD and made into polished thin sections by Quality Thin Sections of Tucson, Arizona. Transmitted-light petrographic observations of these sections were conducted using Leica DM microscopes in the UMD microscopy lab. Petrographic observations helped to refine and better characterize mineralogy, textures, and alteration not obvious in hand samples. Petrographic attributes recorded for each thin section included modal mineralogy of primary and secondary phases, grain size, mineral habit, zoning, exsolution, the extent and nature of alteration and other notable features. Photomicrographs were taken to document the various mineralogic and textural attributes of the samples.

### **3.3 Mineral Chemical Analysis**

Mineral chemistry of selected samples was analyzed at UMD Scanning Electron Microscopy Laboratory using the JEOL JSM-6490LV scanning electron microscope and Oxford Inca 250 energy dispersive X-ray spectroscopy (EDS). Polished thin sections were coated with a ~ 15-20 nm thick carbon film to prevent the sample from charging. Over 600 separate analyses were collected from 24 polished thin section samples. Analyses focused primarily on pyroxene since it is the one mineral existing in each suite of samples (chill, MG and NSVG). Analysis of olivine (within microgabbro), plagioclase,

and biotite was also conducted to compare compositions with preexisting mineral chemical analysis obtained by Miller and compositions determined from geochemical modeling. Typically for each thin section, 12 analyses were obtained for pyroxene, 5 for olivine and 1-5 analyses for biotite. Plagioclase, being significantly zoned, was not rigorously analyzed due to difficulties in acquiring enough analyses to generate a statistically valid average composition.

### **3.4 Lithochemical Analysis**

A total of 37 samples were submitted to Acme Laboratories of Vancouver, British Columbia for lithochemical analysis. Rock samples were submitted for crushing and pulverizing of approximately 1 kilogram samples using PRP70-250 sample preparation. Analyses were completed from a 0.2 kilogram sample by ICP-emission spectrometry following a metaborate/tetraborate fusion and dilute nitric digestion.

The entire suite of collected samples from the chill, microgabbro and overlying NSVG were selected for analysis. Lithochemical compositions, especially incompatible trace elements, can be used to define similarities and differences and evaluate comagmatism between the DLS chill and the cyclic zone microgabbro and between the DLS chill and possible eruptive equivalents in the NSVG.

### **3.5 Geochemical Modeling**

Geochemical modeling was conducted using the program PELE, which is a modified version of the MELTS software program for the PC platform developed by Boudreau (1999). PELE was used to determine the concentration of volatiles ( $H_2O$  and  $CO_2$ ) at saturation in the DLS chill, the effect of pressure changes on the phase equilibrium of such a saturated composition, and the cumulus mineral phases in equilibrium with the

DLS chill composition. PELE is capable of modeling the phase equilibrium of natural magmatic compositions at a range of temperatures (900°C-1700°C), oxygen fugacity conditions, and pressures up to 4 GPa which can be used to predict processes such as equilibrium or fractional crystallization and the degassing of volatiles (Ghiorso and Sack, 1995). Necessary input parameters for PELE include: major oxide wt.%, starting temperature and pressure, stopping temperature and pressure, and oxygen fugacity conditions. Once all parameters have been inserted, different commands within PELE can be used to find the liquidus temperature for the given bulk composition along with computing redox conditions based on specified oxygen fugacity and water saturation for the given bulk composition. Sample MD279A was chosen as the input for the bulk composition and calculations were run simulating equilibrium crystallization under differing QFM oxidation conditions.

## **4. Results**

### **4.1 Petrographic Attributes of the DLS “Chill” and Related Rocks**

Reported here are the detailed petrographic descriptions of samples that comprise the DLS chill and related upper contact zone rocks, cyclic zone microgabbro intervals, and selected flows from the overlying NSVG. In each sample, primary mineral mode, habit, texture and alteration were described from thin section. Samples were assigned a modal rock name based on visually estimated modal abundances, and using the classification nomenclature recommended by Miller et al. (2002). Terminology for mineral habit, grain size, zoning, exsolution and other petrographic attributes follow the definitions given by Bates and Jackson (1987).

#### **4.1.1 DLS “Chill” and Other UCZ Rocks**

As mentioned previously, sampling sites of the DLS chill spanning the lateral extent of the UCZ were identified based on field and petrographic descriptions digitally archived in ArcGIS during mapping of the Duluth Heights 7.5' quadrangle by Miller and Green (2008b). Samples were sought where field descriptions consistently reported the occurrence of a fine-grained mafic rock in the UCZ near a contact with the Anorthositic Series. A total of twenty-two samples were collected from the UCZ that fit this description. Figure 6 shows their locations and descriptions of their location, field occurrence, and geological setting are given in Table 1.



**Table 1:** Locations, field descriptions and distance from Anorthositic Series contact of samples collected from the UCZ.

Sample	UTM Location (N/E)	Field Description	Distance to AS contact (meters)
SSC1A	565415/5181145	Fine-grained, subprismatic mafic rock with 1-2mm biotite phenocrysts	~ 450
SSC1B	565424/5181127	Fine-grained, subprismatic mafic rock with 1-2mm biotite phenocrysts and ~5mm bladed oxide crystals	~ 490
SSC1C	565447/5181119	Fine-grained, mafic rock with 1-2mm biotite phenocrysts and ~5mm bladed oxide crystals; possible qtz.	~ 525
SSC1D	565443/5181128	Fine-grained, quartz-bearing, mafic rock with 1-2mm biotite phenocrysts with granophyre inclusions	~ 540
SSC2A	564919/5181675	Medium fine – medium-grained, felty ferrodiorite (?) with $\leq 1$ mm biotite crystals	~ 980
SSC2B	564952/5181647	Medium fine-grained felty, apatite-bearing ferrodiorite (?) with $\leq 1$ mm biotite crystals	~ 950
SSC3A	565697/5180055	Fine-grained mafic rock with small ( $\leq 1$ mm) biotite crystals intermingled with granophyre	~ 30 from DAS block; ~ 240 from main DAS
SSC3B	565577/5180134	Fine-grained mafic rock with small ( $\leq 1$ mm) biotite crystals, bladed oxide, possible quartz	~ 125 from DAS block; ~ 325 from main DAS
SSC3C	565474/5180916	Fine-grained mafic rock with small ( $\leq 1$ mm) biotite crystals, possible qtz; intermingled with granophyre.	~ 225 from DAS block; ~ 380 from main DAS
SSC4	565864/5181518	Fine-grained, homogenous, biotite-phyric ( $\leq 2$ mm), apatitic(?) ferrodiorite intermingled w/ granophyre	~ 30
SSC5	564888/5179669	Very fine-fine-grained, plagioclase-(2-3mm) and biotite-(1-2mm) phyric mafic rock intermingled with granophyre; in sharp contact w/ crs gabbroic anorthosite.	at contact

**Table 1:** continued

Sample	UTM Location (N/E)	Field Description	Distance to AS contact (meters)
SSC6	563428/5178427	Fine-grained granular rock. Fine-grained olivine gabbro (?)	~ 25
SSC7	564540/5182438	Fine- to medium fine-grained, plagioclase- and biotite- ( $\leq 3$ mm) phyric ferrodiorite (?) with trace sulfide minerals	~ 1150
SSC8	564451/5184011	Fine-grained mafic rock in contact with crs-grained olivine gabbro	~ 900
SSC9A	564864/5183915	Fine-grained, plagioclase- and biotite-phyric mafic rock	~ 550
SSC9B	564950/5183890	Medium fine-grained, intergranular, biotitic mafic rock near contact with gabbroic inclusion (?)	~ 475
SSC9C	564971/5183973	Medium fine-grained, biotitic mafic rock with trace sulfide minerals.	~ 380
SSC10A	563099/5179317	Fine- to medium fine-grained, biotite-phyric (1-2mm) ferrodiorite with trace sulfide minerals.	~ 125
SSC10B	563116/5179292	Very fine-grained, biotite-phyric ferrodiorite	~ 100
SSC10C	563073/5179336	Fine-grained biotite-phyric ferrodiorite with 1-2 cm pods of medium crs-grained gabbro.	~ 25
SSC11	563632/5179280	Very fine-grained, biotite-phyric mafic rock	~ 65
SSC12	563596/5179310	Very fine-grained, biotite-phyric (~2mm) mafic rock near contact with crs-grained olivine gabbro.	In contact



Petrographic observations reveal that the twenty-two samples collected are not uniform in mineralogy and texture, and that only a limited number resembled the type-DLS chill. As summarized in Table 2, the UCZ rock samples collected for this study fall into four general mineralogic/textural categories. Eight samples (SSC1A/1C, 3A/B, 4, 5, 11 and 12) display petrographic attributes that most closely resemble the type-DLS chill and are assigned to in Category 1. These samples are typically fine-grained, intergranular, biotitic ilmenite  $\pm$  hornblende-bearing ferrodiorite/gabbronorite (Fig. 7). Modally, they are composed of 50-60% plagioclase, 15-30% clinopyroxene, 5-15% orthopyroxene (inverted pigeonite) and 3-10% biotite (both primary and secondary). Accessory mineral assemblages include 0–5% quartz, Fe-Ti oxides and minor (< 3%) primary hornblende. Plagioclase occurs as felty, non-foliate laths. Clinopyroxene is most commonly interstitial to plagioclase and occurs as anhedral granular to subophitic crystals, while orthopyroxene is almost entirely interstitial, occurring in poikilitic to subpoikilitic habit. Both pyroxene phases contained abundant exsolution lamellae. Primary biotite occurs as 3-5mm subpoikilitic clots while secondary biotite occurred as overgrowths on Fe-Ti oxides or as an alteration phase after pyroxene. Alteration is variable ranging from relatively unaltered to strong amphibole/uralite/chlorite alteration of pyroxenes and sericitic alteration of plagioclase. In the strongly altered samples, most, if not all, of the pyroxene has been replaced by hornblende and/or actinolitic amphibole.

**Table 2:** Petrographic Attributes of Samples collected from the UCZ near Anorthosite Series Contacts

	Category 1	Category 2	Category 3	Category 4
Samples	SSC1A/1C, 3A/B, 4, 5, 11, 12	SSC1B/1D, 2A/B, 3C	SSC10A-C	SSC6, 7, 8, 9A-C
Modal Rock Type	biotite ilmenite ferrodiorite	ferromonzodiorite	gabbro/ferrodiorite	olivine gabbro
Grain Size	Fine-grained	Medium fine- to medium-grained.	Fine- to medium-grained	Fine- medium fine-grained
Pyroxene types /habits	<u>Clinopyroxene</u> -anhedral granular to subophitic. <u>Orthopyroxene</u> -subpoikilitic to poikilitic	<u>Clinopyroxene</u> -subhedral granular to weakly subophitic. <u>Orthopyroxene</u> -subpoikilitic to poikilitic	<u>Clinopyroxene</u> -subhedral granular; subophitic. <u>Orthopyroxene</u> -subpoikilitic	<u>Clinopyroxene</u> -subhedral granular to weakly subophitic. <u>Orthopyroxene</u> -subpoikilitic
Oxide types/habits	<u>Ilmenite</u> – clotted to bladed. <u>Titanomagnetite</u> -subhedral granular	<u>Ilmenite</u> : bladed/ameboidal. Titanomagnetite-subhedral granular	<u>Ilmenite</u> : bladed/ameboidal. Titanomagnetite-euhedral to subhedral granular	Titanomagnetite-euhedral to subhedral granular
Biotite/Amphibole % and habits	<u>Biotite</u> – 3-10%; 3-5mm subpoikilitic clots/overgrowths on Fe-Ti oxide <u>Hornblende</u> - 0-3%; subhedral granular	<u>Biotite</u> – 0-7%; 1-2mm subpoikilitic clots/overgrowths on Fe-Ti oxide <u>Hornblende</u> - 0-7%; subhedral granular	<u>Biotite</u> – 5-7%; 1-2mm subhedral granular, non-poikilitic to subpoikilitic <u>Hornblende</u> - ≤3%; subhedral granular.	<u>Biotite</u> – 2-7%; subhedral granular, non-poikilitic/overgrowths on Fe-Ti oxide
Accessory phases	Biotite, Fe-Ti oxide, apatite, zircon, quartz, hornblende	Biotite, Fe-Ti oxide, apatite, alkali feldspar	Biotite, Fe-Ti oxide, hornblende, apatite	
Alteration assemblage and intensity	Sericite, saussurite, chlorite, uralite, amphibole (actinolite): Avg. WR minor alteration w/ few samples exhibiting moderate-strong.	Sericite, saussurite, chlorite, uralite, amphibole (actinolite): Avg. WR moderate-strong alteration	Sericite, saussurite, chlorite, uralite, amphibole (actinolite): Avg. WR minor to moderate alteration.	Sericite, saussurite, chlorite, uralite, amphibole (actinolite): Avg. WR trace to minor alteration

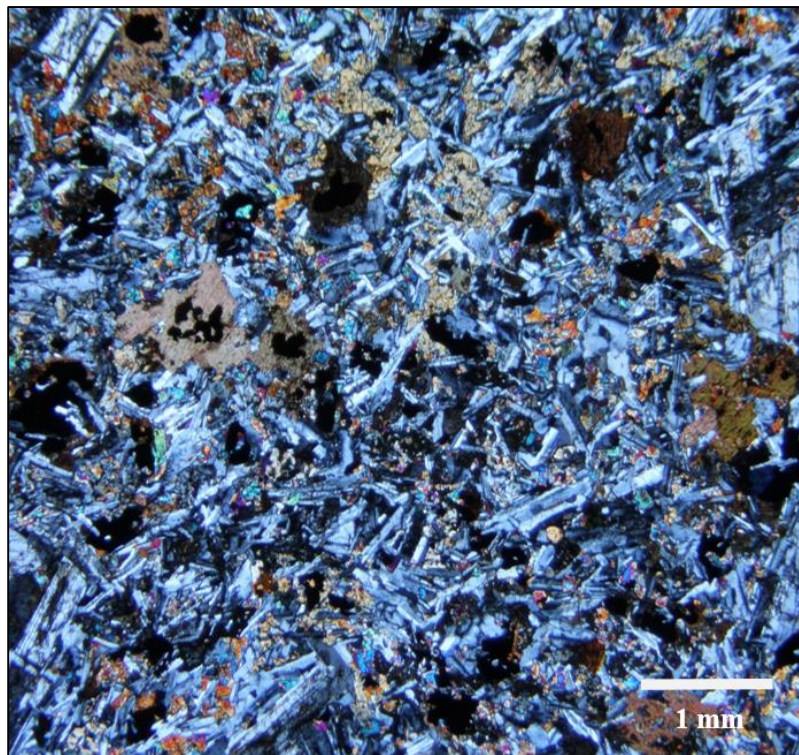
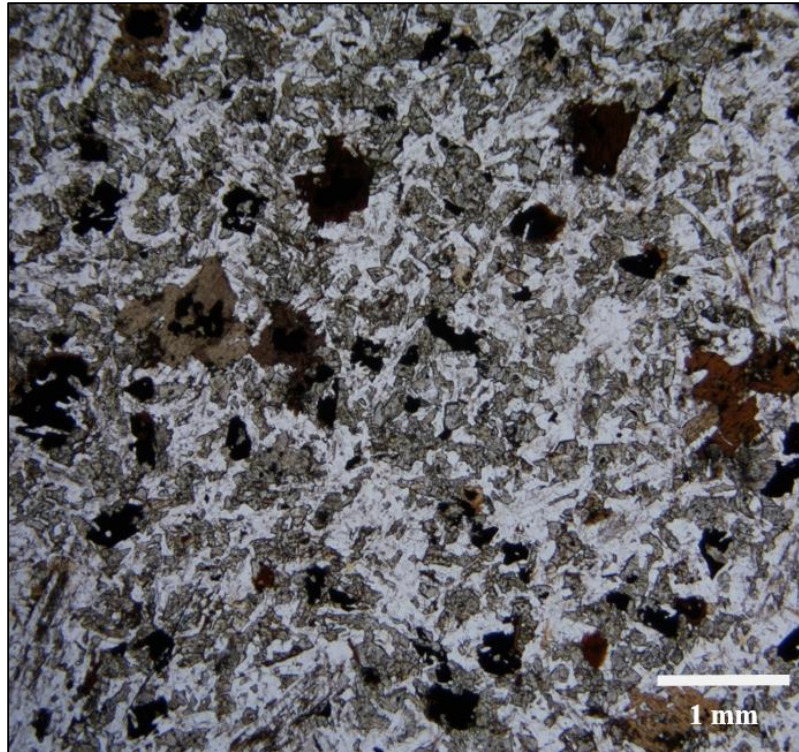


**Figure 7:** Photomicrographs of representative Category 1 rock type (Type-DLS “chill”; Sample SSC 12). Fine-grained, intergranular, biotitic ilmenite ferrodiiorite characterized by felty plagioclase, ophitic to subophitic clino/orthopyroxene and subpoikilitic biotite clots.

Five samples (SSC1B/1D, 2A/B and 3C) comprise Category 2 and are typically a medium fine- to medium-grained ferromonzodiorite to (apatitic) quartz ferromonzodiorite (Table 2). Modally, they are composed of 40 – 50% plagioclase, 15 – 30% clinopyroxene, 0 – 15% orthopyroxene (inverted pigeonite), and 0 – 10% quartz (Fig. 8). Accessory mineral assemblages include, 3-7% Fe-Ti oxides, 0 – 5% biotite, 0-7% primary hornblende, 0 -3% apatite and alkali feldspar. While the mineral assemblages of Category 2 rocks are similar to those of Category 1, they are not considered to be the type chill based on observed differences in grain size, modal mineralogy and distance from DAS contact. Opposed to Category 1, these samples occur in the medial portion of the UCZ, between ~380-980 meters from the DAS contact. Category 2 exhibits a slightly more evolved, felsic, mineral assemblage compared to Category 1, containing more alkali feldspar, apatite and higher modal percentage of quartz along with having a larger grain size compared to Category 1. Interpretation of Category 2 rocks will be discussed below.

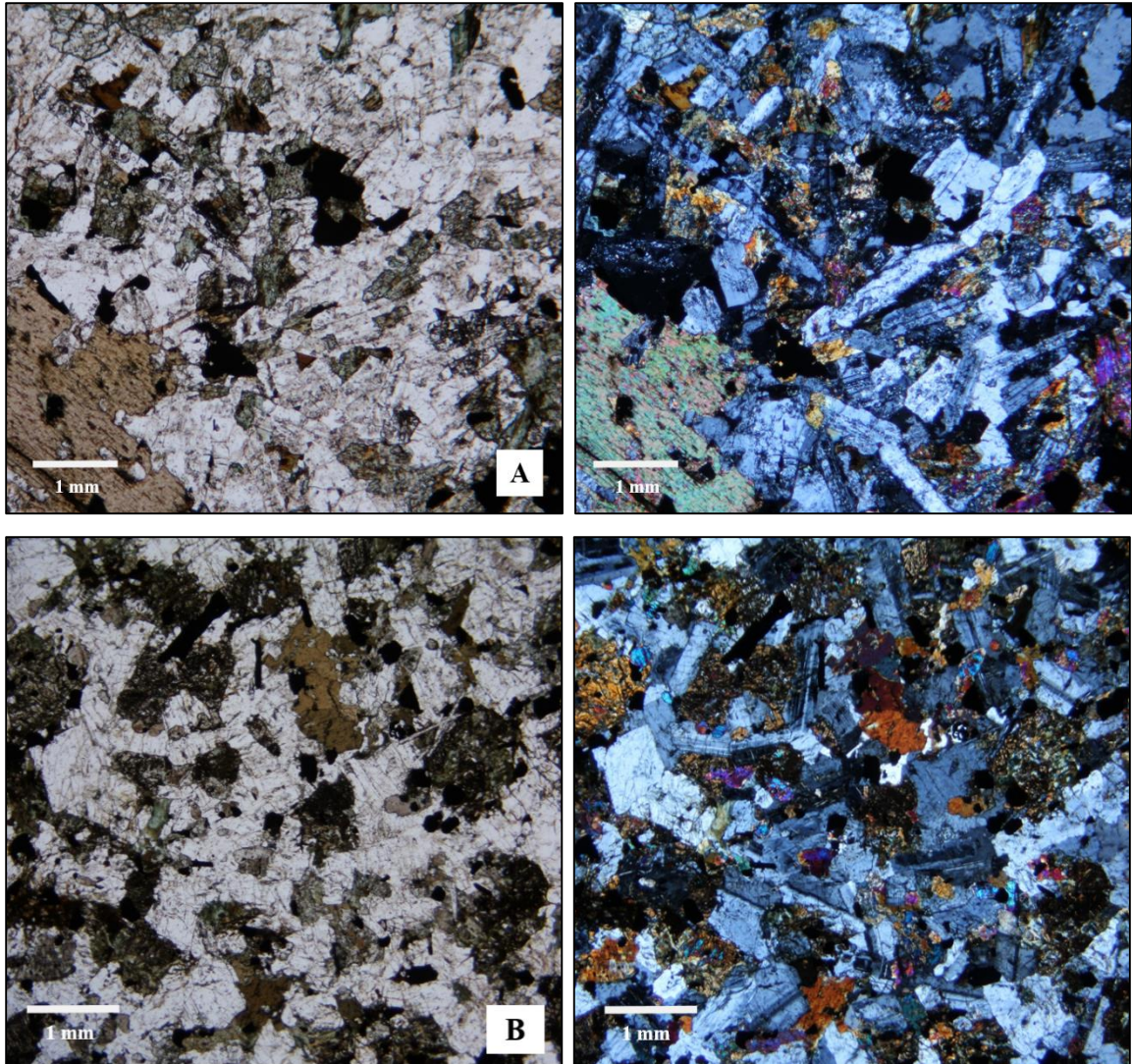


**Figure 8:** Photomicrographs of representative Category 2 rock types: A) biotitic quartz ferromonzodiorite (sample SSC1D). B) medium-fine grained biotitic ferromonzodiorite with decussate plagioclase and granular clinopyroxene (samples SSC2B).

Category 3 consists of samples (SSC10A-C) and displays three distinct textures and mineral assemblages (Table 2; Figure 9). Sample SSC10A is a medium-grained, intergranular oxide gabbro containing 55% plagioclase, 20% clinopyroxene, and 5% orthopyroxene with accessory mineral assemblages including, Fe-Ti oxides, <3% biotite and hornblende along with ~3% euhedral, prismatic apatite. Sample SSC10B is predominantly a fine grained, equigranular ferrodiorite and is irregularly mixed with medium-grained gabbroic cumulates. Bulk rock modal proportions include 60% plagioclase, 25% pyroxene, and 5-7% biotite along with Fe-Ti oxides. Sample SSC10C is a fine grained hornblende, biotite, ilmenite ferrodiorite composed of 60% plagioclase, 15-20% clinopyroxene, and 10% orthopyroxene with accessory mineral assemblages of Fe-Ti oxide, apatite and minor primary biotite and hornblende. Category 3 samples were collected near the western extension of the detached anorthositic block where there UCZ grades into the underlying gabbroic cumulates of the gabbro zone. Texturally, SSC10A is more coarse grained and exhibits cumulate mineral habits which are not characteristic of Category 1. SSC10B is predominantly fine grained, resembling that of Category 1, but mixed with medium-grained cumulates from SSC10A. SSC10C closely resembles the samples from Category 1 exhibiting non-cumulate mineral assemblages of felty, decussate plagioclase and anhedral to subophitic pyroxene. However, this sample has been included into this category based on field occurrence and relationship with SSC10A/B. Interpretation of Category 3 rocks will be discussed below.

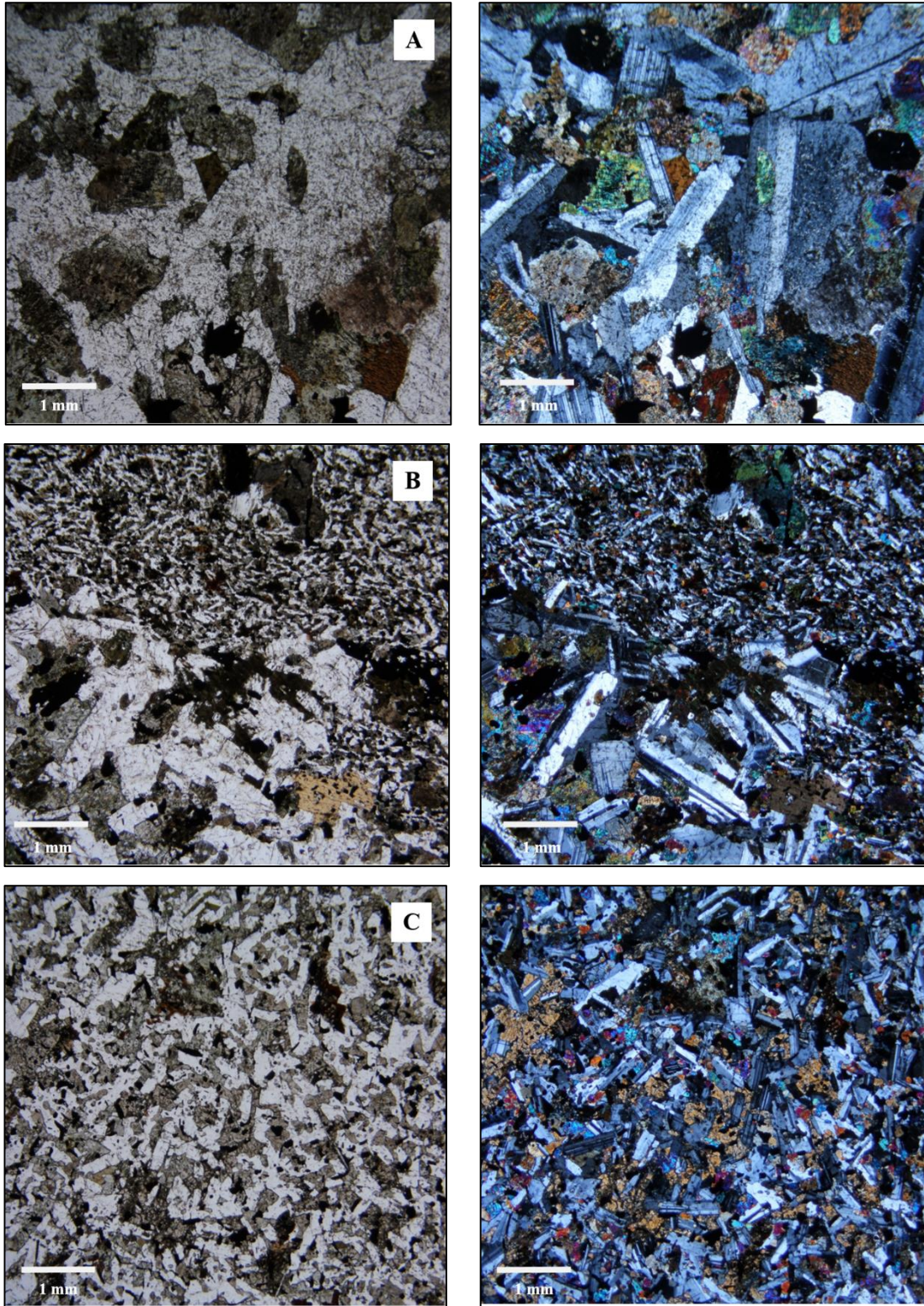


**Figure 9.** Photomicrographs of representative Category 3 rock types: A) medium-grained, intergranular oxide gabbro (sample SSC10A). B) fine grained, equigranular ferrodiorite mixed with medium-grained gabbroic cumulates (samples SSC10B). C) fine grained hornblende, biotite, ilmenite ferrodiorite (samples SSC10C).

Category 4 rocks (SSC6, 7, 8, 9A-C) differ from Category 1 based on mineral assemblages, mineral habit and texture. These samples occur in the north west portion of the UCZ and generally are a fine-grained, equigranular olivine gabbro, composed of 45 – 55% plagioclase, 20 – 30% clinopyroxene, 0-10% orthopyroxene, up to 15% olivine and 5-10% Fe-Ti oxide. In thin section the gabbroic cumulates are irregularly mixed with fine to medium fine-grained ferrodioritic/ferromonzodioritic compositions characteristic of those from Category 2 (Figure 10). Interpretation of Category 4 rocks will be discussed below.

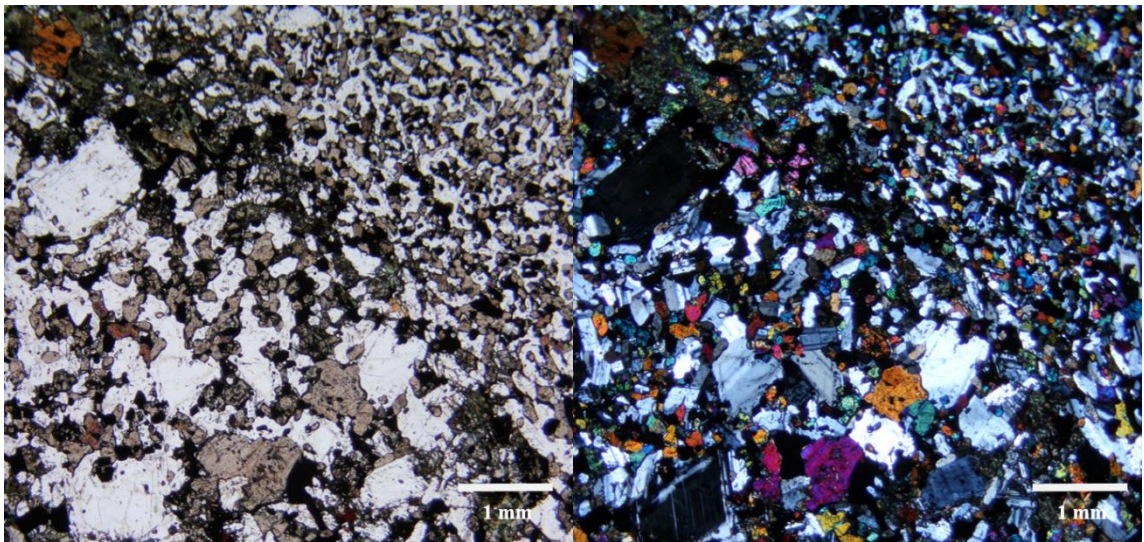


**Figure 10.** Photomicrographs of representative Category 4 rock types: Fine-grained, equigranular olivine gabbro with medium-fine grained ferrodiorite inclusions (sample SSC7).



#### 4.1.2 Cyclic Zone Microgabbro

As mentioned previously, microgabbro sampling sites were identified based on field and petrographic descriptions digitally archived in ArcGIS during mapping of the West Duluth 7.5' quadrangle by Miller and Green (2008b). Samples were sought out where field descriptions consistently report the occurrence of a fine-grained, intergranular, oxide olivine gabbro. A total of thirteen samples were collected from 9 locations (Fig. 11).

Petrographic analysis from the microgabbro intervals show an overall homogeneity in both grain size and mineral proportions. The cyclic zone microgabbro is a fine-grained intergranular oxide-olivine gabbro (Fig. 12). It is modally composed of 40 – 60 % plagioclase, 15 – 30% clinopyroxene, 5 – 30 % olivine and 10-20% Fe-Ti oxide. Plagioclase occurs primarily as equigranular, euhedral to subhedral stubby laths. In many samples, phenocrysts of plagioclase are irregularly scattered throughout and in some samples form megacrysts with clinopyroxene and occasionally olivine. Clinopyroxene occurs as equigranular, subhedral to weakly ameboidal habit and commonly contains exsolution lamellae of Fe-Ti oxide. Olivine is typically subhedral granular and in some samples, weakly sub-poikilitic habit. Oxide, primarily ilmenite, occurs as bladed and subhedral to weakly ameboidal habit. Trace biotite is observed in the microgabbro and typically occurs as rims on Fe-Ti oxide minerals. Though the microgabbro exhibits a sub-equant, intergranular texture and lacks modal layering, they do display a poor foliation based on the alignment of stubby plagioclase laths, ilmenite blades and rectangular augite.

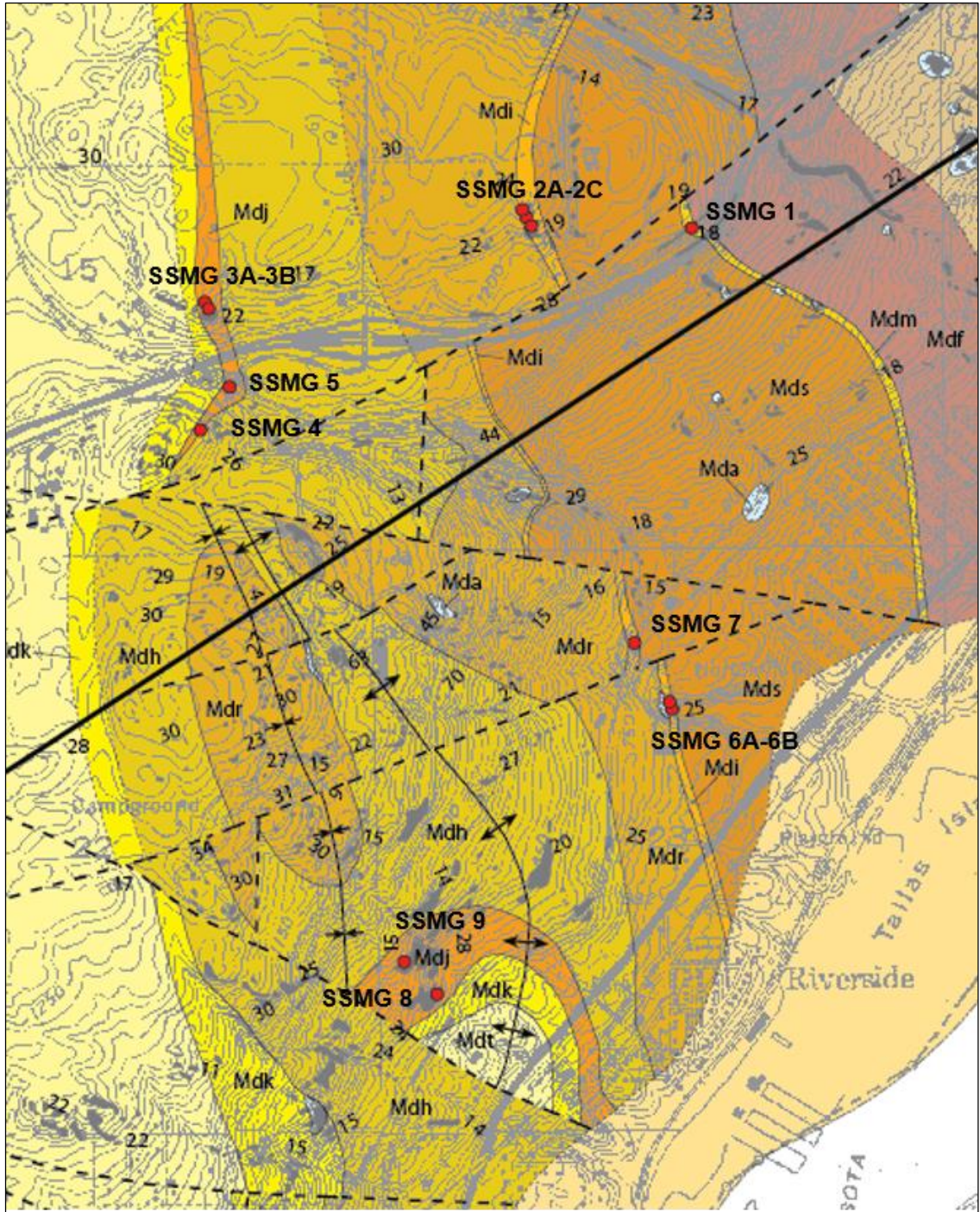


**Figure 11.** Locations of samples collected from the cyclic zone microgabbro. Base map from Miller and Green (2008b).

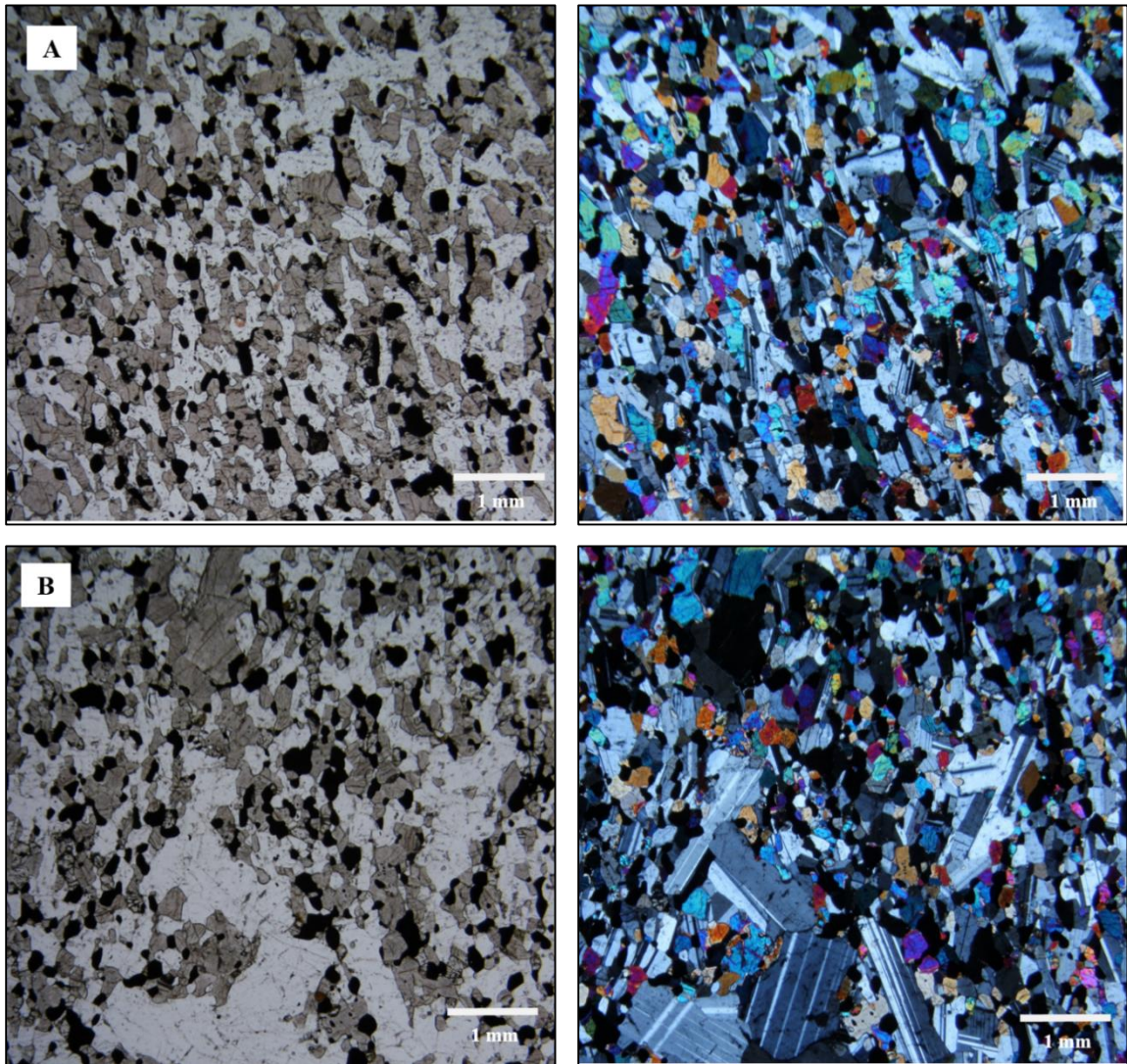


**Figure 12.** Photomicrographs of representative cyclic zone microgabbro. A) fine-grained, moderately foliated, intergranular oxide-olivine gabbro (sample SSMG2B). B) fine-grained, intergranular oxide-olivine gabbro with megacrysts of medium-grained plagioclase (sample SSMG3B).

### **4.1.3 North Shore Volcanic Group Basalt Flows**

Sample sites for potentially comagmatic NSVG basalts were chosen based on the initial geochemical evaluation of the 160 successive lava flows collect by Brannon (1984), which were normalized to the average chill composition and plotted on spider diagrams. Flows which showed the best match to the chill in both major and trace elements were chosen for resampling. As noted in the Methods sections, sampling locations were determined using inset maps that were sketched by Brannon, which delineate individual flow boundaries, in combination with geologic maps of the French River and Lakewood 7.5' quadrangles (Boerboom et al., 2002). However, Brannon's exact sampling locations are unknown. Figure 13 shows sample locations for this study.

Petrographic analysis from the seven collected flows from the NSVG show an overall homogeneity in both grain size and mineral proportions but variations in the habit of clinopyroxene, either granular or ophitic (Fig. 14). Modally these basalts are composed of 40 – 65 % plagioclase and 20 – 30% clinopyroxene with the remainder composed of volcanic glass and 3-10% Fe-Ti oxide. Plagioclase occurred as euhedral to subhedral felty, decussate laths and some samples are weakly plagioclase-porphyritic. As mentioned, clinopyroxene exhibited two habits occurring either as equigranular, subhedral to anhedral granular or ophitic-subophitic with oikocrysts ranging from 1-3mm.

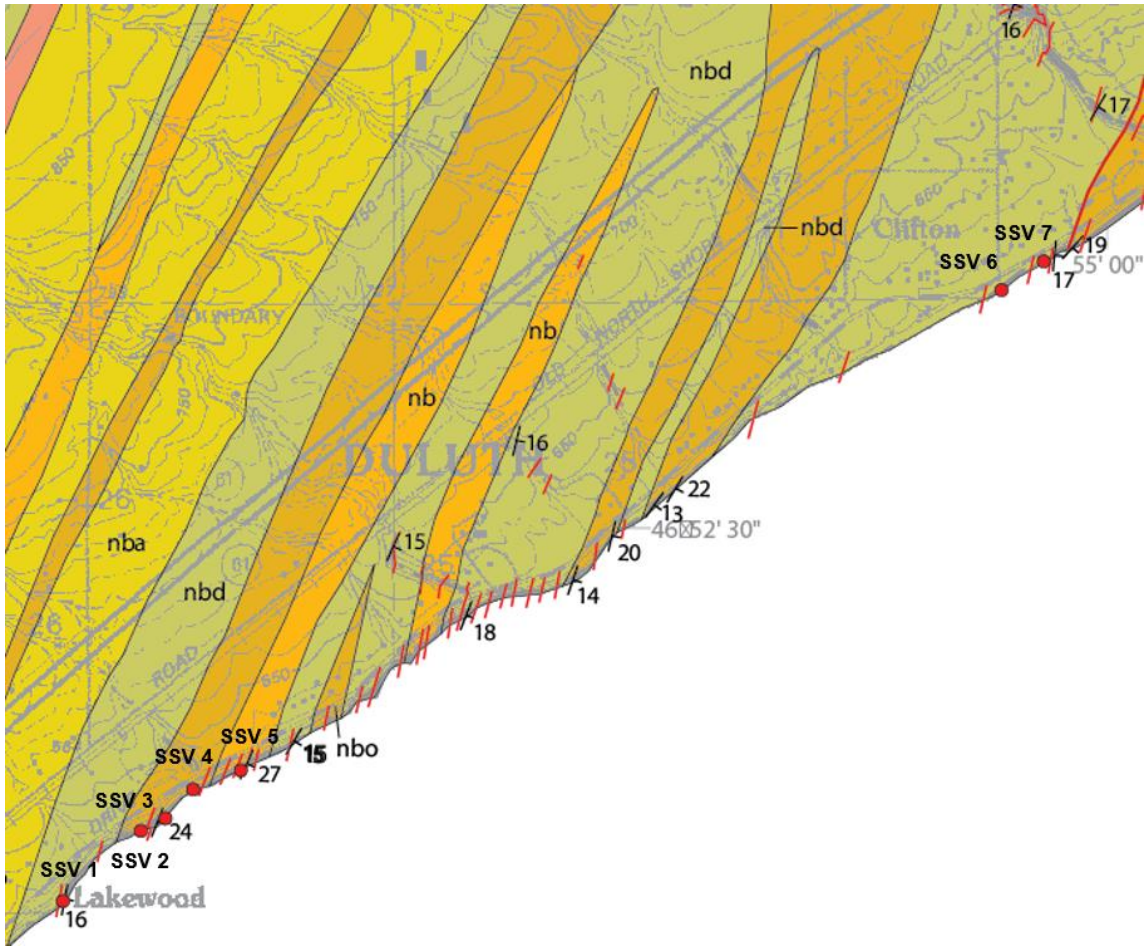


**Figure 13.** Map of North Shore Volcanic Group sample sites. Base map from Boerboom et al. (2002)

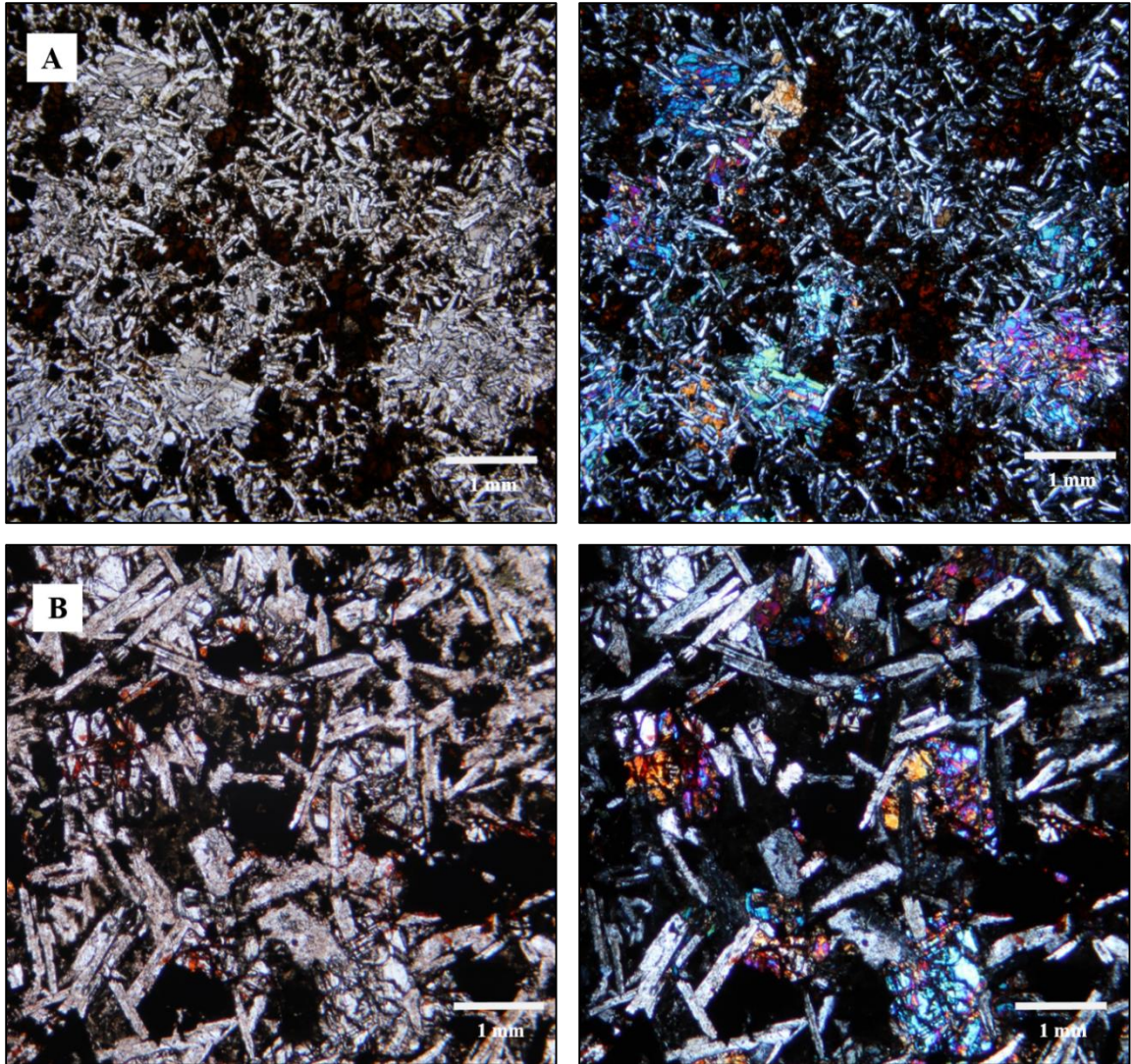


**Figure 14.** Photomicrographs of representative NSVG samples A) Ophitic basalt (SSV 3). B) Intergranular weakly plagioclase-porphyritic basalt (SSV 5).

## 4.2 Mineral Chemistry

The mineral compositions of twenty-four samples were analyzed by SEM-EDS at UMD's Research Instrumentation Laboratory in order to evaluate compositional similarities between the chill, gabbro zone and microgabbro intervals along with the chill and selected flows from the NSVG. Pyroxene was robustly analyzed in all samples (~12 analyses per sample) though where possible, analyses of olivine, biotite and plagioclase were also collected. From the UCZ, the eight ferrodiorite samples determined to be the chill (Category 1, Table 2) were selected for mineral chemical analysis, with the exception of sample SSC3A which is extensively altered. Given the petrographic homogeneity of microgabbro samples, only one sample was analyzed from each of the nine collection sites (if there were multiple samples). All seven NSVG samples were analyzed. Appendix 2 contains full results from mineral chemical analysis.

Data are reported in weight percent oxides and converted to cation proportions. From these cation proportions pyroxene compositions were characterized based on En:F<sub>s</sub>:Wo components ( $\text{Mg}/(\text{Mg}+\text{Fe}+\text{Ca})$ ,  $\text{Fe}/(\text{Mg}+\text{Fe}+\text{Ca})$ , and  $\text{Ca}/(\text{Mg}+\text{Fe}+\text{Ca})$ , respectively), and En' ( $\text{Mg}/(\text{Mg}+\text{Fe})$ ). The same was done for Fo ( $\text{Mg}/(\text{Mg}+\text{Fe})$ ) in olivine and mg# ( $\text{Mg}/\text{Fe}+\text{Mg}$ ) in biotite. In addition to the mineral compositions acquired by SEM analysis for this study, microprobe data from samples of the chill, microgabbros and gabbro zone cumulates, previously collected by Miller (unpublished data), were also incorporated into this study.

En-Fs-Wo compositions of pyroxenes from the DLS chill, cyclic zone microgabbro, NSVG basalt and gabbro zone cumulates are shown in Figure 15. Petrographic observations revealed that both clinopyroxene and orthopyroxene consistently contained

exsolution lamellae and, therefore, care was taken to analyze only the host mineral. Nevertheless, some analyses with Wo contents below 35% Wo in augite and greater than 5% Wo in orthopyroxene represent analyses that include exsolution lamellae. These limits are indicated by the dashed red lines in figure 15. Generally, high-Ca pyroxenes in the four suites plot as magnesian augites and Fe-rich diopside. The high-Ca pyroxenes analyzed in the microgabbro and gabbro zone, however, are more magnesium rich and iron depleted relative to the DLS chill. Low-Ca pyroxenes occurred predominantly in the DLS chill and plot as Fe-rich orthopyroxene.

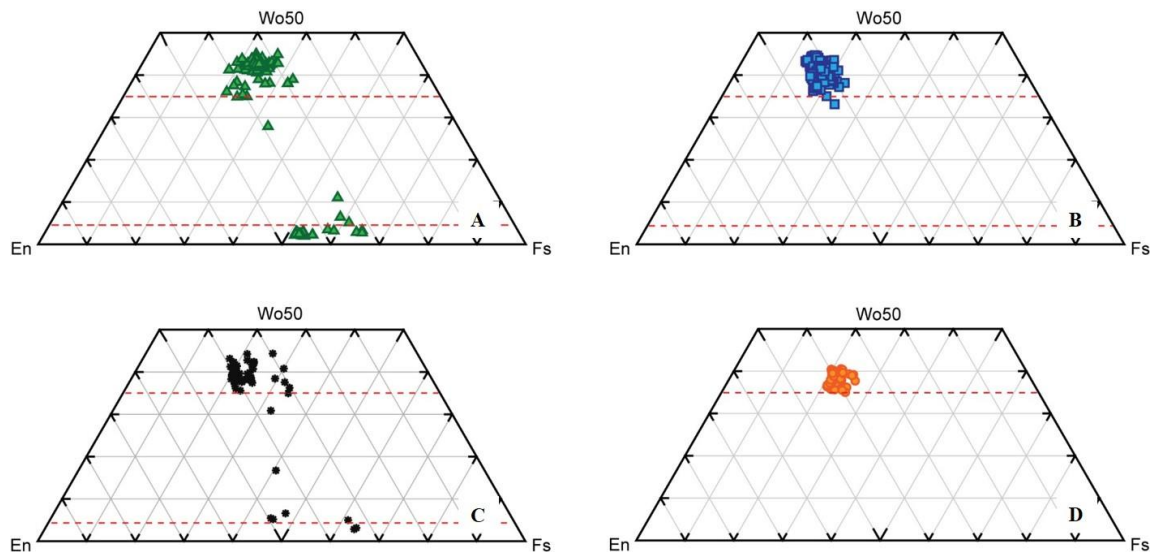


**Figure 15:** Ternary diagram of En-Wo-Fs components in augite in: A) DLS chill, B) cyclic zone microgabbro, C) gabbro zone cumulates, and D) NSVG. The red dashed lines indicates the threshold for analyses that evidently include exsolution lamellae. For augite, this is  $Wo < 35\%$  and for orthopyroxene, it is  $> 5\% Wo$ .



The range of mg# in biotite from the chill, microgabbro and gabbro zone and of Fo content in olivine within the cyclic zone microgabbros and gabbro zone cumulates and are shown in Figures 16 and 17, respectively. This data shows the more iron rich composition of biotite in the DLS chill compared to the gabbro zone and cyclic zone, along with more iron rich olivine in the gabbroic zone cumulates compared to the cyclic zone cumulates.

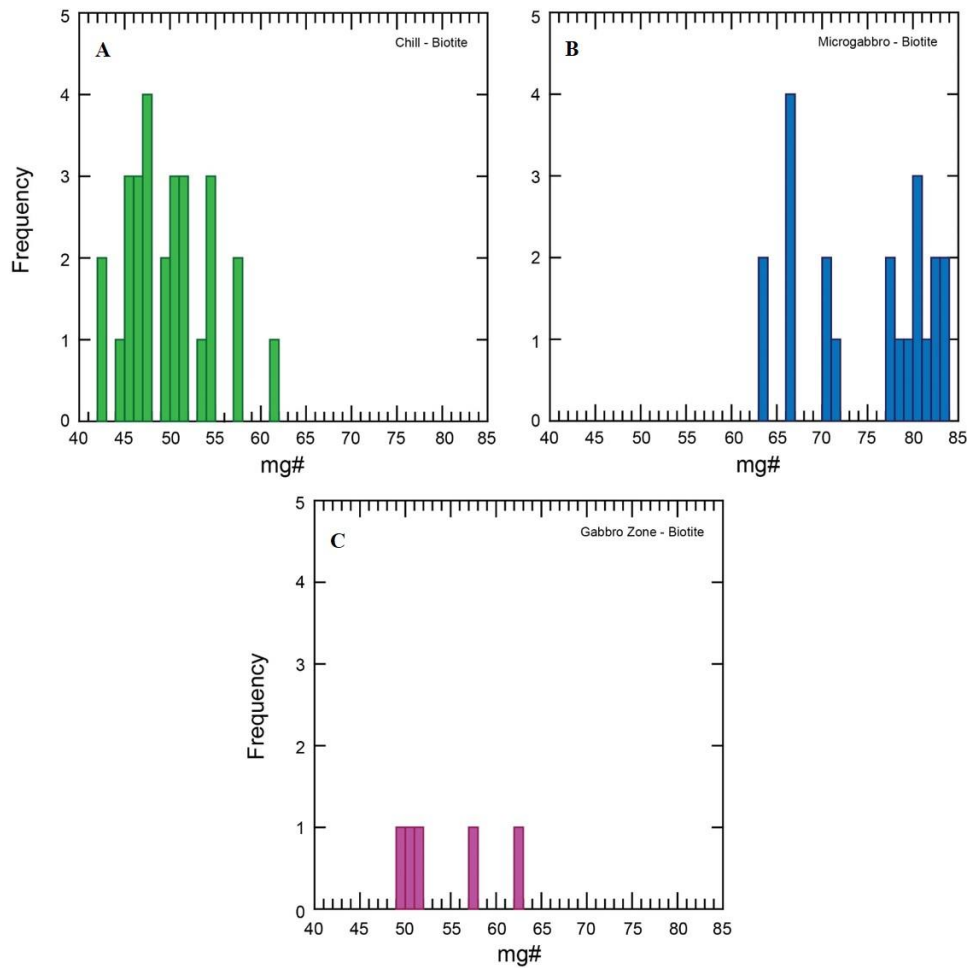


**Figure 16:** Histograms displaying range in mg# in biotite from A) DLS “chill”, B) cyclic zone microgabbro and C) gabbro zone cumulates (mg# = (Mg/Mg+Fe))

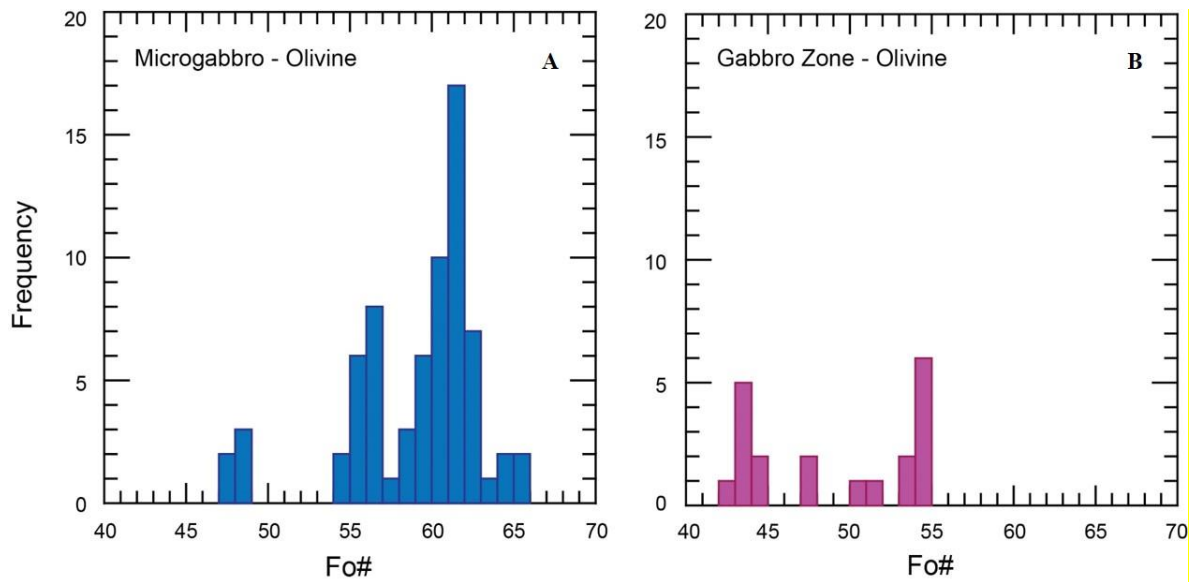


**Figure 17:** Histograms displaying range in Fo content in olivine from A) cyclic zone microgabbro and B) gabbro zone

### 4.3 Whole-Rock Chemistry

Whole rock compositions of forty-two samples from the DLS chill and UCZ (22), the cyclic zone microgabbro (13), and the NSVG (7) were acquired by ICP-MS analysis conducted by Acme Laboratories for major and minor oxides, as well as REE and other trace elements. Major and trace element data are reported in Appendix 3.

As will be discussed in the next chapter, a key component to evaluating the correlation of the DLS chill and its possible volcanic equivalents is using Brannon's (1984) lithochemical database from the NSVG to search for a match. Brannon's (1984) analyses were completed by instrumental neutron activation analysis (INAA) and X-ray fluorescence analysis (XRF). It should also be noted that Brannon's data contain fewer analyses of trace and REE elements compared to the ICP-MS analysis. To be able

to compare her dataset with the ICP-MS analyses collected for this study, it is necessary to first evaluate if there is an analytical bias in some of the analyses. To determine this X/Y plots of certain trace elements were created plotting Brannon's values against the resampled flows (Fig 18). These plots revealed that Brannon's analyses were higher for most trace elements and each element was corrected with a different value, up to 15%.

The three suites of rocks analyzed for their lithochemistry are either non-cumulates (chill, NSVG) or cumulates (microgabbro). Within cumulate rocks, abundances in major elements are primarily controlled by the modes of cumulus mineral phases. Since most trace elements are incompatible with cumulate mineral phases, their abundance is largely controlled by two independent variables – the melt composition and the volume of trapped liquid present in the cumulate rock, now represented by postcumulus phases. Although the absolute abundances of trace elements in cumulates will vary, the ratios of incompatible trace elements should be generally similar in both cumulus and postcumulus components and reflective of the parental magma. One caveat to this statement is that differing degrees of incompatibility of trace elements for various cumulus phases (Fig. 19) will have an effect on the trace element ratios of cumulates, especially those with low percentages of trapped liquid (i.e. adcumulates). Consequently, in the evaluations to follow, only incompatible trace element ratios are used to evaluate compositional attributes of the parental magmas of the cumulates and their possible petrogenetic relationship to the DLS chill. A standard way to evaluate multiple trace element ratios is to plot normalized variation diagrams (spider diagrams). These diagrams use trace element concentrations that have been normalized to a standard composition, such as mantle, chondrites, or MORB. The normalized element concentrations are plotted

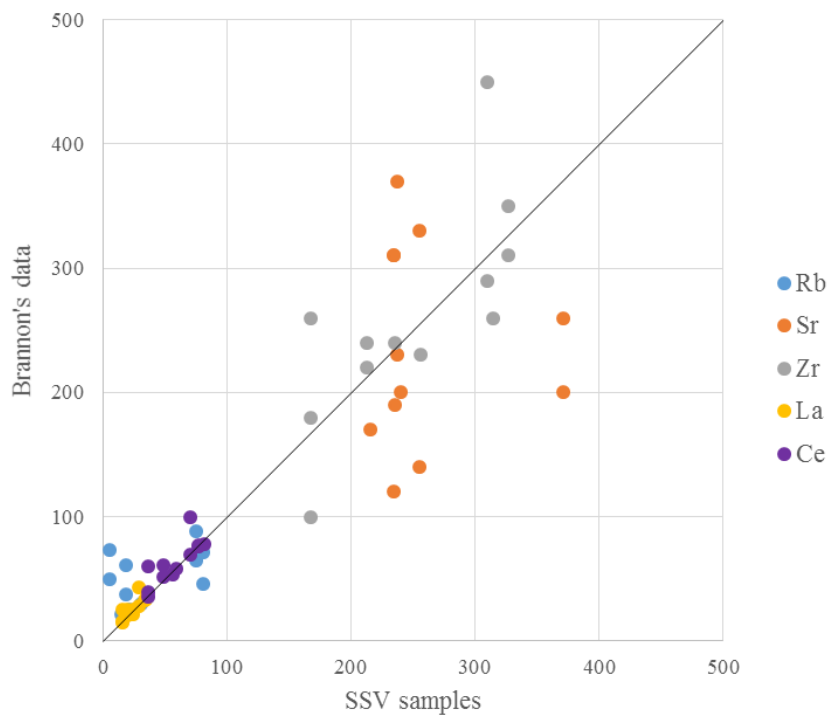
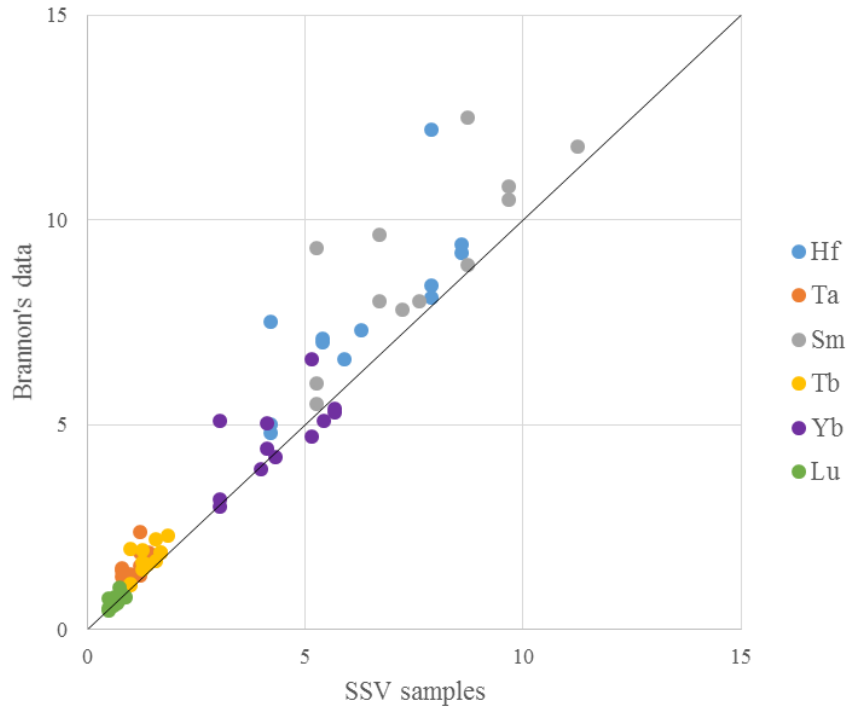


**Figure 18.** X/Y plot evaluating analytical bias of trace element analyses between Brannon's data (Y-axis) and recollected NSVG samples (X-axis).

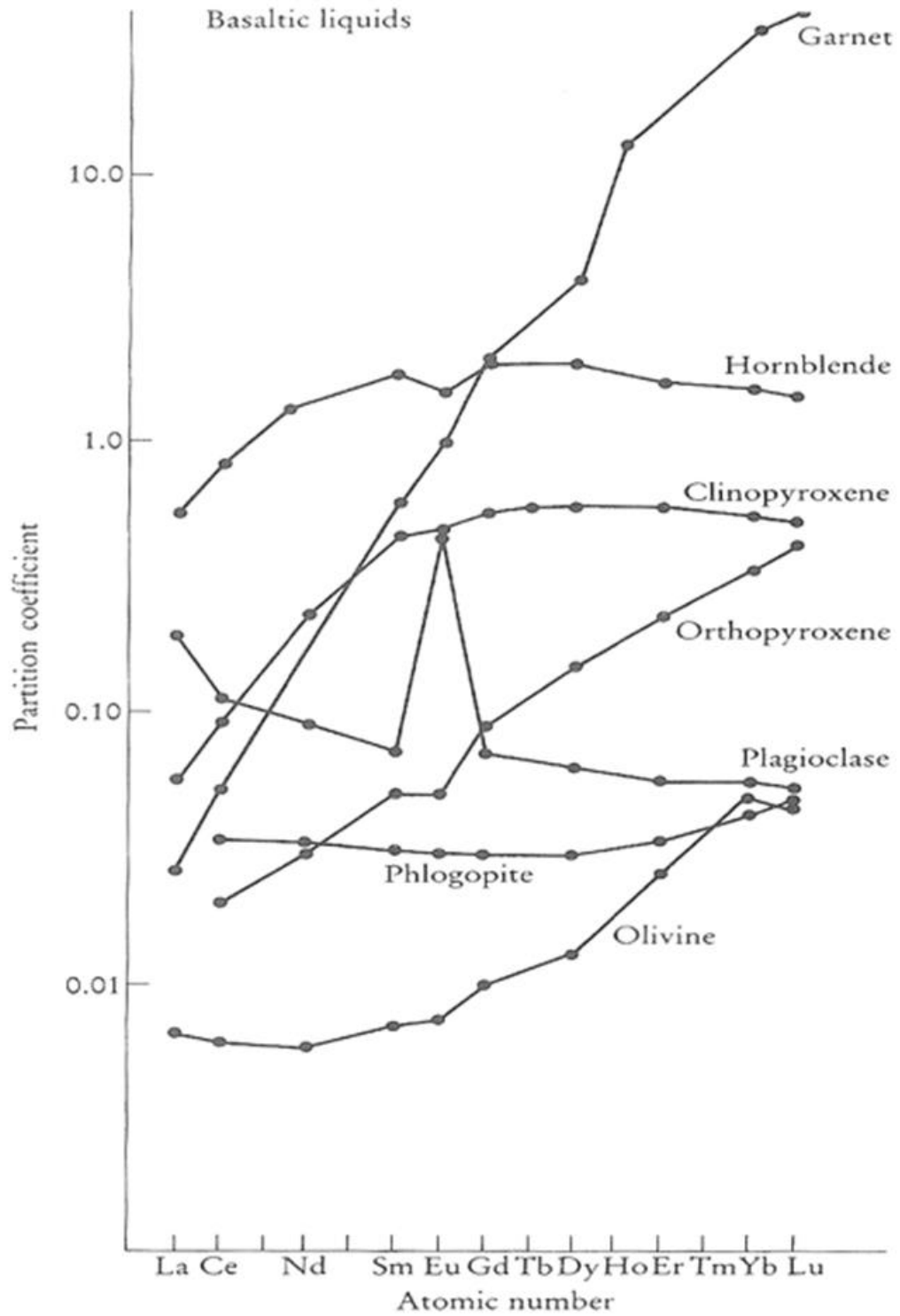


**Figure 19.** Partition coefficients of REEs between common minerals and mafic magmas. (Rollinson, 1993)

on a logarithmic scale with elements in order of increasing incompatibility to the left of the diagram (Rollinson, 1993).

For this study, rare earth element (REE) variation diagrams, were constructed and normalized to the chondrite standard reported by Sun and McDonough (1989). Figures 20-22 show REE spider diagrams for the DLS “chill”, UCZ rocks and microgabbros. Generally speaking, the variation diagrams show similar trends in trace element behavior between the chill and UCZ with slight depletion in the HREE relative to the LREE along with a small negative europium. As would be expected when comparing cumulates to non-cumulates, trace element abundances of the microgabbro cumulates (Fig. 22) are approximately a log unit lower in trace element abundances compared to the DLS chill. As will be discussed in the next chapter, the relatively flat concentration in REE abundances compared to the chill is likely related to the different distribution coefficients of LREE and HREE for the principal cumulus phases (Pl, Cpx, and Ol; see Fig. 19). Similarly, the positive Eu anomaly displayed by the microgabbro cumulates relative to the negative anomaly observed in the chill, is presumably due to the compatibility of  $\text{Eu}^{2+}$  in cumulus plagioclase.

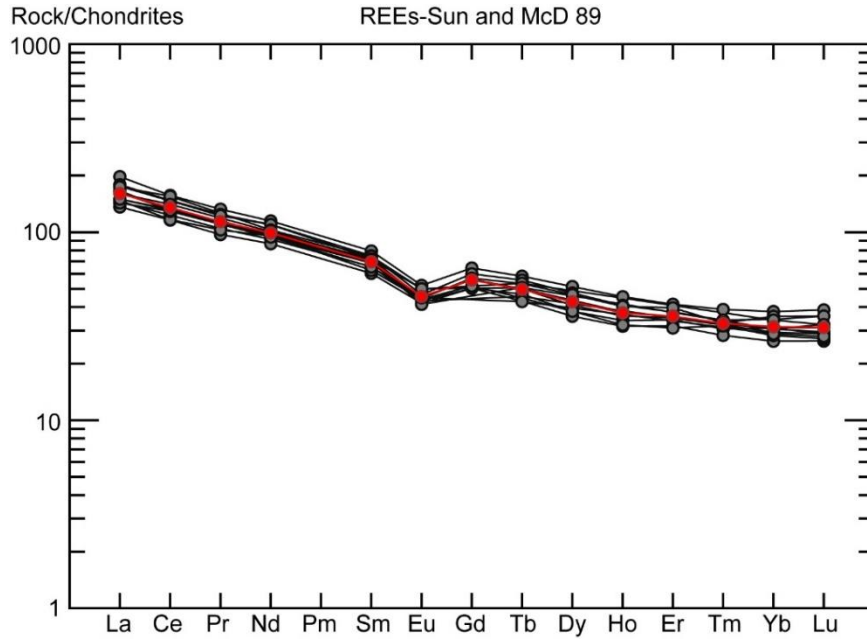


**Figure 20.** Rare earth element variation diagram for DLS chill samples. Red line indicates the DLS “chill” average. REE data are normalized to chondrites reported by Sun and McDonough (1989).

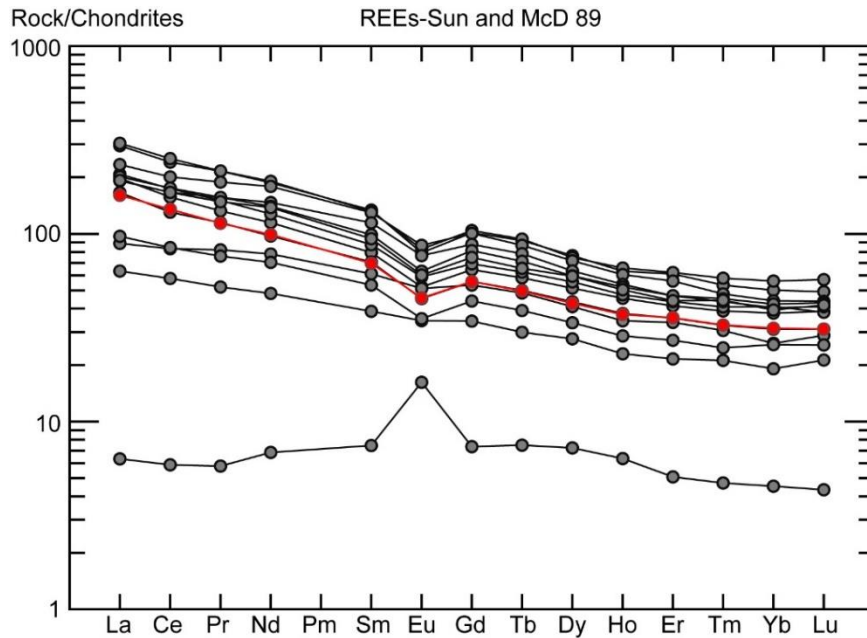


**Figure 21.** Rare earth element variation diagram for UCZ samples. Red line indicates the DLS “chill” average. REE data are normalized to chondrites reported by Sun and McDonough (1989).

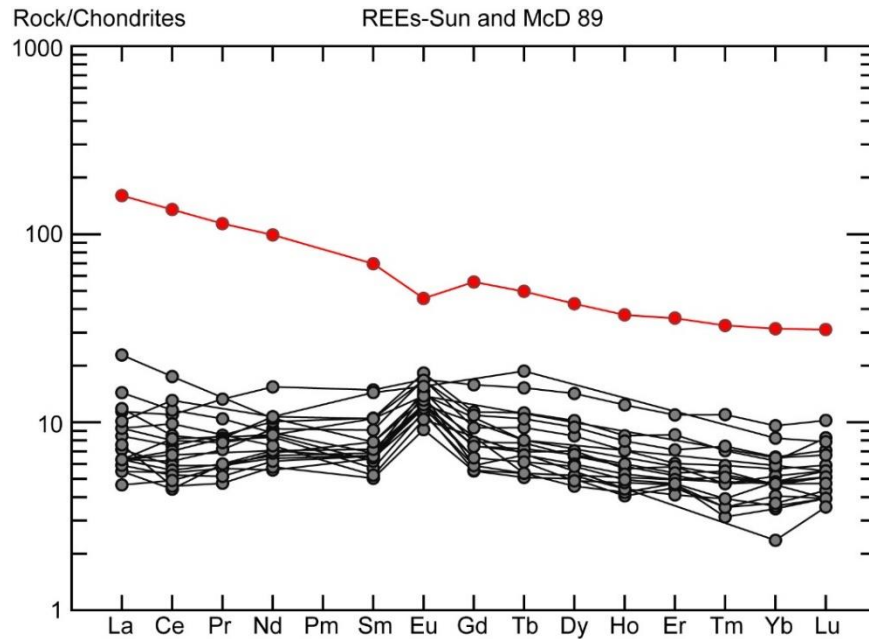


**Figure 22.** Rare earth element variation diagrams for microgabbro samples. Red line indicates the DLS “chill” average. REE data are normalized to chondrites reported by Sun and McDounough (1989).

#### 4.4 Geochemical Modeling

One objective of this study is to evaluate whether the microgabbro cumulates are in equilibrium with the DLS chill composition. This problem was addressed by applying the chill composition to the modified MELTS program, PELE (Boudreau, 1999), to determine the mineral phases in equilibrium with the DLS chill composition along with determining the degree to which volatiles ( $H_2O$  and  $CO_2$ ) were saturated in the chilled magma during decompression attending venting.

Variables of pressure conditions and water content were used in order to evaluate the effects of pressure fluctuations caused by devolatilization (pressure increase) and volcanic venting (pressure decrease) on phase stability and mineral composition. Pressure



and water content variables were assumed on the basis of: lithostatic pressure at the top of the DLS was between 1050-1500 bar (see discussion below), and water contents were from 0 -3.5 wt.% H<sub>2</sub>O (see discussion below). In order to test the effects of changing pressure on the system, compositions were run in two sets; effect of devolatilization and decompression (volcanic venting) and effect of decompression under water saturated conditions. Devolatilization runs were completed as follows: the starting temperature was set based on the calculated liquidus temperature of the chill composition at 1500 bar lithostatic pressure. Allowing PELE to run in 1°C steps, the temperature at which plagioclase, olivine and clinopyroxene first became saturated were recorded. Next, while using the same starting temperature, runs were completed at 1600, 1700 and 1800 bar and the saturation temperature of clinopyroxene was recorded. Testing decompressional effects on pyroxene stability, runs were completed at 1800 bar initial pressure and a temperature at which all three phases are initially saturated. Keeping temperature constant, the pressure was dropped 300 bars in one step. This process was also repeated using different wt.% H<sub>2</sub>O to evaluate if the presence of volatiles had any effect.

In addition to testing phase stability due to pressure increases and decreases, PELE was also used to test the effects of decompression under low pressure at water saturated conditions. Water saturated conditions were assumed based on the occurrence of hydrous mineral assemblages within the chill, biotite and amphibole, which are stable in basaltic magmas at water-saturated or near-saturated conditions (Wones and Eugster, 1965). This process was modeled as follows: Sample MD279 was used as the input bulk rock composition as this sample represents the type DLS chill. The liquidus temperature was recorded at pressures between 1800 to 1 bar lithostatic pressure at different water

contents between 0 – 3.5 wt.% H<sub>2</sub>O. This process was then repeated at water saturated conditions determined by using the ‘find water saturation’ function in PELE. Results from devolatilization and venting runs are listed in Table 3 and will be discussed below.

Lastly, PELE was used to evaluate the comagmatic relationship between the DLS chill and cyclic zone microgabbros by determining the mineral phases in equilibrium with the chill composition and comparing them to the phase compositions observed in the microgabbros. These calculations were run under equilibrium crystallization, 1500 bar lithostatic pressure and QFM conditions from -2 to +2. Initial experiments with the program revealed that the amount of water in the magma had a strong effect on the liquidus temperature, mineral compositions and phase stability, most severely noticed in plagioclase. Two sets of calculations were performed. The first set was completed at QFM conditions with varying H<sub>2</sub>O contents from 0 – 3.5 wt.% in order to evaluate the degree of water saturation in the chill. The second set was completed by varying the water content between 0 – 3.5 wt.% along with varying the oxygen fugacities from QFM -2 to QFM +2. Results from PELE are listed in Table 4.

**Table 3a.** Devolatilization experiments performed to verify clinopyroxene phase stability calculated with the PELE program.

Wt.% Water	Pressure (bar)	Bulk liquidus T ( $^{\circ}$ C)	Plagioclase liquidus T ( $^{\circ}$ C)	Olivine liquidus T ( $^{\circ}$ C)	Clinopyroxene Liquidus T ( $^{\circ}$ C)
0.5	1500	1142	1141	1124	1097
0.5	1600				1099
0.5	1700				1101
0.5	1800				1103
1	1500	1106	1106	1106	1082
1	1600				1084
1	1700				1086
1	1800				1088
1.5	1500	1101	1077	1100	1071
1.5	1600				1073
1.5	1700				1075
1.5	1800				1077

**Table 3b.** Decompression experiments performed to verify the effects of decompression under low pressure at water saturated conditions calculated with the PELE program

0.05 wt. % Water		1.0 wt. % Water		2.0 wt. % Water		3.0 wt. % Water	
Pressure (bar)	Liquidus T (°C)	Pressure (bar)	Liquidus T (°C)	Pressure (bar)	Liquidus T (°C)	Pressure (bar)	Liquidus T (°C)
1	1132	1	1096.79	1	1085.18	1	1076.48
50	1132.52	50	1096.79	50	1085.54	50	1076.84
100	1133.29	100	1097.17	100	1085.91	100	1077.2
200	1134.05	200	1097.75	200	1086.64	200	1077.91
300	1134.8	300	1098.47	300	1087.37	300	1078.63
400	1135.55	400	1099.2	400	1088.09	400	1079.34
500	1136.29	500	1099.93	500	1088.82	500	1080.05
600	1137.02	600	1100.64	600	1089.85	600	1080.76
700	1137.74	700	1101.35	700	1090.67	700	1081.47
800	1138.46	800	1102.05	800	1091.39	800	1082.18
900	1139.17	900	1102.74	900	1092.1	900	1082.89
1000	1139.87	1000	1103.43	1000	1092.82	1000	1083.59
1100	1140.56	1100	1104.1	1100	1093.53	1100	1084.3
1200	1141.24	1200	1104.77	1200	1094.25	1200	1085.34
1300	1141.91	1300	1105.43	1300	1094.97	1300	1086.1
1400	1142.56	1400	1106.07	1400	1095.72	1400	1086.83
1500	1143.21	1500	1106.7	1500	1096.47	1500	1087.57
1600	1143.85	1600	1107.32	1600	1097.21	1600	1088.3
1700	1144.48	1700	1107.93	1700	1097.96	1700	1089.03
1800	1144.47	1800	1108.54	1800	1098.7	1800	1089.75

**Table 4a.** Mineral chemistry experiments performed to determining the mineral phases in equilibrium with the DLS chill calculated with the PELE program. Calculations were completed using MD279A as the reference sample, at 1500 bar pressure and QFM conditions.

Wt.% H <sub>2</sub> O	Olivine (Fo)	Clinopyroxene (Di)
0	49.73	69.93
0.5	56.22	72.92
1.0	59.13	74.29
1.5	61.6	75.4
2.0	63.08	76.09
2.5	64.43	76.73
3.0	66.99	77.96
3.5	68.55	78.75

**Table 4b.** Mineral chemistry experiments performed to determining the mineral phases in equilibrium with the DLS chill calculated with the PELE program. Calculations were completed using MD279A as the reference sample, at 1500 bar pressure and variable oxygen fugacities.

QFM-1			QFM-2		
Wt.% H <sub>2</sub> O	Olivine (Fo)	Clinopyroxene (Di)	Wt.% H <sub>2</sub> O	Olivine (Fo)	Clinopyroxene (Di)
0	49.2	69.6	0	48.67	69.31
0.5	54.74	72.22	0.5	53.72	71.74
1	57.8	73.65	1	56.61	73.1
1.5	59.84	74.6	1.5	58.64	74.06
2	61.55	75.39	2	60.34	74.85
2.5	61.9	75.61	2.5	60.44	74.97
3	60.14	74.98	3	58.72	74.37
3.5	60.08	75.09	3.5	57.02	73.81

QFM+1			QFM+2		
Wt.% H <sub>2</sub> O	Olivine (Fo)	Clinopyroxene (Di)	Wt.% H	Olivine (Fo)	Clinopyroxene (Di)
0	51.41	70.78	0	64.72	76.56
0.5	58.37	73.93	0.5	64.82	76.77
1	63.12	76.04	1	68.7	78.57
1.5	65.48	77.12	1.5	68.4	78.55
2	67.27	77.96	2	72.66	80.51
2.5	69	78.79	2.5	75.25	81.85
3	72.38	80.47	3	77.86	83.27
3.5	74.49	81.57	3.5	79.36	84.14

## **5. Discussion**

The petrographic and geochemical data presented above provide an improved understanding of various aspects within the upper contact zone and cyclic zone of the Duluth Layered series at Duluth. The discussion to follow will focus on evaluating potential comagmatic relationships among several features within the DLS, along with the selected lava flows of the North Shore Volcanic Group. First, the field occurrence, petrographic and geochemical characteristics of what distinguishes the DLS chill from other UCZ rocks will be discussed. Second, a potential plutonic-volcanic link between the DLS chill and lava flows overlying the Duluth Complex will be evaluated. Next, the model of decompression quenching of a hydrous magma during venting proposed by Miller (Miller and Ripley, 1997; Miller and Severson, 2002) to explain the formation of the chill, and tested using the PELE algorithm for magmatic phase equilibrium, will be discussed. PELE was also used to evaluate a comagmatic link between the chill and microgabbro intervals of the cyclic zone by comparing the chill composition to the phase and mineral chemistries of the microgabbro. Finally, a petrologic model for the origin of the DLS chill and related rocks will be discussed.

### **5.1 Petrologic Significance of the DLS chill**

From petrographic and whole-rock analysis of samples collected from the UCZ, it is evident that some samples were not of the characteristic DLS chill. As reported above, samples collected from the UCZ were grouped into four different categories based on lithology and occurrence within the UCZ. Only the eight samples comprising Category 1 (SSC1A, 1C, 3A-B, 4, 5, 11, 12) resemble the representative or type DLS chill defined by sample MD279A (Figs. 5, 7) and they show a striking homogeneity in mineralogy,

texture and composition along the DLS-DAS contact. When considering the texture, mineral chemistry and whole rock chemistry of the DLS chill samples, they clearly indicate quenching of a geochemically evolved magma composition.

In general, the mafic “chill” is a fine-grained, intergranular, biotitic ferrodiorite and texturally is defined by randomly oriented, felty plagioclase, anhedral granular augite, subophitic orthopyroxene, bladed ilmenite and porphyritic to subpoikilitic clots of biotite. These fine-grained, non-cumulate textures characteristic of the chill are indicative of magma quenching. Evaluation of mineral chemistries from the chill also indicate quenching of an evolved magma. Figure 23 shows mineral chemistries from augites analyzed in the chill (a), microgabbro (b), and gabbro zone (c). Augites analyzed from the chill are more evolved (lower mg#) compared to the microgabbro and gabbro zone cumulates. Therefore, the more iron rich composition of the chill likely indicates it formed by rapid cooling of a liquid rather than cumulate crystallization. Lastly, the whole rock composition of the chill (Table 5) indicates it is too evolved to represent a parental magma to the DLS. The whole-rock composition of the chill contains high  $\text{TiO}_2$  and  $\text{P}_2\text{O}_5$  abundances along with elevated incompatible trace elements (e.g. Zr, Hf, Nb, Ta, Rb, Cs) and low compatible trace elements (e.g. Ni, Cr, Co, Sc). Furthermore, when compared to other Layered Series intrusions (Fig. 24), the chill composition plots near the apex of the tholeiitic iron enrichment trend and corresponds to an evolved tholeiitic ferrobasalt, again indicating it is too evolved to be parental to the DLS.

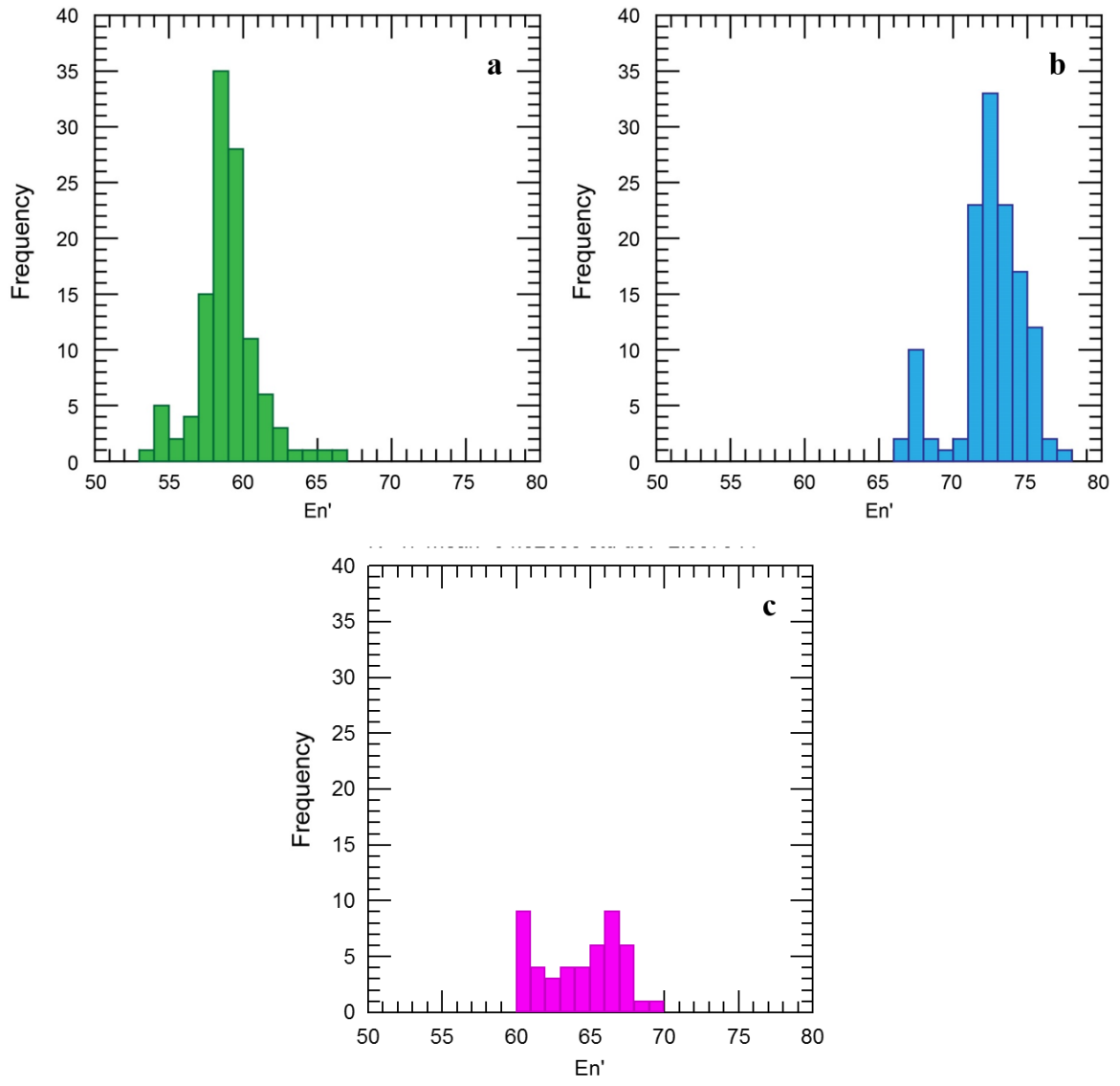


**Figure 23.** Histograms displaying range in En' in augite in a) chill, b) microgabbro and c) gabbro zone ( $En' = Mg / (Mg + Fe)$ ).



**Table 5.** Whole rock lithogeochemical data for DLS “chill” samples. Major oxides reported in percentages, all others in ppm. Total iron reported as Fe<sub>2</sub>O<sub>3</sub>. MD samples were previously analyzed by Miller (2008a).

Sample	SSC1A	SSC1C	SSC3A	SSC3B	SSC4	SSC5	SSC11	SSC12	MD342D	MD268	MD279A	MD293A'	MD260B	Average Chill
SiO <sub>2</sub>	49.33	48.57	48.07	50.10	49.49	49.23	49.71	48.50	48.80	48.30	48.50	49.10	47.20	48.84
Al <sub>2</sub> O <sub>3</sub>	12.89	13.80	13.57	12.99	13.19	13.44	15.39	14.61	12.30	13.30	13.10	13.20	12.50	13.41
Fe <sub>2</sub> O <sub>3</sub> *	15.69	14.89	14.93	14.55	15.15	14.54	13.54	14.34	15.8	15.6	14.1	15.1	16.5	15.69
MgO	4.83	5.25	6.31	4.68	4.86	5.15	4.92	5.17	4.57	5.00	4.77	4.82	4.89	5.02
CaO	8.66	8.72	8.17	8.64	8.23	8.69	9.27	8.85	8.52	9.15	9.31	8.78	9.27	8.79
Na <sub>2</sub> O	2.85	2.88	2.71	2.73	3.02	3.06	2.87	2.85	2.65	3.10	2.89	2.70	2.68	2.85
K <sub>2</sub> O	1.00	0.85	0.61	1.44	1.49	1.11	1.04	1.23	1.26	0.42	1.05	0.93	0.71	1.01
TiO <sub>2</sub>	3.37	3.08	2.91	3.17	3.21	3.05	2.78	3.00	3.49	3.35	2.97	3.10	3.49	3.15
P <sub>2</sub> O <sub>5</sub>	0.58	0.53	0.47	0.53	0.47	0.50	0.45	0.49	0.60	0.58	0.53	0.55	0.65	0.53
MnO	0.23	0.21	0.25	0.22	0.22	0.19	0.18	0.20	0.22	0.22	0.18	0.22	0.23	0.21
Cr <sub>2</sub> O <sub>3</sub>	0.01	0.01	0.02	0.02	0.01	0.01	0.01	0.02						0.01
Total	99.443	98.793	98.019	99.067	99.343	98.974	100.164	99.255	98.21	99.02	97.4	98.5	98.12	99.443
Ni	74.00	85.00	95.00	50.00	61.00	79.00	89.00	85.00	60.00	76.00	77.00	73.00	63.00	74.38
Sc	35.00	32.00	33.00	36.00	34.00	33.00	30.00	31.00	34.20	33.60	31.30	33.30	35.00	33.18
Ba	393.00	265.00	276.00	347.00	522.00	255.00	313.00	347.00	338.00	156.00	134.00	266.00	288.00	300.00
Be	1.00	5.00	3.00	1.00	2.00	1.00	1.00	3.00						2.13
Co	41.50	43.00	46.30	38.30	39.30	45.30	42.20	40.20	33.00	35.00	33.00	33.00	36.00	38.93
Cs	2.00	2.00	0.90	2.60	3.30	2.50	1.50	2.30						2.14
Ga	22.50	22.70	22.00	20.90	21.30	20.70	21.10	20.80						21.50
Hf	9.70	8.30	7.70	9.30	9.30	8.40	7.80	7.70	10.00	7.00	8.00	9.00	7.00	8.40
Nb	28.10	24.40	22.40	25.40	25.80	24.00	21.40	22.90	27.00	25.00	25.00	25.00	26.00	24.80
Rb	35.20	35.00	18.20	57.70	55.70	50.80	38.00	44.60	44.00	15.00	46.00	34.00	19.00	37.94
Sn	3.00	3.00	3.00	3.00	2.00	3.00	3.00	3.00						2.88
Sr	227.20	225.00	228.10	236.80	238.20	229.00	259.80	267.40	168.00	180.00	186.00	180.00	181.00	215.88
Ta	1.80	1.50	1.40	1.90	1.40	1.30	1.40	1.20	2.00	0.80	1.00	2.00	0.80	1.42
Th	5.30	4.80	4.80	5.90	4.70	5.40	4.50	4.70	5.00	4.00	5.00	5.00	2.00	4.70
U	1.50	1.40	1.50	2.00	1.70	1.70	1.20	1.20	2.60	1.50	1.90	2.30	1.60	1.70
V	336.00	298.00	299.00	316.00	323.00	313.00	277.00	296.00	346.00	336.00	320.00	336.00	381.00	321.31
W	0.50	0.90	0.50	0.60	0.50	0.60	0.50	0.50						0.58

**Table 5:** continued.

Sample	SSC1A	SSC1C	SSC3A	SSC3B	SSC4	SSC5	SSC11	SSC12	MD342D	MD268	MD279A	MD293A'	MD260B	Average Chill
Zr	407.30	358.50	320.60	385.80	382.00	375.70	304.50	323.60	386.00	306.00	341.00	343.00	278.00	347.08
Y	64.50	52.90	50.90	59.40	60.10	53.40	48.40	49.10	64.00	56.00	55.00	56.00	61.00	56.21
La	46.80	39.30	34.30	42.40	41.60	38.30	32.30	35.00	41.20	35.60	35.60	38.00	33.90	38.02
Ce	96.10	79.90	75.40	90.40	89.80	81.00	71.10	71.40	95.00	81.00	80.00	86.00	79.00	82.78
Pr	12.58	10.90	9.93	11.80	11.63	10.61	9.24	9.78						10.81
Nd	53.60	45.50	42.80	51.30	51.20	44.90	40.60	44.50	48.00	44.00	44.00	47.00	44.00	46.26
Sm	12.17	10.82	10.02	11.46	11.07	10.47	9.25	9.59	11.40	10.50	10.00	11.00	10.70	10.65
Eu	3.02	2.62	2.51	2.70	2.58	2.61	2.43	2.55	2.90	2.50	2.60	2.90	2.40	2.64
Gd	13.26	11.44	10.33	12.33	11.71	11.52	10.34	10.65						11.45
Tb	2.18	1.87	1.75	2.08	1.99	1.87	1.61	1.67	2.00	1.70	1.60	1.90	1.90	1.86
Dy	13.06	11.03	9.64	12.05	11.82	10.38	9.07	9.65						10.84
Ho	2.57	2.13	1.92	2.31	2.28	2.03	1.79	1.82						2.11
Er	6.84	5.89	5.66	6.23	6.55	5.80	5.25	5.12						5.92
Tm	0.99	0.83	0.78	0.87	0.84	0.83	0.72	0.81						0.83
Yb	6.43	5.28	5.26	5.84	6.06	5.21	4.47	4.79	5.80	5.00	4.90	5.20	5.20	5.34
Lu	0.98	0.79	0.73	0.91	0.91	0.82	0.67	0.69	0.82	0.73	0.71	0.75	0.75	0.79

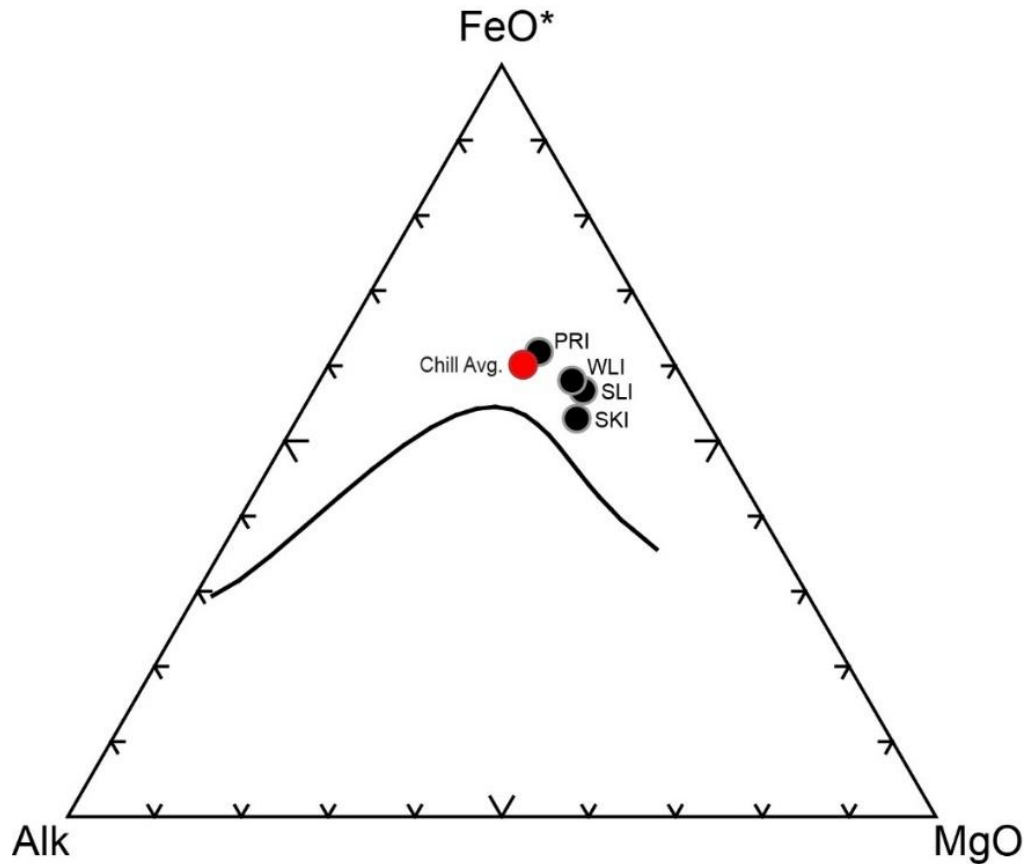


**Figure 24.** AFM diagram comparing the DLS chill composition against other Layered Series intrusions; South Kawishiwi Intrusion (SKI), Sonju Lake Intrusion (SLI), Wilder Lake Intrusion (WLI) and Partridge River Intrusion (PRI).

The chill composition was applied to PELE to evaluate initial cumulus mineral assemblages. Regardless of water content, PELE consistently reported an initial assemblage of olivine, plagioclase and augite. The persistent occurrence of olivine reported by PELE is unexplained. However, Miller and Ripley (1996) applied an average “chill” composition similar to that shown in Table 5 to the Chaos 2 fractional crystallization model of Nielsen (1990). They reported that a dry chill composition should initially crystallize a cumulus assemblage of augite, plagioclase and Fe-Ti oxide

(Miller and Ripley, 1996). Based on their results, the DLS chill composition discussed here is more closely related to PCOF cumulates of the cyclic and gabbro zone.

Away from the immediate contact with the AS to the northern and eastern portions of the UCZ, samples display different modal mineralogies, textures and whole rock compositions compared with the DLS chill samples of category 1. These compositions are grouped into three other categories as described earlier. The possible petrologic significance of these other UCZ samples is discussed here.

Rock samples comprising category 2 (SSC1B/D, 2A/B and 3C) occurring within the medial portion of the UCZ, in Logan and Miller creek, exhibit a range of generally more evolved intermediate compositions and occur typically as medium fine- to medium-grained ferromonzodiorite to (apatitic) quartz ferromonzodiorite (Fig 8). Texturally, rocks from this category differ from Category 1 based on the predominant subprismatic mineral habit of plagioclase opposed to the felty, decussate plagioclase in Category 1. Whole-rock geochemistry from Category 2 are slightly depleted in magnesium and more enriched in the alkalis relative to the chill and also show enrichment in all trace elements (Fig. 25). Based on the higher proportions of apatite and quartz along with trace element enrichment, this category is interpreted to represent either a more evolved or hybrid/transitional component of the UCZ and “chill”.

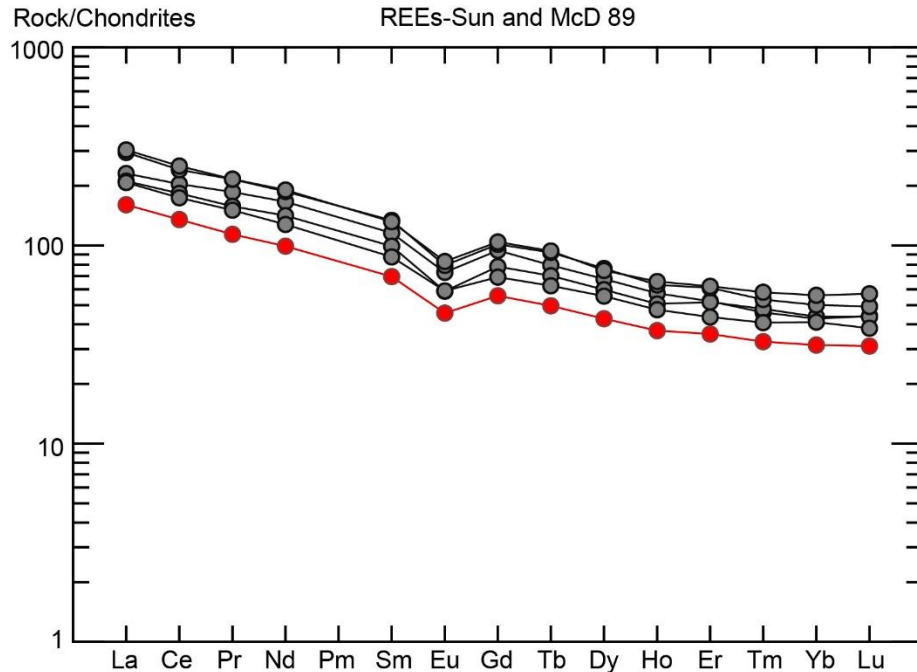


**Figure 25.** Rare earth element variation diagram for Category 2 samples. Red line indicates the DLS “chill” average. REE data are normalized to chondrites reported by Sun and McDonough (1989)

Rock samples comprising category 3 (SSC10A-C) occur in the southwest, at the westernmost extension of the anorthositic mass near Keen Creek. Here the DLS chill forms a narrow contact which abruptly grades into the underlying gabbroic cumulates. Near the gabbro zone contact, sample SSC10A is a medium-grained, intergranular oxide gabbro. Sample SSC10B is a fine-grained ferrodiorite which abruptly grades into medium-grained gabbroic cumulates. Sample SSC10C closely resembles the samples from Category 1 exhibiting non-cumulate mineral assemblages of felty, decussate plagioclase and anhedral to subophitic pyroxene, but is more enriched in trace elements relative to chill (Fig. 26). Based on these petrographic attributes along with the field occurrence, this category is interpreted to mark a transitional zone between the previously formed DLS chill and underlying gabbro zone.

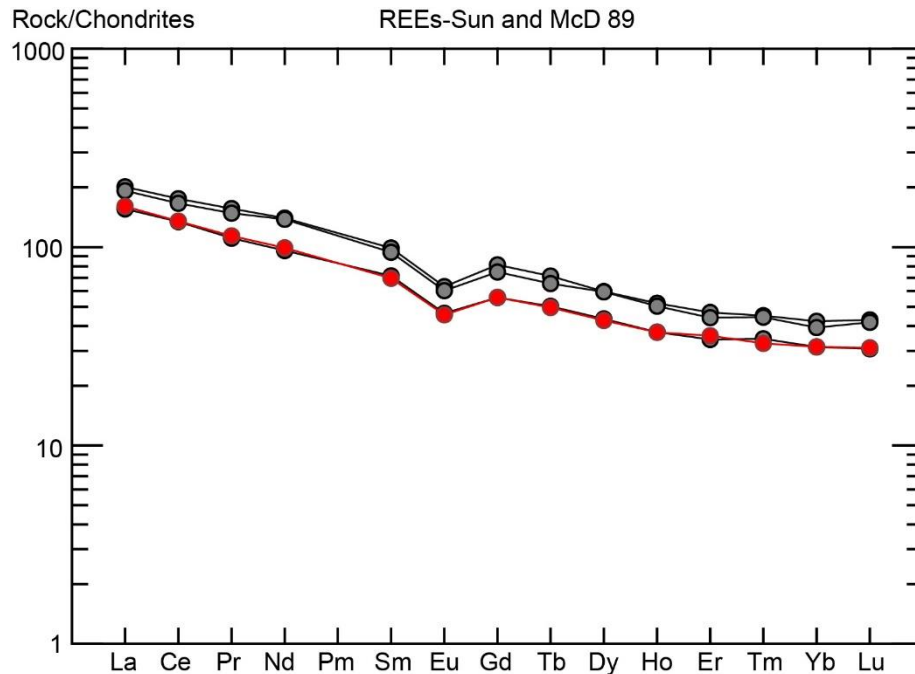


**Figure 26.** Rare earth element variation diagram for Category 3 samples. Red line indicates the DLS “chill” average. REE data are normalized to chondrites reported by Sun and McDonough (1989)

Petrographic observations within the Category 4 samples (SSC6, 7, 8, 9A-C) revealed predominantly gabbroic cumulates. Except for sample SSC6, all samples from Category 4 contained variable amounts of a fine-grained ferromonzodiorite which occurs as pod-like masses forming irregular, gradational contacts with the gabbroic cumulates. The ferromonzodioritic masses exhibit similar textures and mineral assemblages as those from Category 2. Relative to the chill, the REE patterns from Category 4 (Fig. 27) are similar, either showing enrichment or depletion in trace element concentrations. The degree of enrichment or depletion in REE concentrations is likely due to the proportion of gabbroic vs. ferromonzodioritic components within the sample. Previous studies and mapping of the Duluth Layered Series at Duluth (Miller and Green, 2008a, 2008b, and

Green and Miller, 2008) revealed numerous DAS inclusions within the medial and upper portions of the layered series and some of these inclusions can be found in the north eastern portion of the UCZ, corresponding with Category 4 sampling locations. One sample, SSC6, contained no ferromonzodioritic inclusions and was composed entirely of gabbroic cumulates, likely accounting for the vastly different REE pattern. Based on petrography and field occurrence, Category 4 rocks are interpreted to be mixtures of typical UCZ ferromonzodiorite (characteristic of those from Category 2) and ophitic olivine leucogabbro inclusions from the Anorthositic Series.

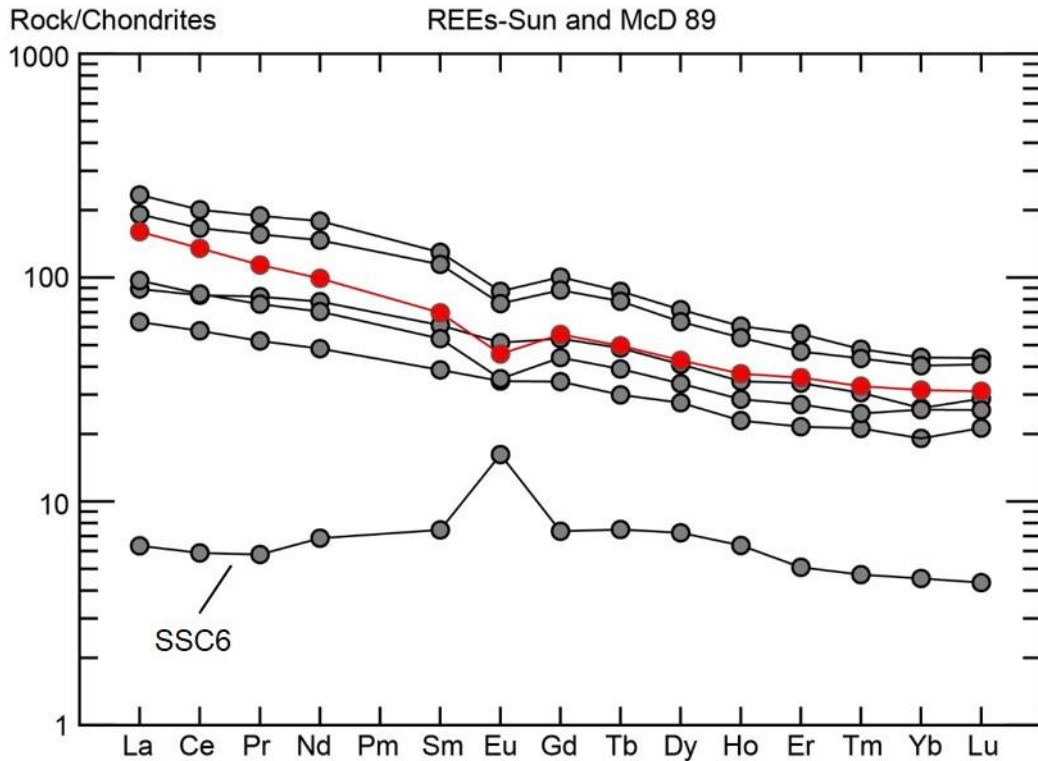


**Figure 27.** Rare earth element variation diagram for Category 4 samples. Red line indicates the DLS “chill” average. REE data are normalized to chondrites reported by Sun and McDonough (1989)

## 5.2 Volcanic Equivalents of the DLS “Chill”

The aborted rifting of the Midcontinent Rift is unique in that both volcanic and shallow plutonic systems are exposed, allowing for studies to examine the extent to which these systems are related, particularly in northeast Minnesota where the Duluth Complex and related intrusions underlie ~ 10 km of similarly aged volcanics. Having suggested that the DLS chill represents a decompressional quench of magma which vented from the layered series magma chamber, it compels one to ask whether the chill composition can be found in the overlying sequence of predominantly basaltic lava flows which form the hanging wall of the Duluth Complex at Duluth. Finding such a correlative lava would provide insight regarding the depth at which the Duluth Complex was emplaced, which can then be used to constrain physical conditions during its evolution and differentiation. Fortunately, Brannon (1984) analyzed the geochemistry of 160 successive lava flows of the NSVG between 2.5 – 6.5 kilometers above the top of the Duluth Complex.

Normalizing Brannon’s (1984) analyses to the average DLS chill composition (Table 5), the data were plotted on spider diagrams in order to identify flows that most closely match the chill composition. Two sequences of flows were identified which had the best match for most major and trace elements. The first sequence contains flow units 28-38 (Fig. 28). While not all of flow units within this sequence fit the chill composition, many exhibit a good match, specifically flow 28 (highlighted in red). The second sequence include flow units 58-65 (Fig. 29), most notable is flow 65 (highlighted in red) which not only shows a good match for most major and trace elements, but is the upper-most flow of



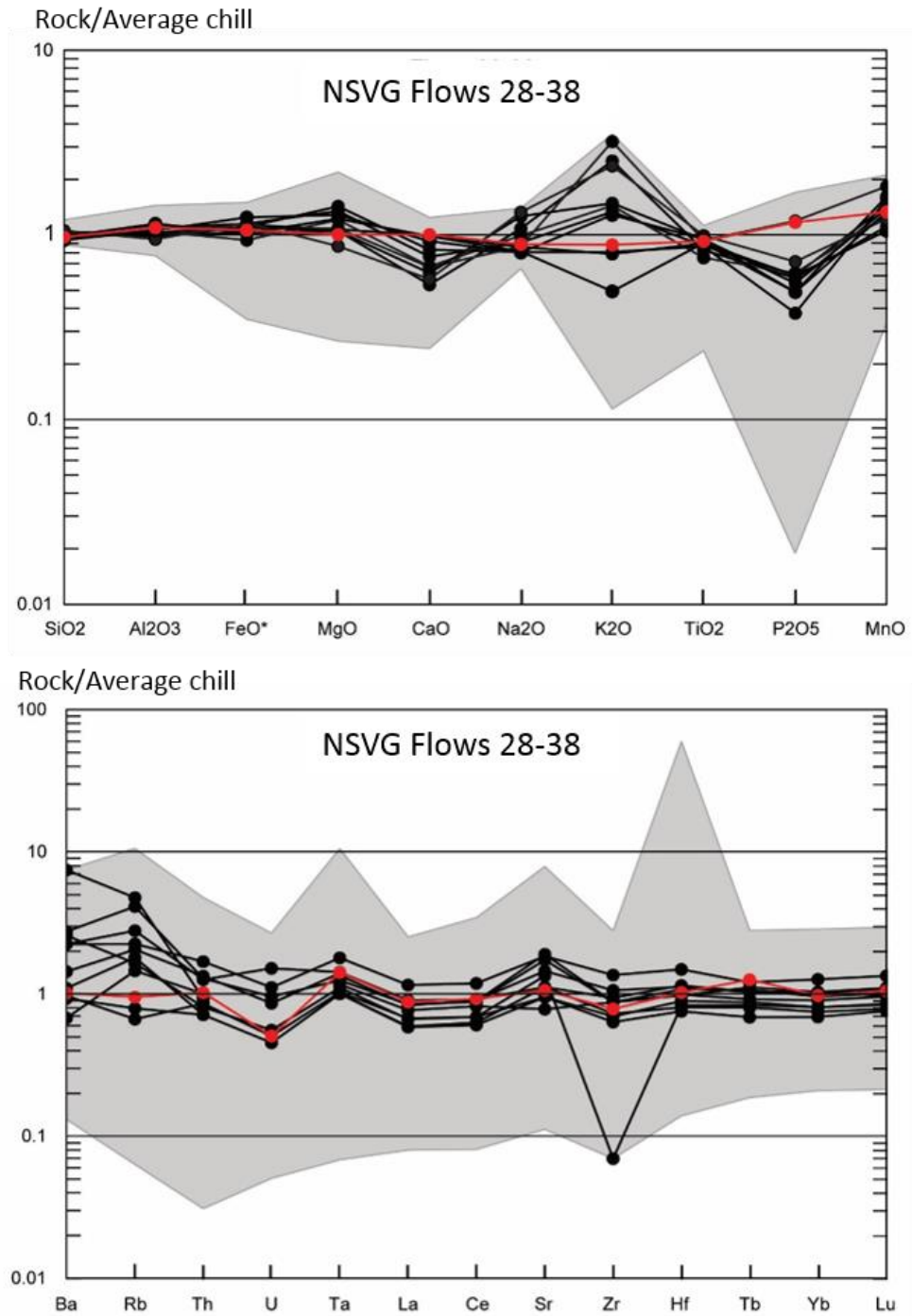


**Figure 28.** Major and trace element spider diagrams for flow sequence 28-38. The grey field contains all samples reported by Brannon (1984). Flow unit 28 is highlighted in red. The average chill composition was used for normalization values (Table 5).

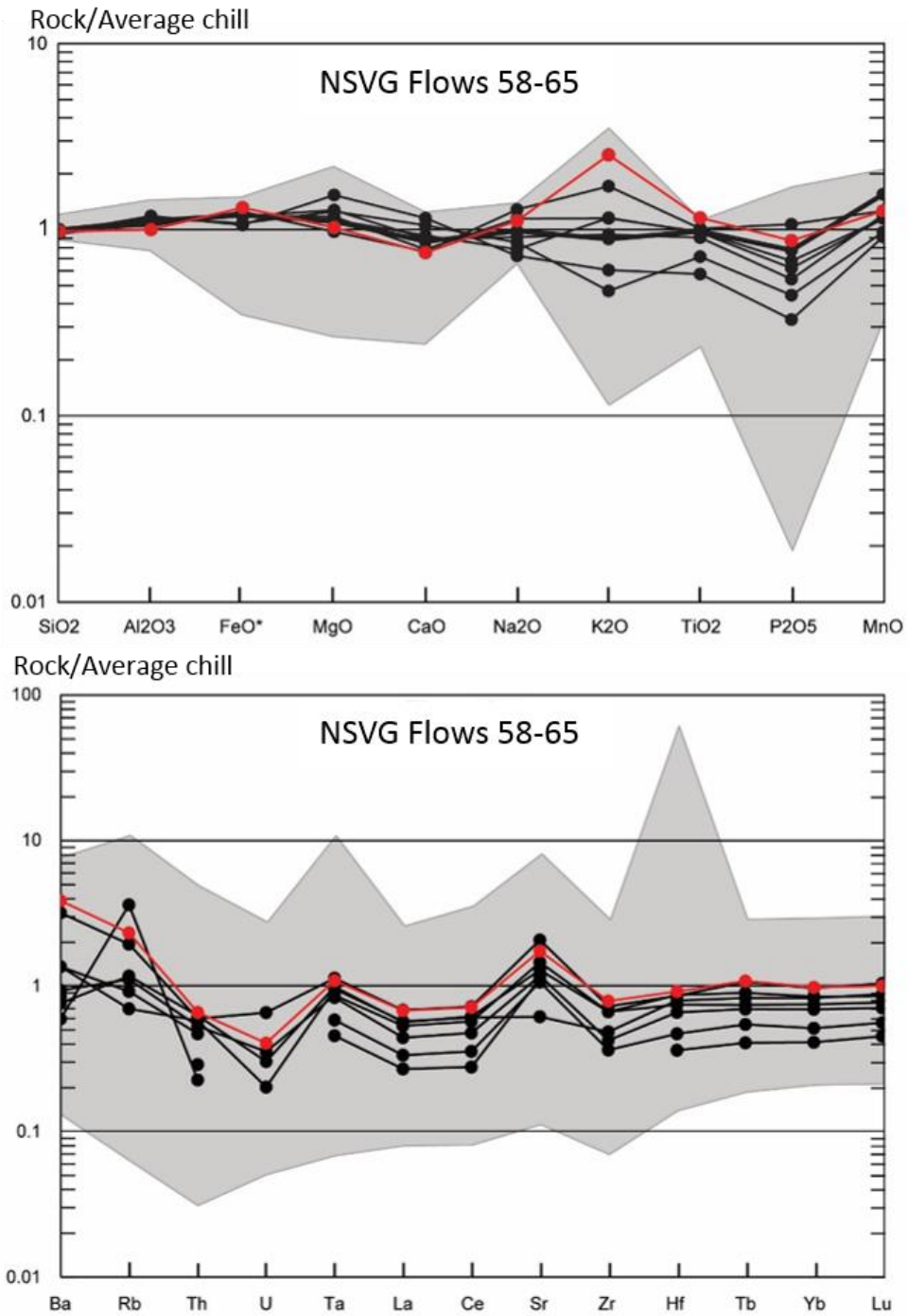


**Figure 29.** Major and trace element spider diagrams for flow sequence 58-65. The grey field contains all samples reported by Brannon (1984). Flow unit 65 is highlighted in red. The average chill composition was used for normalization values (Table 5).

an 8 flow sequence that defines an obvious differentiation trend within the volcanic package and is consistent with a progressively fractionating layered intrusion.

As previously mentioned, these two suites were not completely resampled because of limited exposure due to recent shoreline development. Furthermore, there is slight uncertainty regarding which of Brannon's (1984) original flows were sampled in this study. Sampling locations for Brannon's flows were based on inset maps which were sketched by Brannon and exact sample locations are often difficult to rectify with recent geology maps of these areas (Boerboom et al., 2002a; Boerboom et al., 2002b). Five of the resampled flows (SSV1-5) came from flow sequence 28-38 and two samples (SSV6-7) came from flow sequence 58-65. Samples SSV1-5 presumably correspond with flow units 28, 30, 31, 33, 38 and SSV6-7 to flow units 64 and 65. The seven resampled flow units were plotted on a spider diagram (Fig. 30), along with the average chill composition (shown in red) to evaluate possible matches. Despite showing similar trends in trace element abundance, this figure illustrates the incongruity between selected flow unit and sampling locations. Of the seven collected flows, only two show a good match which presumably correspond to Brannon's (1984) flow units 28 and 31. Two samples were collected from the 58-65 sequence and were inferred to correspond to flow units 64 and 65. Unfortunately, these two samples show the poorest fit to the chill composition, and instead may be from flows higher in the volcanic pile.

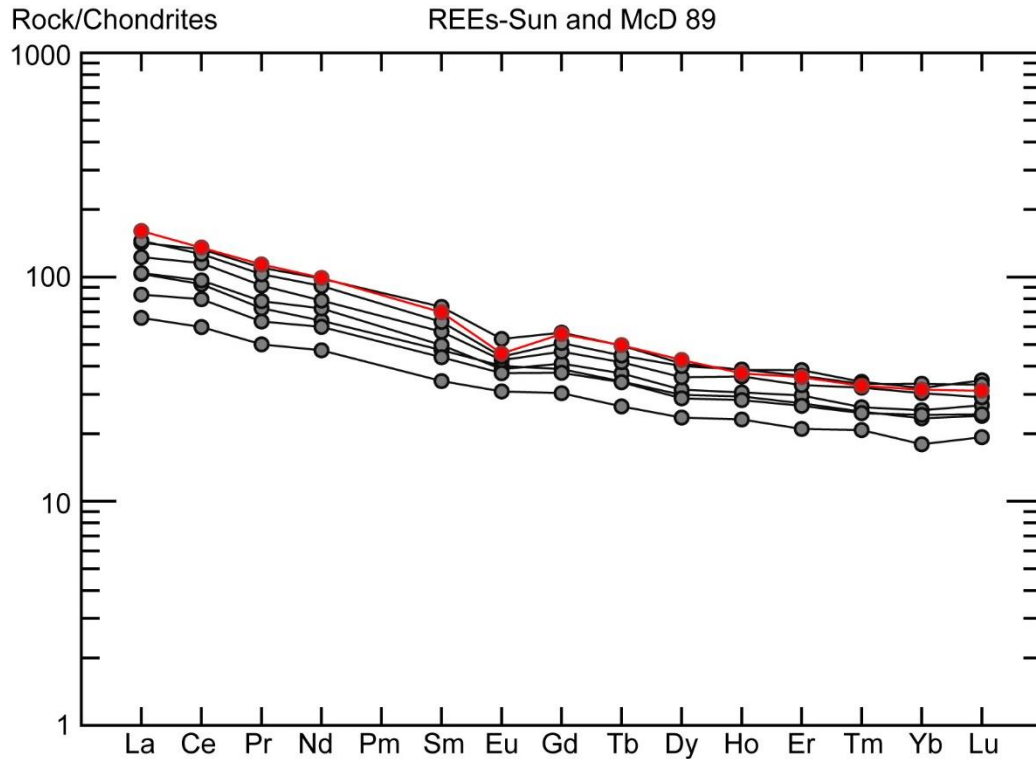


**Figure 30.** Rare earth element variation diagram for new NSVG samples. Red line indicates the DLS “chill” average. REE data are normalized to chondrites reported by Sun and McDonough (1989).

Trace element ratio diagrams (Fig. 31), incorporating the geochemistry of the resampled flows along with corrected values from Brannon’s (1984) data, further illustrate the possible connection between the selected sequence of flows and the DLS chill. Shown as green triangles, a majority of the chill samples show a tight cluster around the average chill composition (red circle). Sample MD279A (gold cross) is also shown as it represents the type chill composition. There is a slight spread in the Hf/Ta ratio within the chill which could be attributed to the amount of biotite/amphibole within the selected samples since Hf and Ta are more compatible in those phases. Despite the

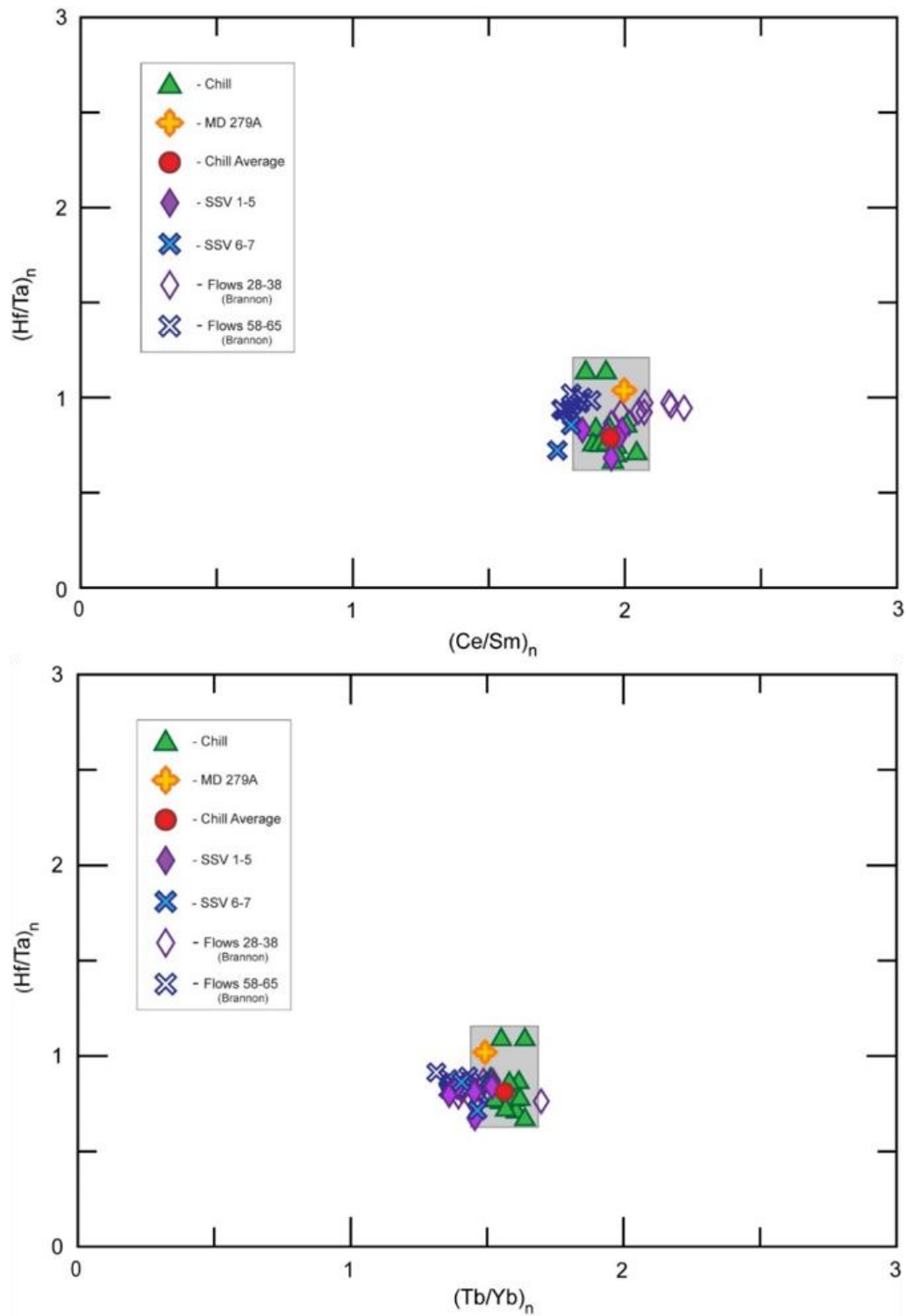


**Figure 31.** Trace element ratio diagram comparing NSVG lavas and DLS chill. Abundances are normalized to chondrite compositions reported by Sun and McDonough (1989).

minor spread, both sequences of flows show a relatively tight cluster within the compositional range of the chill, predominantly around the bulk/average chill samples.

Given the ambiguity between the two sequences of flows, either sequence could be representative volcanic products of the DLS. However, it seems probable that numerous venting events could have occurred during the evolution of the DLS. Considering this, the well differentiated nature of flows 58-65 (Fig. 32) offer persuasive evidence that this sequence of lavas might represent the volcanic products of the DLS.

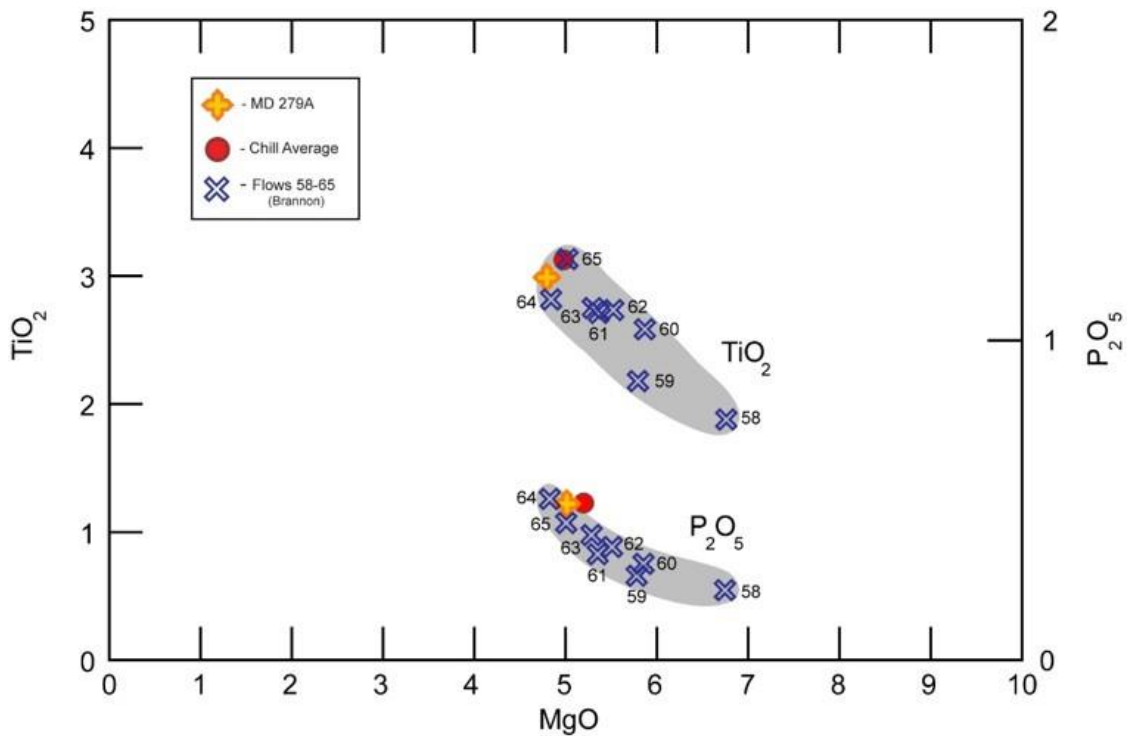


**Figure 32.** Ratio of MgO vs. TiO<sub>2</sub> in flow sequence 58-65 lavas.

Determination of a correlative sequence of lava flows not only provides a rare plutonic – volcanic connection, but more importantly, provides constraints on the depth of emplacement and implications for pressure at the top of the DLS magma chamber. Several subvolcanic mafic dikes and sills associated with the Duluth Complex were emplaced into lava flows which overlie the complex. Three of these sills, Lester River Sill, Endion Sill, and Northland Sill, were emplaced stratigraphically below the lava flows that may represent volcanic equivalents to magmas vented from the DLS, however it is unknown whether these sills pre- or post-date the formation of the lava flows. The Endion Sill is the only intrusion that comes into contact with the Duluth Complex, however, Green and Miller (2008) report that the contact relationships are ambiguous as to which is cutting which. Moreover, attempts by Hoaglund (2010) to date the Endion Sill by U-Pb dating of zircon proved unsuccessful due to isotopic inheritance. If it is assumed that the diabase sills are younger than the Duluth Complex, flow units 28 and 65 are situated approximately 3300 meters and 3850 meters stratigraphically above the upper contact of the DLS, respectively. If the diabase sills are older than the complex, this would add an additional 1125 meters to the hanging wall section. If flow sequences 28-38 or 58-65 are the volcanic products of venting from the DLS, this would indicate a depth of emplacement within the volcanic edifice of about 4450 meters to 4975 meters, or, 4.5-5 kilometers below the surface.

A depth of emplacement between 3.3 and 5.0 kilometers is consistent with estimates for the depths of shallow magma reservoirs beneath mafic volcanic centers, such as Kilauea in Hawaii (2-4 km; Ryan, 1987, 1988) and it also corresponds to zones of neutral buoyancy for basaltic magmas (Ryan, 1987, 1993). Although flow sequence 58-65 would

appear to be the better match because of its progressive differentiation, both sequences are nearly indistinguishable from each other such that matches within sequence 28-38 cannot be discounted. Regardless, a ~500 meter difference in depth of emplacement would be negligible for development of the DLS.

Emplacement of the DLS beneath 5 kilometers of predominantly basaltic lavas ( $\rho \sim 2.90 \text{ g/cm}^3$ ) plus a 1 kilometer-thick cap of gabbroic anorthosite ( $\rho = 2.75 \text{ g/cm}^3$ ) forming the DAS, would yield pressures at the top of the DLS magma chamber of about 1.2 kbar. If the subvolcanic mafic sills are older than DLS this would add an additional 1.125 km thickness of diabase ( $\rho = 2.95 \text{ g/cm}^3$ ) to the volcanic edifice, and would increase the pressure up to ~1.5 kbar. As will be discussed in more detail below, the solubility of water and its effect on the solidus and liquidus temperature of magmas is more extreme at pressures below 2 kbar. As such, the proposed low range in lithostatic pressure, between 1.2 – 1.5 kbar, is a critical factor when evaluating if the formation of the DLS chill and cyclic zone were the result of cyclical fluctuations in lithostatic and volatile pressure within the DLS magma chamber.

### **5.3 Evaluating the Formation of the DLS Chill by Decompression of a Volatile-saturated Magma at Low Pressure**

The evolved composition of the chill and the effectively identical age dates between the DAS and DLS indicate the chill is not the result of thermal quenching of parental DLS magma against an older and cooler anorthositic cap, but instead was formed by decompressional quenching of a hydrous magma attending volcanic venting events.



Important to this interpretation is the presumed saturation of a volatile phase in the DLS roof zone.

### **5.3.1 Evidence of water saturation in the DLS roof zone**

As mentioned previously, based on the different lithologic and structural attributes of the DLS and DAS, these two series had been interpreted to be petrogenetically and temporally distinct. U-Pb dating of zircon has shown that these two rock series are essentially identical in age at  $1099 \pm 0.5$  Ma (Paces and Miller, 1993), but even without this geochronologic evidence, the mineralogy and composition of the mafic rocks “chilled” against the DAS are much too evolved to represent a thermal quench of DLS parental magma. Instead, an alternative hypothesis suggested by Miller and Ripley (1996) might better explain the identical age dates and evolved composition. This hypothesis holds that the chill formed by decompression quenching of a hydrous magma as a result of magmatic venting. That the DLS magma was saturated in volatiles is significant to this hypothesis because decompression under water-saturated conditions at low overall pressures will have a pronounced effect on the liquidus temperature of magmas (discussed below). Evidence hinting that water-saturated conditions existed in the roof zone of the DLS include: 1) the common occurrence of biotite and amphibole in the chill, and 2) the intense hydrothermal alteration of DAS roof rocks and related DAS inclusions found within medial parts of the layered series.

The presence of biotite phenocrysts is the strongest evidence that the magma in the roof zone was water-saturated or near saturated at the time of quenching, as experimental studies indicate that water-saturated or near-saturated conditions are necessary for the phase stability of biotite in basaltic to intermediate magmas (Wones and Eugster, 1965).

Titaniferous biotite phenocrysts ( $\text{TiO}_2 = 4\text{-}5.5$  wt.%) compose 2-10 modal % of the fine-grained ferrodiorite, and typically occur either as 3 – 5 mm, subpoikilitic to anhedral granular clots, intergranular crystals or as overgrowths on ilmenite and pyroxene.

Primary hornblende and amphibolitic alteration of primary pyroxene (hornblende to actinolite) is also present in most of the chill rock and locally amphibolitization is nearly complete. As with biotite, relatively high amounts of water are necessary to stabilize amphibole (Berndt et al., 2004). The porphyritic occurrence of biotite suggests it was a liquidus phase at the time the rock was quenched and the abundant amphibole alteration of primary pyroxene along with interstitial or overgrowth textures of biotite suggest water saturation was achieved simultaneously with or during the later stages of crystallization.

The intensity and spatial distribution of hydrothermal alteration of DAS hanging wall rocks and DAS inclusions also allude to the build-up of a volatile fluid in the DLS roof zone. Locally, complete alteration of primary silicates is observed within the DAS, especially where the DAS rocks are in direct contact with the chill and where DLS intrusions cut the anorthositic rocks. Alteration within the DAS takes the form of commonly complete uralite and chlorite replacement of pyroxene, serpentine, talc, oxide and iddingsite alteration of olivine and sericite, zeolite, epidote and calcite (sausseritic) replacement of plagioclase. This diverse assemblage of alteration phases suggest a prolonged period of hydrothermal alteration over a broad temperature range. Despite the minor amphibolitic alteration of primary pyroxene, the chill shows only minor alteration of plagioclase and oxide which suggests that a volatile phase existed prior to the formation of the chill. Further evidence suggesting that a volatile phase existed before the formation of the chill is the occurrence of DAS-related inclusions within relatively

unaltered cumulates in the cyclic and gabbro zones of the DLS that display similar alteration assemblages as those of the DAS roof rocks. Presumably, these inclusions became detached from the DAS roof and settled to the cumulate floor during the medial stage of DLS crystallization, further suggesting volatile saturation existed prior to or contemporaneously with the formation of the cyclic zone, providing additional constraints on the timing of the build-up of a volatiles in the DLS roof zone.

### **5.3.2 Effects of decompression under water-saturated conditions**

Experimental studies on the melting relations in the system  $\text{NaAlSi}_3\text{O}_8 - \text{H}_2\text{O}$  demonstrate the influence of  $\text{H}_2\text{O}$  on solidus and liquidus temperatures of silicate melts at varying water pressures (Burnham and Davis, 1974). These studies show that the liquidus temperature decreases with decreasing pressure at water-undersaturated conditions; however, at water-saturated conditions, the liquidus temperature increases with decreasing pressure (Fig. 33). If the magma was water-undersaturated at the time of decompression, this might cause a hiatus in crystallization or possibly resorption of some or all of the mineral phases. In a water-undersaturated magma that is multiply saturated in solid phases, decompression may result in a shift in phase boundaries leading to a decrease in the number of saturated phases (e.g.,  $\text{Pl} + \text{Ol} \rightarrow \text{Pl}$  only). Conversely, decompression under water-saturated conditions would result in an increase in the overall liquidus temperature of the magma, which would lead to instantaneous undercooling, effectively quenching the magma. This effect is even more pronounced at low pressures (< 2 kbar) which are thought to have existed during the formation of the DLS.

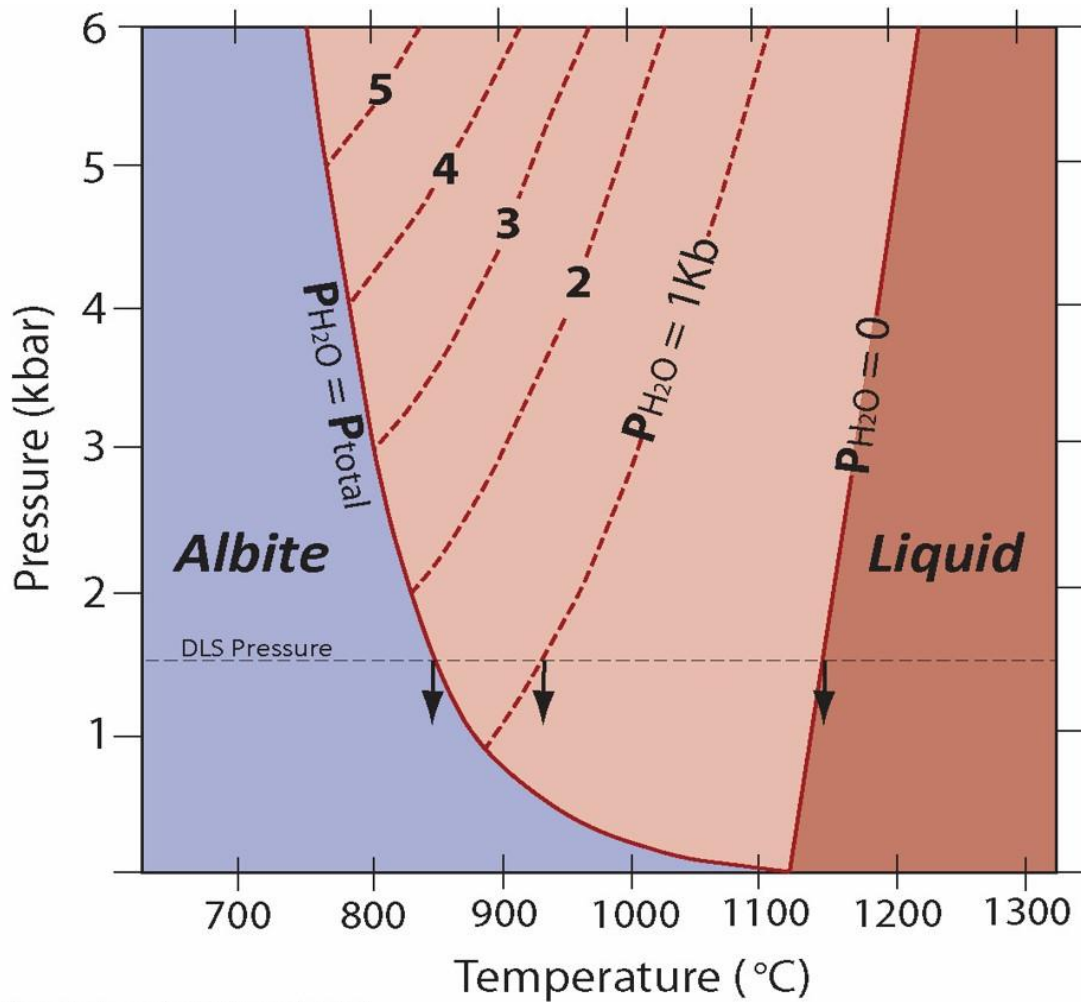


**Figure 33.** The effect of H<sub>2</sub>O saturation on the melting of albite. After Burnham and Davis (1974).

While decompression quenching of a water-saturated liquid can be shown to occur in the albite-water system (Fig. 31), a question arises as to whether a similar result would be expected from a multi-component natural magma. The geochemical modeling program PELE (Boudreau, 1999) is useful for testing different phenomena in natural magmatic systems and was used to model the effects of decompression on the chill composition. This process was modeled as follows: Sample MD279 was used as the input bulk-rock

composition, as this sample represents the type chill composition. Starting with 0 wt.% H<sub>2</sub>O, the liquidus temperature of the system, determined by PELE, was recorded in 100 bar increments between 1 bar – 1800 bars lithostatic pressure. This process was then repeated, increasing the water content of the chill from 0.5 wt.% - 3.5 wt.% H<sub>2</sub>O. Based on the input bulk rock composition, PELE is able to determine the amount of water required to achieve saturation in the magma. Utilizing this function, the liquidus temperature was then recorded over the pressure range with the determined amount of water to achieve saturation. The determined values are listed in Table 3b.

A plot of the recorded liquidus temperatures (Figure 34) shows that PELE sufficiently models and recreates the proposed effect of decompression at water saturation using the chill composition. As shown, when the chill is water understated (0.5 – 3 wt.% H<sub>2</sub>O) the liquidus temperature decreases with decreasing pressure. Once the magma is saturated in water, however, the liquidus temperature increases with decreasing pressure such that rapid decompression of the DLS at any temperature below ~1100 °C, as might be expected during a volcanic venting event, would result in quenching of the saturated mineral phases to form the DLS chill.

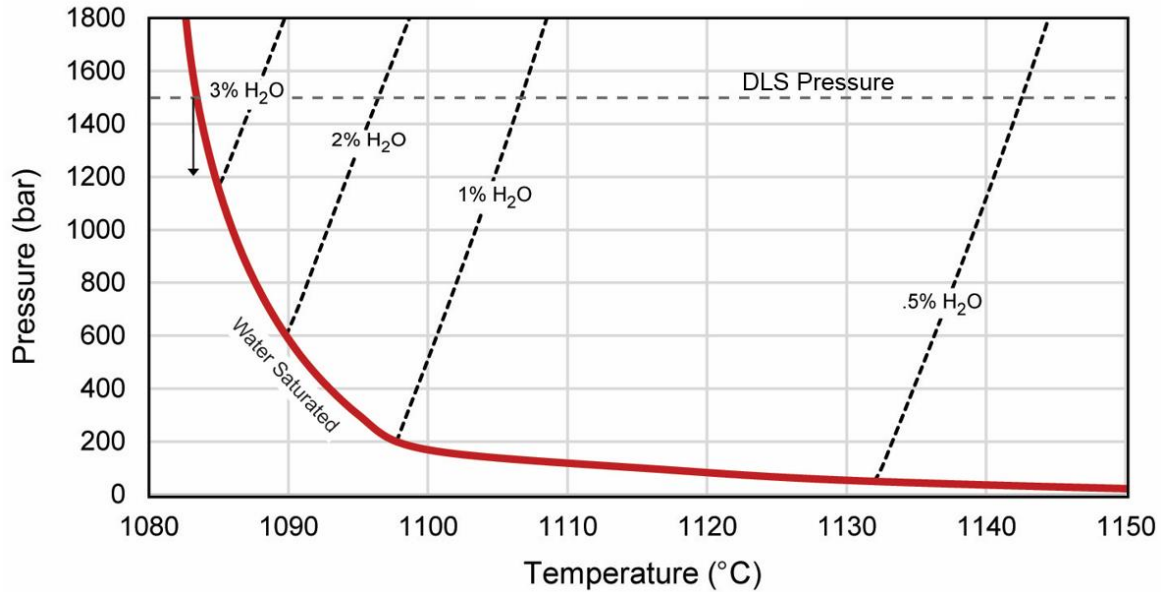


**Figure 34.** Decompression experiments performed to verify the effects of water on the liquidus temperature and the effects of decompression under low pressure at water saturated conditions.

### 5.3.3 Development of volatile saturated conditions in the DLS magma system

Devolatization within shallow magma chambers resulting in overpressures exceeding the tensile strength of the chamber roof is commonly cited as a major cause of volcanic eruptions in basaltic, intermediate and felsic systems (Wilson and Head, 1981; Tait et al., 1989; Bottinga and Javoy, 1989). Furthermore, once saturated, the more soluble a volatile species is, the more important is its role in developing overpressures. Tait et al. (1989) demonstrated that H<sub>2</sub>O is a critical component of the gas phase, more so than CO<sub>2</sub>, to generate overpressures because H<sub>2</sub>O has a greater solubility than CO<sub>2</sub>. The presence of biotite and amphibole along with the intense alteration in the DAS roof rocks indicate water-saturated conditions existed at least in the roof zone of the DLS magma

chamber, but how was water saturation achieved if tholeiitic basalt is commonly thought to be water – undersaturated (~0.5 wt.%; Moore, 1970) at most crustal pressures (Burnham, 1980; Dixon et al., 1989; Johnson et al., 1994)? Several processes acting within the DLS magma could have led to the development of water-saturated conditions, at least in the roof zone of the DLS magma chamber during the intermediate stage of its crystallization and specifically at the time of cyclic zone formation. These include: 1) high initial water content of the parental magma, 2) H<sub>2</sub>O enrichment by fractional crystallization, 3) H<sub>2</sub>O enrichment by CO<sub>2</sub> degassing and 4) shallow level of emplacement.

As mentioned, tholeiitic MORB basalts are commonly regarded as being undersaturated in H<sub>2</sub>O. However, water behaves like other incompatible elements in silicate melts and would be expected to be more abundant in enriched magmas, such as plume-fed EMORB basalts (Dixon et al., 1988; Jambon and Zimmerman, 1990). Since MCR magmas are proposed to have derived from an enriched mantle plume (Hutchinson et al. 1990), it is reasonable the DLS parental magma would have had an initial water content similar to that of an enriched oceanic basalt (~0.8 wt.%; Johnson et al., 1994). Furthermore, emplacement of the Duluth Complex into water-bearing lava flows may have also contributed additional water to the magma.

Fractional crystallization is another process which could have resulted in water saturation as the DLS differentiated. Based on the solubility of water in basaltic magmas, at lithostatic pressure at the top of the DLS about 3.5 wt.% water would be needed to be saturated in the magma (Hamilton et al. 1964; Shiskina et al., 2010). If water has a bulk partition coefficient (D) of about 0.01, suggested based on observations between water

and other incompatible elements in mafic magmas (Dixon et al. 1988), enrichment from 0.8 wt.% to 3.5 wt.% H<sub>2</sub>O would require a substantial degree of fractional crystallization as modeled by the Rayleigh distillation equation:

$$C_l = C_o * F^{(D-1)}$$

Here C<sub>l</sub> is the concentration in the remaining liquid, C<sub>o</sub> is the initial concentration in the parental magma, F is the fraction of melt remaining, and D is the bulk partition coefficient (0.01). Replacing C<sub>o</sub>, F and D with known values we can see that between 75-80% Rayleigh-type fractional crystallization is needed to reach saturation.

$$C_l = 0.8 * 0.25^{(0.01-1)}; C_l = 3.156\%$$

$$C_l = 0.8 * 0.20^{(0.01-1)}; C_l = 3.936\%$$

However, in open systems, which the DLS is presumed to be based on evidence of liquid recharge, enrichment in incompatible elements can be enhanced (O'Hara and Mathews, 1981) as the influx of new magma would introduce additional concentrations of incompatible elements and prolong crystallization processes, further enriching concentrations within the magma chamber. Either through simple fractional crystallization, or by recharge and fractional crystallization, the magma will become enriched in incompatible elements, especially in the roof zone if the magma chamber becomes compositionally zoned.

The presence of CO<sub>2</sub> within the magma can also result in the development of a volatile phase, at least in the roof zone, due to CO<sub>2</sub> fluxing. Experimental studies on the solubility of volatiles in basaltic magmas indicate that a tholeiitic MORB will be CO<sub>2</sub>-saturated at all crustal pressures (Dixon et al., 1988; Dixon and Stolper, 1995; Bottinga and Javoy 1989, 1990; Sisson and Grove, 1993; Johnson et al., 1994; Duan, 2004), such



that through fractional crystallization, CO<sub>2</sub> should be continuously degassing from the DLS magma. Despite being initially saturated, studies show that bubble nucleation will not occur until supersaturated levels have been reached (>1.5; Bottinga and Javoy, 1989, 1990). Once supersaturation has been achieved, bubbles will then nucleate, grow and rise to the roof zone of the magma chamber. Despite being undersaturated in the magma, CO<sub>2</sub> gas-fluxing removes dissolved H<sub>2</sub>O from the melt (Johnson et al., 2008, 2010) and the dissolved H<sub>2</sub>O will be partitioned into a volatile phase at a concentration equal to its partial pressure in the magma.

Thermodynamic model calculations on the albite-H<sub>2</sub>O-CO<sub>2</sub> system, indicate that as the concentration of H<sub>2</sub>O within the system increases, the partition coefficient between the fluid and melt changes from <1 to >1. Furthermore, the concentration at which H<sub>2</sub>O changes from incompatible to compatible within the fluid phase is less at lower pressures (Burnham and Davis, 1974; Holloway, 1976). The increased compatibility of water into the fluid phase, combined with H<sub>2</sub>O partitioning into degassing CO<sub>2</sub> – dominated bubbles which rise to the higher portions of the magma chamber could result in enrichment of water in the roof zone.

Lastly, that the DC was emplaced shallowly within the volcanic edifice, presumably 4.5 – 5 km (discussed below), is a cogent feature in the development of the DLS chill. Pressure, more so than temperature and magma composition, has a pronounced effect on the solubility of water in magmas (Botcharnikov et al., 2005). The solubility of water in basaltic magmas is approximately a function of the square root of pressure (Hamilton et al., 1964). As shown in Figure 35, for lithostatic pressure at the top of the DLS of about 1.5 kbar (discussed below), the amount of water needed to reach saturation on the solidus

is about 3.5 wt.%. As previously discussed, if the parental magma had an initial water content of about 0.8 wt.%, a four-fold increase in the concentration of water would be needed to become saturated. However, even if the magma had not reached water-saturation prior to decompression, a drop in pressure would lower the solubility of water in the melt, effectively bringing it into saturation at which point the water concentration in the melt will follow the water solubility curve to lower pressures ( Dixon and Stolper, 1995).

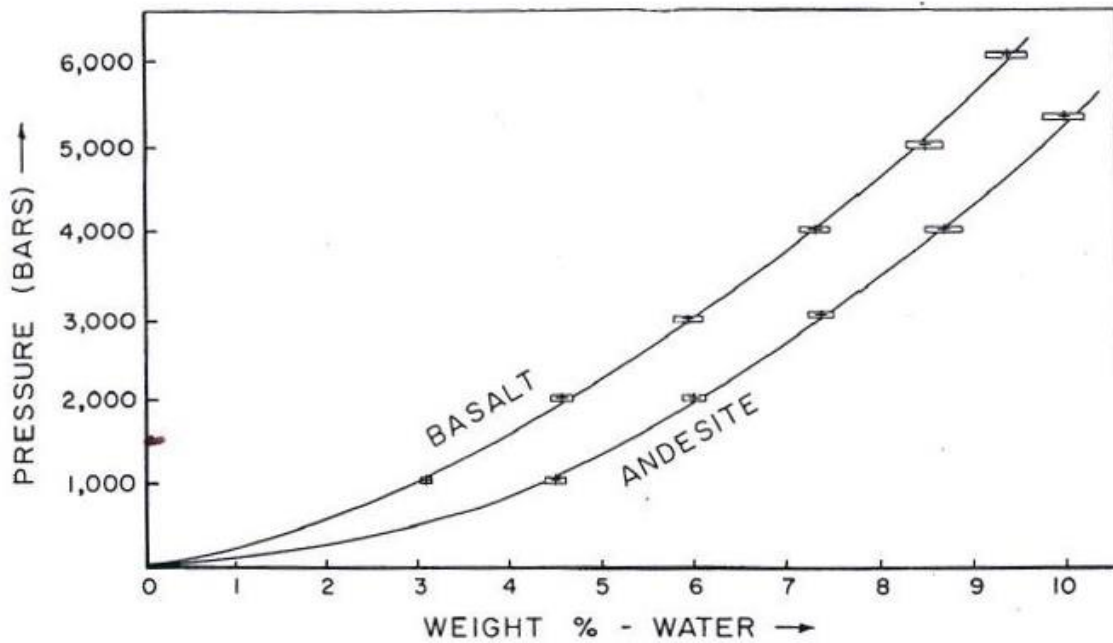


**Figure 35.** The solubility of water in Columbia River basalt and Mount Hood andesite melts as a function of water pressure at 1,100 ° C. From Hamilton et al. (1964).

All of these processes will have significant effects on pressure within the magma chamber, which will prove to be an important concept when considering formation of the cyclic zone. Pressure fluctuations expected to result from devolatilization and decompression from the DLS would probably be on the order of 125-300 bars (Fig. 36). Assuming no overpressures, a change in pressure due simply to venting is the difference between the lithostatic pressure of rock above the chamber and the pressure of a column of magma or,

$$\Delta P = (\rho_{rock} - \rho_{magma}) \cdot g \cdot d$$

where  $g$  is the acceleration due to gravity ( $0.098 \text{ cm/s}^2$ ) and  $d$  is the depth at the top of the DLS or 5 km. Assuming the volcanic edifice is composed of predominantly basaltic lavas,  $\rho_{rock} \sim 2.90 \text{ g/cm}^3$ , and the density of a column of magma ( $\rho_{magma}$ ) of approximately  $2.65 \text{ g/cm}^3$  the total amount of decompression from simple venting would be:

$$\Delta P = (2.90 - 2.65) \cdot 0.098 \cdot 5000$$

$$\Delta P = 122.5 \text{ or } \sim 125 \text{ bar}$$

However, unless the system is in tension, overpressures ( $P^+$ ) are needed in order to initiate venting. The maximum amount of overpressures needed is equal to twice the tensile strength of the volcanic edifice:

$$P^+ = 2 \cdot t$$

where  $t$  equals the tensile strength of basalt ( $\sim 90 \text{ bars}$ ). Considering this, the maximum amount of overpressure needed would be approximately 180 bars.

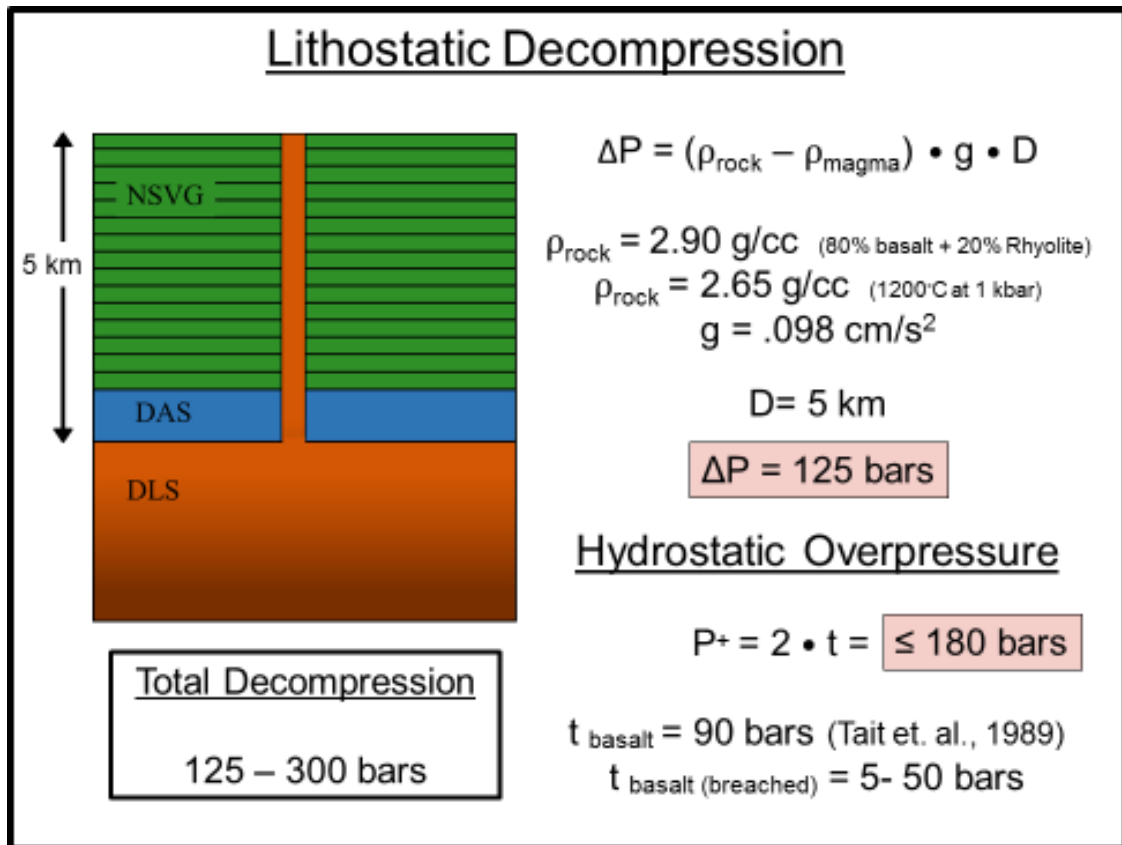


**Figure 36.** Calculations determining pressure fluctuations expected from devolatilization and decompression with the DLS.

Numerous processes have been cited as triggering mechanisms for volcanic eruptions including magmatic recharge, crystallization resulting in devolatilization, and increased buoyancy of the magma (Blake 1989; Tait et al. 1989, Pinkerton et al. 2002), all of which may have been occurring within the DLS magma chamber. Progressive differentiation due to fractional crystallization of the DLS system would result in the melt becoming saturated with respect to volatiles, leading to degassing of  $\text{CO}_2 + \text{H}_2\text{O}$  and an increase in the total pressure. Enrichment of a gas phase within the magma would also effectively lower the density of the magma due to the increase in molar volume of the

gas. An influx of new magma into the system would also increase pressure due to compression of the liquid and expansion of the chamber, but recharge would also introduce additional volatile species into the system. Furthermore, all of these processes will have a more dramatic effect at lower pressures, at which the DLS presumably formed.

#### **5.4 Correlation of the DLS Chill and DLS Cumulates.**

Discussed previously, the chill composition should initially crystallize a cumulus mineral assemblage of plagioclase, augite and Fe-Ti oxide (Miller and Ripley, 1996), making them more comagmatic with PCF±O cumulates of the cyclic and gabbro zone. To the southwest, near Keene Creek, the UCZ/chill forms a narrow contact between a large anorthositic mass, detached from the DAS, and underlying gabbroic cumulates. It is also into this DAS inclusion that the type DLS chill intrudes. While it is hypothesized that the chill is in equilibrium with the microgabbro intervals within the cyclic zone, these field relations question whether, instead, the chill formed during gabbro zone crystallization and the anorthositic block detached during a venting event. In order to test whether the chill is in equilibrium with the gabbro zone, PELE was used to calculate mineral chemistries of saturated phases expected to crystallize from the chill composition. These runs were completed simulating processes at 1500 bar lithostatic pressure, and QFM conditions along with variable water content from 0 – 3.5 wt.% H<sub>2</sub>O (Fig. 37). Compared to the mineral chemistries of the gabbro zone, only at dry conditions do the minerals expected to crystallize from the chill correspond with those from the gabbro zone. With the addition of more water, the minerals produced from the chill become more

magnesium rich than those in the gabbro zone. From these model runs, it is apparent that the minerals expected to be produced from the chill are not in equilibrium with the gabbro zone cumulates, and instead, as will be discussed further below, are more appropriately comagmatic with microgabbro cumulates from the cyclic zone.

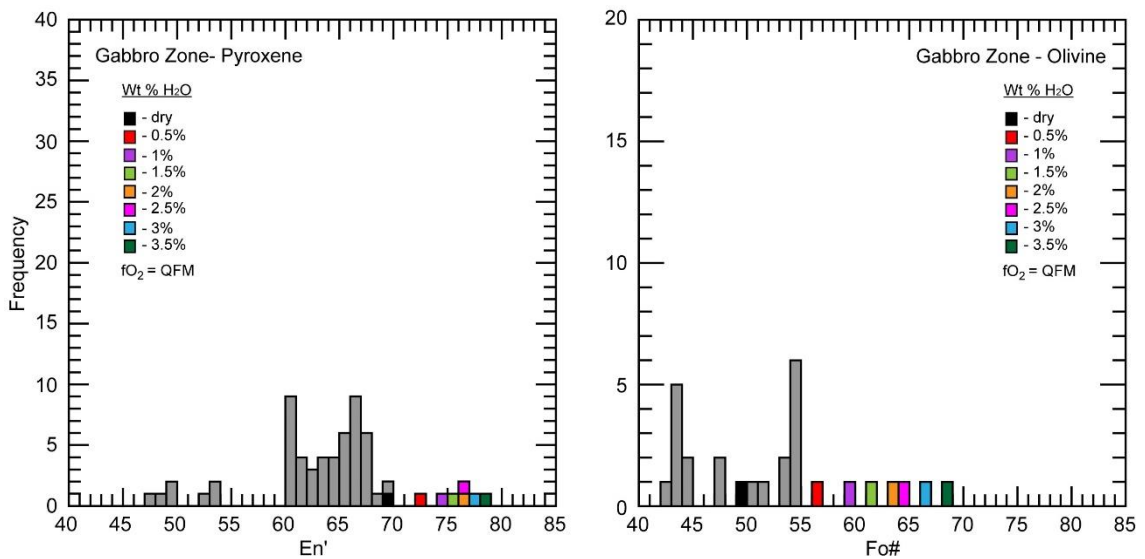


**Figure 37.** Mineral chemistries for augite and olivine determined by PELE at 1500 bar lithostatic pressure and QFM conditions. Grey bins are pyroxene and olivine values determined from microprobe analyses from gabbro zone samples.

### 5.5 Formation of the Cyclic Zone

Having shown from mineralogy and mineral chemistry that the chill is more appropriately comagmatic with PCOF cumulates with the cyclic zone rather than gabbro zone cumulates, other features and attributes of the cyclic zone are also better explained

by the same processes proposed for the formation of the DLS chill – namely, decompression and degassing of a volatile-saturated magma due to venting. The specific features of the cyclic zone to be considered are phase and cryptic layering of the macrocyclic units and the occurrence of microgabbro and anorthositic series xenoliths at the tops of macrocyclic units. The results strongly support the interpretation that the DLS chill and the cyclic zone formed contemporaneously.

### **5.5.1 Phase and Cryptic Layering of the Cyclic Zone**

The cyclic zone of the DLS is a ~ 1 km- thick zone exhibiting cyclical variations in cumulus mineral assemblages which transition from two phase troctolitic cumulates (PO) to three or four phase olivine gabbro cumulates (PCOF) (Fig. 38). Boundaries between the macrocycles are commonly sharp and at the tops of most of the macrocycles is the occurrence of a fine-grained, intergranular oxide-olivine gabbro, or microgabbro. These cyclic variations in cumulate phase layering would appear to be readily explained by progressive fractional crystallization interrupted by magmatic recharge as such processes are commonly used to explain similar macrocyclic phase layering in many other mafic layered intrusions (Wager and Brown, 1968; Irvine 1975). Magmatic recharge could also explain the microgabbro occurrences if they were considered to be intraplutonic quench zones formed by the rapid cooling of recharged magma beneath a cooler resident magma (Tegner et al. 1993; Weibe and Snyder, 1993). However, several features within the cyclic zone (irregular cryptic variation, abrupt phase reversals, microgabbro intervals and occurrence of altered DAS-like inclusions) do not correspond

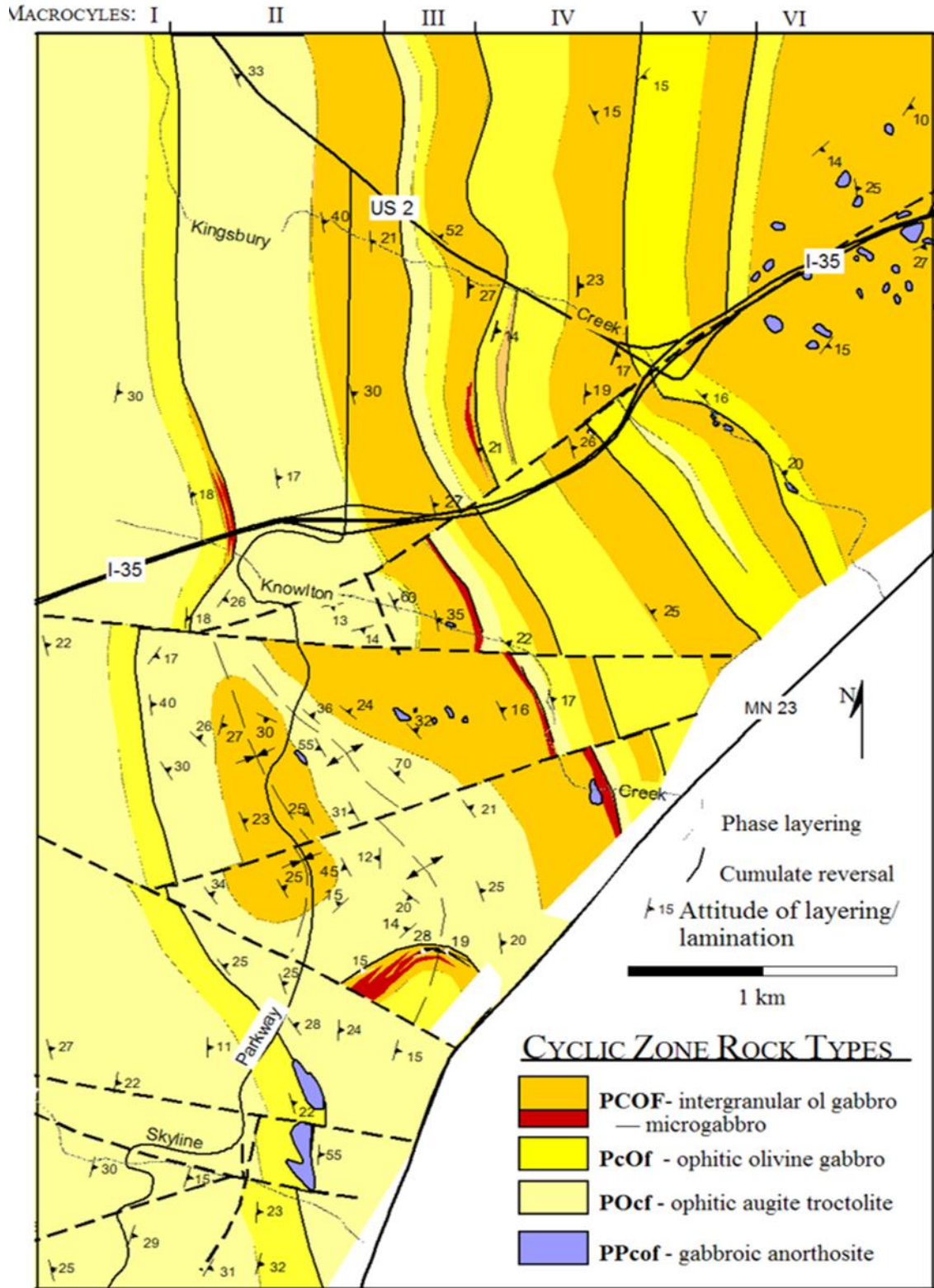


Figure 38. Geology of the cyclic zone of the DLS. From Miller and Ripley (1996).



with a model of fractional crystallization interrupted by recharge. Rather, these features are better explained by fluctuations in fluid pressure due to crystallization and magmatic venting (Miller and Ripley, 1996).

If solidification occurred by a process of fractional crystallization interrupted by magmatic recharge, the progressive and regressive phase layering should exhibit corresponding reversals in cryptic variation. However, not only is cryptic variation minor between the macrocycles, there is also a lack of correlation between phase layering and cryptic layering, especially at the cumulus phase reversals (Fig. 39). Considering magmatic recharge, a progression from PO to PCOF cumulates should be matched by a similar progression in cumulus mineral cryptic variation such that the *mg#* should be higher in the PO cumulates, becoming progressively lower during PCOF crystallization. Recharge of a more primitive magma would shift the composition back to equilibrium with only plagioclase and olivine, resulting in crystallization of PO cumulates (phase reversal) and a shift to higher *mg#*. However, at many macrocycle boundaries, the transition from PCOF – PO cumulates results in a decrease in *mg#*, contradicting a magma recharge model. Conversely, this lack in cryptic variation does not disprove magma recharge, however, if responsible for the phase regression it would require limited volumes of a lower density magma, relative to the resident magma, which were emplaced as well-mixed plumes.

The abrupt phase transition from PO to PCOF cumulates is also difficult to explain by fractionation and recharge. Generally within macrocycles, the PO cumulates contain little interstitial augite and oxide up to within a few meters of the cumulus arrive of all four phases. Within this interval, high density subpoikilitic clots of pyroxene and is

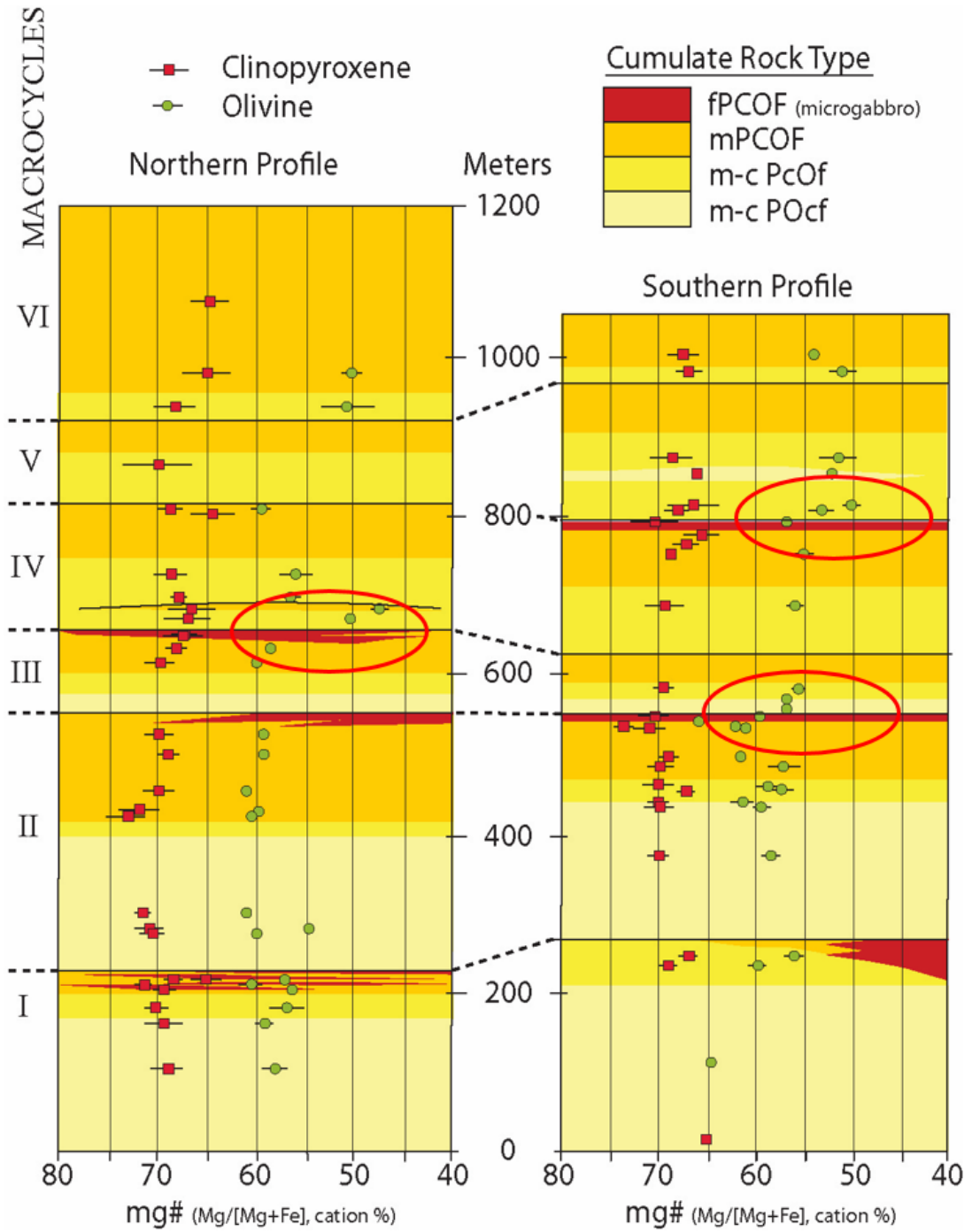


**Figure 39.** Cryptic variation in  $mg\#$  in olivine and augite. From Miller and Ripley (1996).

oxide appear, indicating their imminent saturation. The contacts between cumulus phases typically gradational on a scale of a few meters. If by simple fractionation/recharge, the cumulus assemblage of augite and oxide should be signaled by their gradual interstitial build-up as poikilitic oikocrysts. There also should be gradual decrease in mg# of the mafic phases across this transition which is not observed.

In contrast, the abrupt phase transitions and contradictory cryptic variation are better explained by gradual increases in fluid pressure due to magma venting. Having previously cited evidence for the development of volatile saturated conditions in the DLS magma system leading to the formation of the DLS chill, this build-up of a volatile phase would result in increasing the pressure within the chamber. Eventually fluid overpressure are achieved leading to failure of the roof zone and magmatic venting, which would result in abrupt decompression and degassing and a return to lithostatic pressure.

Although the DLS was initially saturated in plagioclase and olivine forming PO cumulates of the troctolite zone, fractional crystallization would have brought the magma close to saturation in augite and Fe-Ti oxide. If volatile saturation of a CO<sub>2</sub>/hydrous fluid phase was achieved near the end of the troctolite zone crystallization, degassing would have led to a gradual increase in pressure. As shown by the model Plag-Oliv-Cpx system in figure 40, increasing pressure has the effect of expanding the pyroxene liquidus field relative to plagioclase and olivine (Sisson and Grove, 1993; Métrich and Rutherford, 1998). Therefore, the increased pressure effect may have resulted in the early onset of augite (an oxide) saturation and to their appearance as cumulus phases and PCOF crystallization. The abrupt transition back to PO crystallization may reflect a return to lithostatic pressure after venting, resulting in rapid decompression and degassing, thereby

shrinking the pyroxene liquidus field and shifting the phase equilibrium back to saturation in only plagioclase and olivine. Eventually, fractional crystallization would drive pressure to increase again as gas exsolves from the magma, leading to another venting event, and formation of subsequent macrocycles.

Studies have shown that small changes in pressure and water content have noticeable effects on the phase equilibrium of mafic magmas; however, small shifts in pressure have negligible effect on mineral compositions (Baker and Eggler, 1987; Sisson and Grove, 1993). Therefore, the abrupt cumulus phase transitions and lack of corresponding cryptic variation are better explained by periodic pressure fluctuations, instead of by magmatic recharge.

In order to evaluate this model more rigorously, PELE was used again to evaluate the effect of pressure fluctuations on the stability of pyroxene. This process was modeled as follows: Sample MD279 was again used as the input bulk rock composition for all runs. The starting temperature was set based on the calculated liquidus temperature of the input bulk composition at 1500 bar lithostatic pressure. Allowing PELE to run in 1°C steps, the temperature at which plagioclase, olivine and clinopyroxene first became saturated were recorded. Next, while using the same starting temperature, runs were completed at 1600, 1700 and 1800 bar (representing maximum proposed pressure increase, discussed above) and the saturation temperature of clinopyroxene was recorded. This process was again repeated at different water contents. Recorded values are presented in Table 3a.

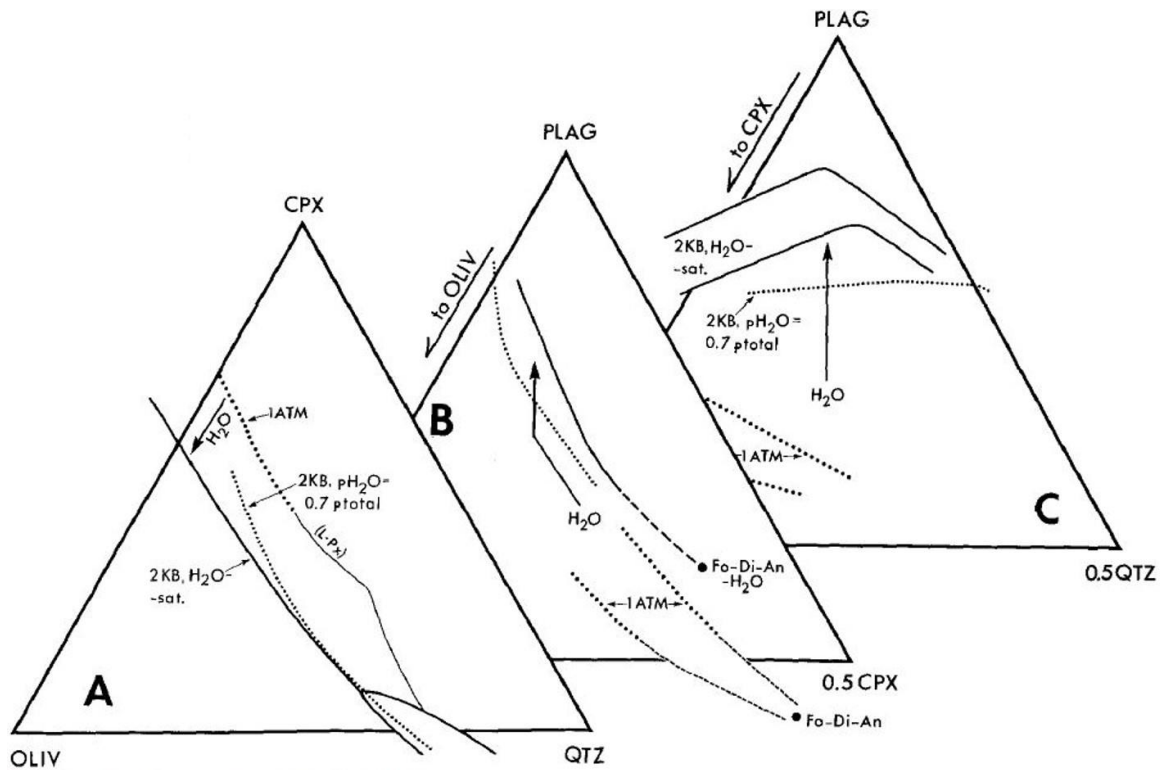


**Figure 40.** Pseudo-ternary projections illustrating the influence of  $p_{H_2O}$  on the position of phase boundaries (from Sisson and Grover, 1993).

Plotting the recorded liquidus temperatures in Figure. 41, PELE predicts the proposed expansion of pyroxene stability due exclusively to increasing pressure. Panel A in Figure 41 shows the initial liquidus temperatures of plagioclase, olivine and clinopyroxene at 1500 bar and variable water contents. At low water contents (0.5 wt.%) plagioclase is the first saturated phase followed by olivine and then clinopyroxene. Studies show the addition of water to a basaltic melt depresses the plagioclase crystallization temperature (Holloway and Burnham, 1972; Sisson and Grove, 1993b) and the results from PELE also demonstrated this effect. At 1 wt.%  $H_2O$ , the solidus temperature of plagioclase decreased from  $1142^\circ C$  to  $1106^\circ C$ , crystallizing at the same

temperature as olivine. With the addition of more water up to 1.5 wt.%, the crystallization temperature of plagioclase was significantly lowered by 60 °C. In Figure 39 (B) the solidus temperature of clinopyroxene can be seen to increase with each incremental step in pressure. In total, a 300 bar increase in pressure resulted in raising the solidus temperature by 6 °C relative to that of plagioclase and olivine.

Having proposed that the phase reversals represent the return to lithostatic pressure after magmatic venting, decompression tests were also modeled by PELE. Starting at 1800 bar (upper pressure limit) and a temperature at which all three phases were initially saturated, the pressure was dropped 300 bars in one step. Results from these runs were consistent with the proposed model that a return to lithostatic pressure would shift phase equilibrium back to saturation in only plagioclase and olivine. While clinopyroxene was a saturated phase at 1800 bar, when reduced to 1500 bar, clinopyroxene became undersaturated and only plagioclase and olivine remained liquidus phases. The PELE modeling shows that, theoretically, fluctuations in pressure could produce the cyclic phase layering characteristics of the cyclic zone.

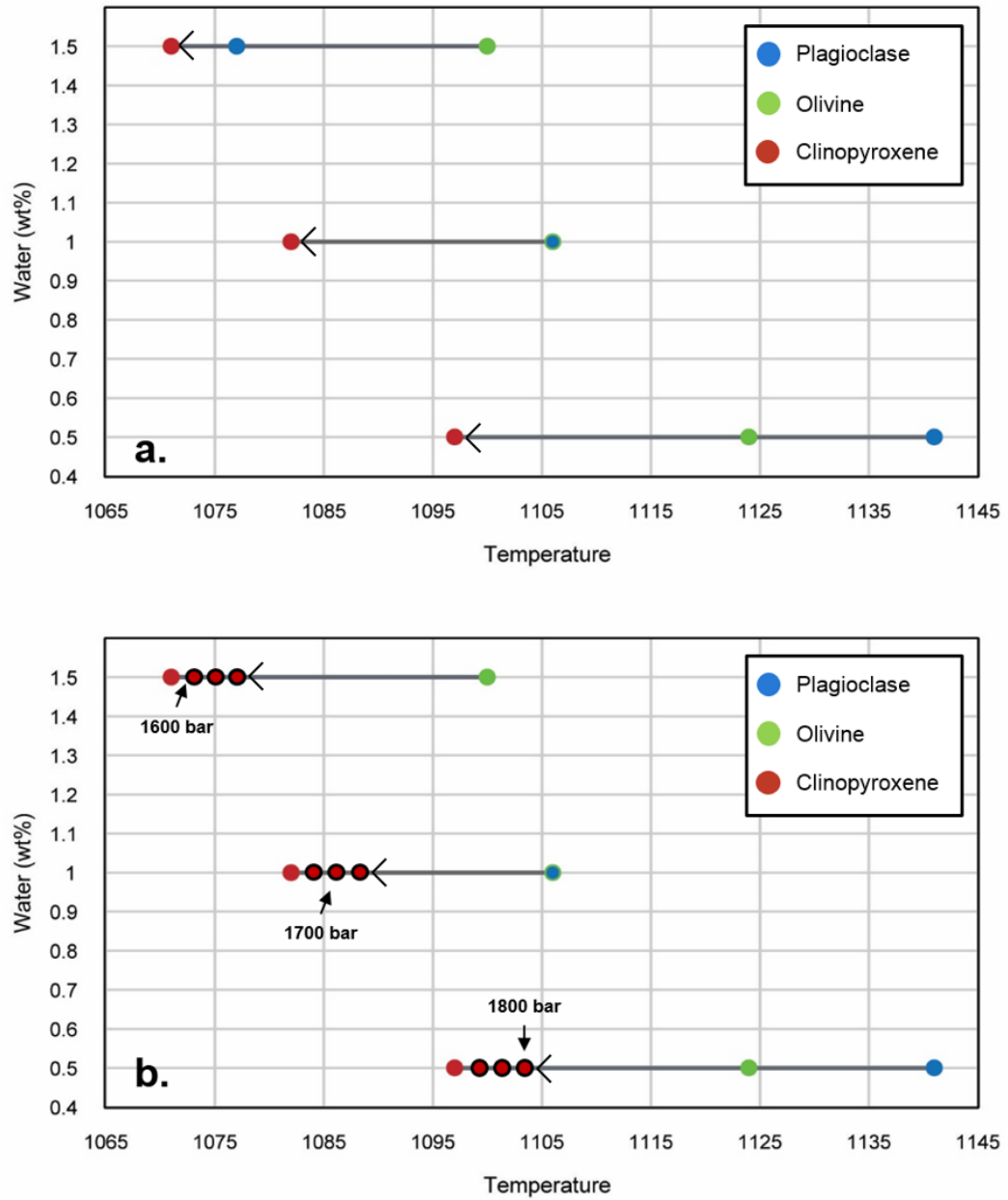


**Figure 41.** Devolatilization runs evaluating the effect of increasing pressure on clinopyroxene stability.

### **5.5.2 Occurrence of Anorthositic Xenoliths in the Cyclic Zone**

Another feature observed within the cyclic zone suggesting decompression and degassing of a volatile-saturated magma due to venting is the occurrence of DAS-like gabbroic anorthosite inclusions, which exhibit similar hydrothermal alteration as the DAS roof zone rocks, in the PcOf and PCOF cumulates found below macrocycle boundaries (Fig. 42). An eruption through the roof of the layered series could explain the occurrence of DAS-like anorthositic inclusion throughout the cyclic zone as this could indicate that the hanging wall anorthosite is breaking up as magma venting events occur. Furthermore, the occurrence of DAS-like anorthositic inclusions only within PcOf /PCOF cumulates, and not PO cumulates, is also consistent with this model. By PCOF crystallization, the DLS system presumably became saturated in a volatile phase which ultimately results in overpressures and failure of the roof zone (discussed below). The extensive hydrothermal alteration of anorthositic inclusions is consistent with a volatile-rich environment existing in the DLS roof zone, and following an eruption, anorthositic blocks detached from the chamber cupola and settled to the cumulate floor.



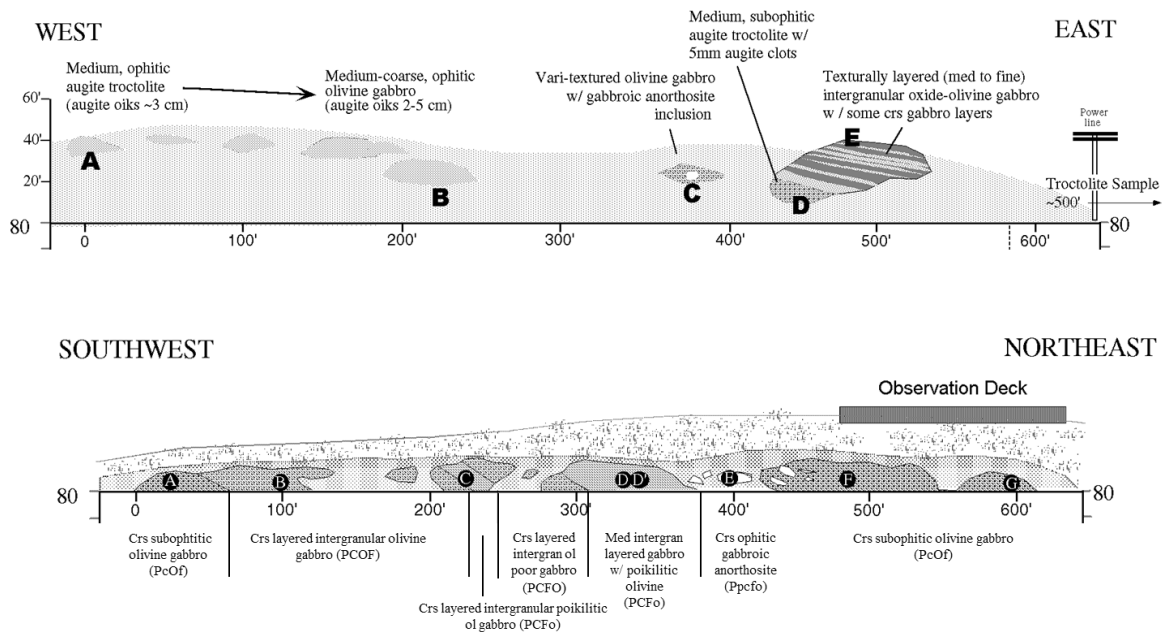


**Figure 42.** Outcrop geology corresponding to macrocycle units within the cyclic zone, illustrating the occurrence of DAS-like gabbroic anorthosite inclusions at the base of macrocycle boundaries. From Miller (2011).

### 5.5.3 Significance of Microgabbro Cumulates

A distinctive feature within the cyclic zone which is also consistent with a model of decompression quenching of a hydrous magma, rather than magma recharge, is the occurrence of microgabbro intervals found at the top of most macrocycle boundaries. The microgabbro are fine-grained, intergranular oxide olivine gabbro cumulates (PCOF) to oxide gabbro cumulates with postcumulus olivine (PCFo) and occur as centimeter- to meter-scale lenses commonly interlayered with medium-grained PCOF cumulates.

Similar fine-grained gabbro layers occurring in the Kap Edvard Holm complex and Newark Island intrusion have been interpreted to represent intraplutonic quench zones formed by chilling of a recharged primitive magma beneath a cooler resident magma

(Tegner et al., 1993; Weibe and Snyder, 1993). However, features of the microgabbros do not fit such an interpretation. For one, the microgabbros in the cyclic zone occur as lenticular cumulate layers which are commonly intercalated with medium-grained PCOF cumulates (Fig. 38 and 43). If produced by a quenched recharge magma, the microgabbros should exhibit some lateral continuity and would not be interlayered with similar cumulate phases.

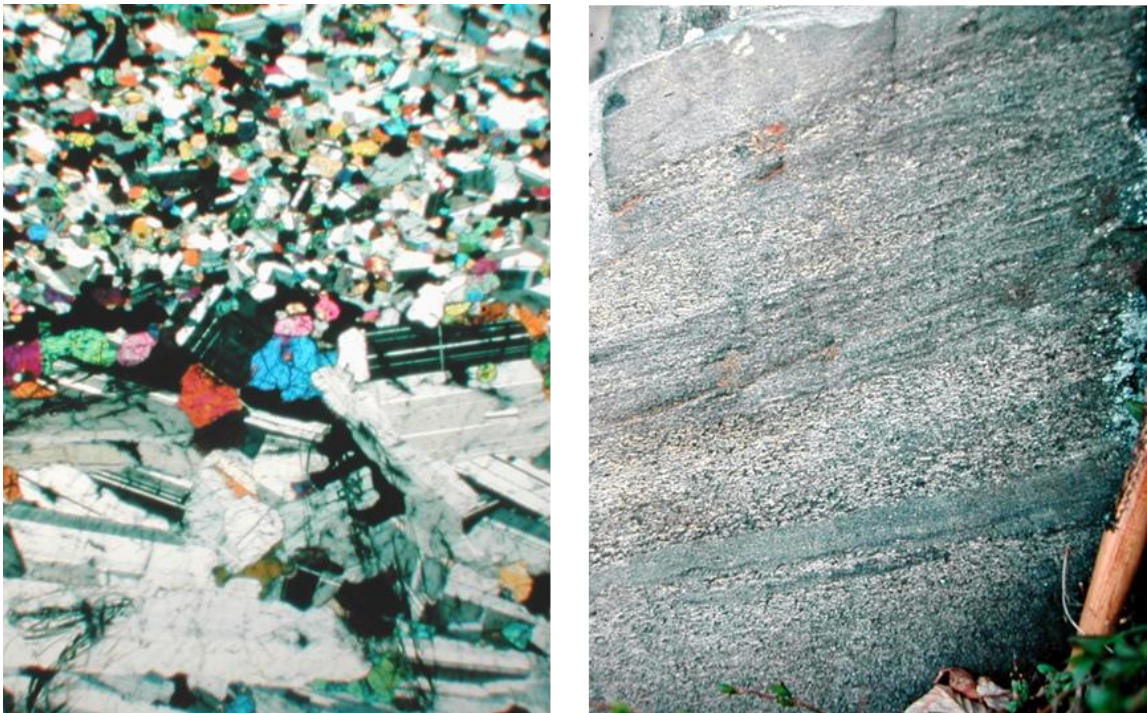


**Figure 43.** Left: Photomicrograph of microgabbro and *m*PCOF cumulates. Right: Field photograph of microgabbro interlayered with *m*PCOF cumulates.

Secondly, the mineralogy and geochemistry of the microgabbro is not consistent with a magma recharge model. If produced by quenching of a more primitive magma, the microgabbros presumably should be fine-grained plagioclase, olivine cumulates. The whole rock geochemistry of collected microgabbro samples is listed in Appendix 2. The whole rock compositions are characterized by high compatible and low incompatible element concentrations which indicates they are not quenched liquids of a primitive, recharged magma, but instead, the mineralogy, texture, and geochemistry suggest the microgabbros are fine-grained adcumulates. Instead, the DLS microgabbros are better interpreted as being the cumulate equivalents of the DLS chill formed during a decompressional quenching event. That the DLS chill and DLS microgabbro are in equilibrium, forming by the same processes, will be discussed in more detail to follow.

In Figure 22, thirteen microgabbro samples were plotted on a REE spider diagram in order to evaluate the proposed geochemical link with the chill (shown in red). As would be expected when comparing cumulates to non-cumulates, trace element abundances of the microgabbro cumulates are approximately a log unit lower in trace element abundances when compared to those of the chill. The microgabbros also exhibit a relatively flat concentration in REE abundances compared to the chill which is likely related to the different distribution coefficients of LREE and HREE for the principal cumulus phases (Pl, Cpx, and Ol; see Fig. 19). While the HREE slope of the microgabbros shows a similar trend compared to the chill, the LREE is dissimilar. The flatter trend in LREE relative to that of the chill may be explained by the occurrence of olivine and clinopyroxene, which prefer the HREE over the LREE. Similarly, the positive Eu anomaly displayed by the microgabbro cumulates relative the negative anomaly

observed in the chill, is presumably due to the compatibility of Eu<sup>2+</sup> in cumulus plagioclase.

At first glance, the chill and microgabbro appear to be unrelated based on differences in trace element concentrations and REE trends. However, because the microgabbros are cumulates, most trace elements are incompatible with cumulus mineral phases, and their whole rock concentrations will largely be a function of the amount and composition of intercumulus melt incorporated into a rock. Considering this, is it possible for the DLS chill to produce cumulate compositions such as those found in the microgabbro? Bedard (1994) developed a mass balance model for calculating the incompatible trace element composition of a melt in equilibrium with a cumulate rock. A modified version of this mass balance model was used to evaluate whether the chill could produce the microgabbro cumulates. Using this model, the whole rock concentration of each trace element, *i*, can be expressed as the sum of the modal proportions of the cumulate minerals times the concentration of element *i* in the mineral ( $Kd_i^{min}$ ), plus some fraction of trapped liquid (TL).

$$WR_i = Kd_i^{Ol} \cdot \%Ol + Kd_i^{Pl} \cdot \%Pl + Kd_i^{Cpx} \cdot \%Cpx + Kd_i^{Ox} \cdot \%Ox + TL_i \cdot \%TL$$

Kd values were determined by dividing the concentration of element *i* in the mineral by the concentration of element *i* in the liquid or

$$Kd_i^{min} = X_i^{min} / X_i^{liq}$$

The trace element abundances from the chill were used as the concentration values for element *i* in the trapped liquid (TL<sub>*i*</sub>) along with the concentration in the liquid (X<sub>*i*</sub><sup>liq</sup>) in the Kd equation. Microgabbro mode (wt.%) were determined to contain: 55% Pl + 22%

Cpx + 15% Ol + 9% Ox. These new value were then plotted on a spider diagram (Figure 44). By treating the chill as the liquid component in the calculations above, the results from these calculations indicate that the microgabbros could indeed be cumulate products of the chill and that they are almost purely adcumulates with 0-5% trapped liquid.

PELE was used one final time in order to further evaluate the proposed geochemical link between the chill and microgabbro. One of the important functions of PELE is its ability to calculate mineral chemistries of saturated phases expected to crystalize from the input bulk composition. One of the many effects associated with water, such as, depression of liquidus and solidus temperatures and plagioclase saturation depression, is its influence on mineral chemistries (Feig et al., 2006). The first set of runs were completed by varying the water content of the chill as a way to evaluate the degree of water saturation and associated mineral chemistries in equilibrium at the time of formation. The results from these runs are shown in Figure 45.

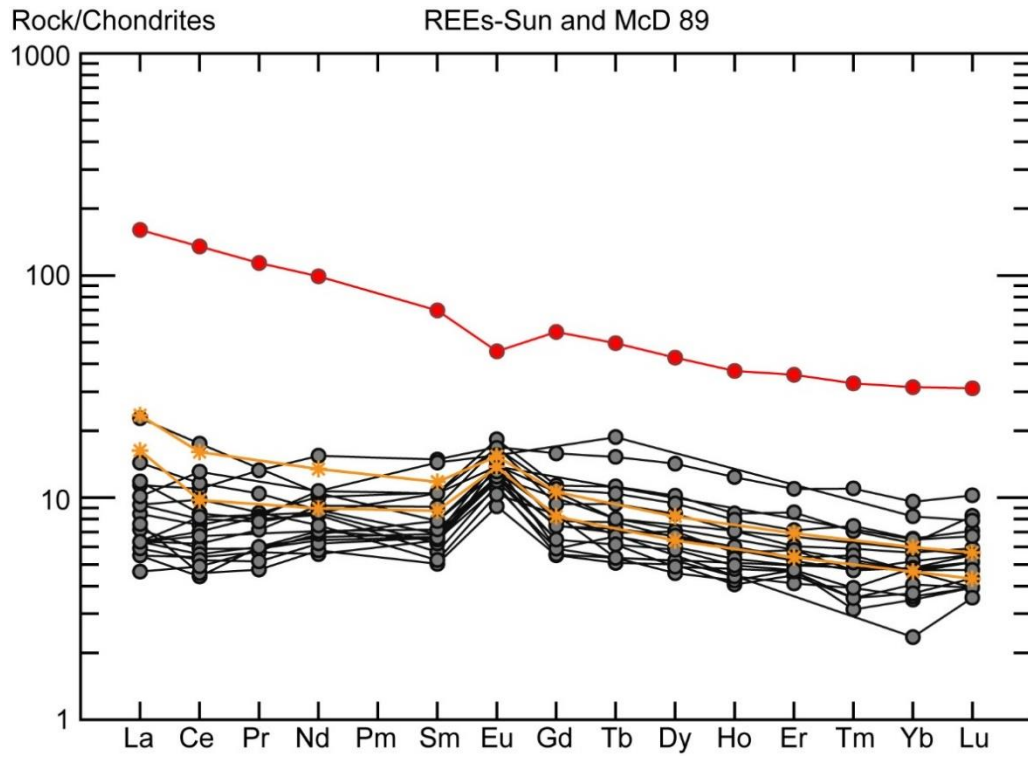


**Figure 44.** Mass balance variation diagram evaluating whether the DLS chill could produce cumulates in equilibrium with the microgabbro. Results indicate the microgabbros are purely adcumulates with 0-5% trapped liquid (orange lines).

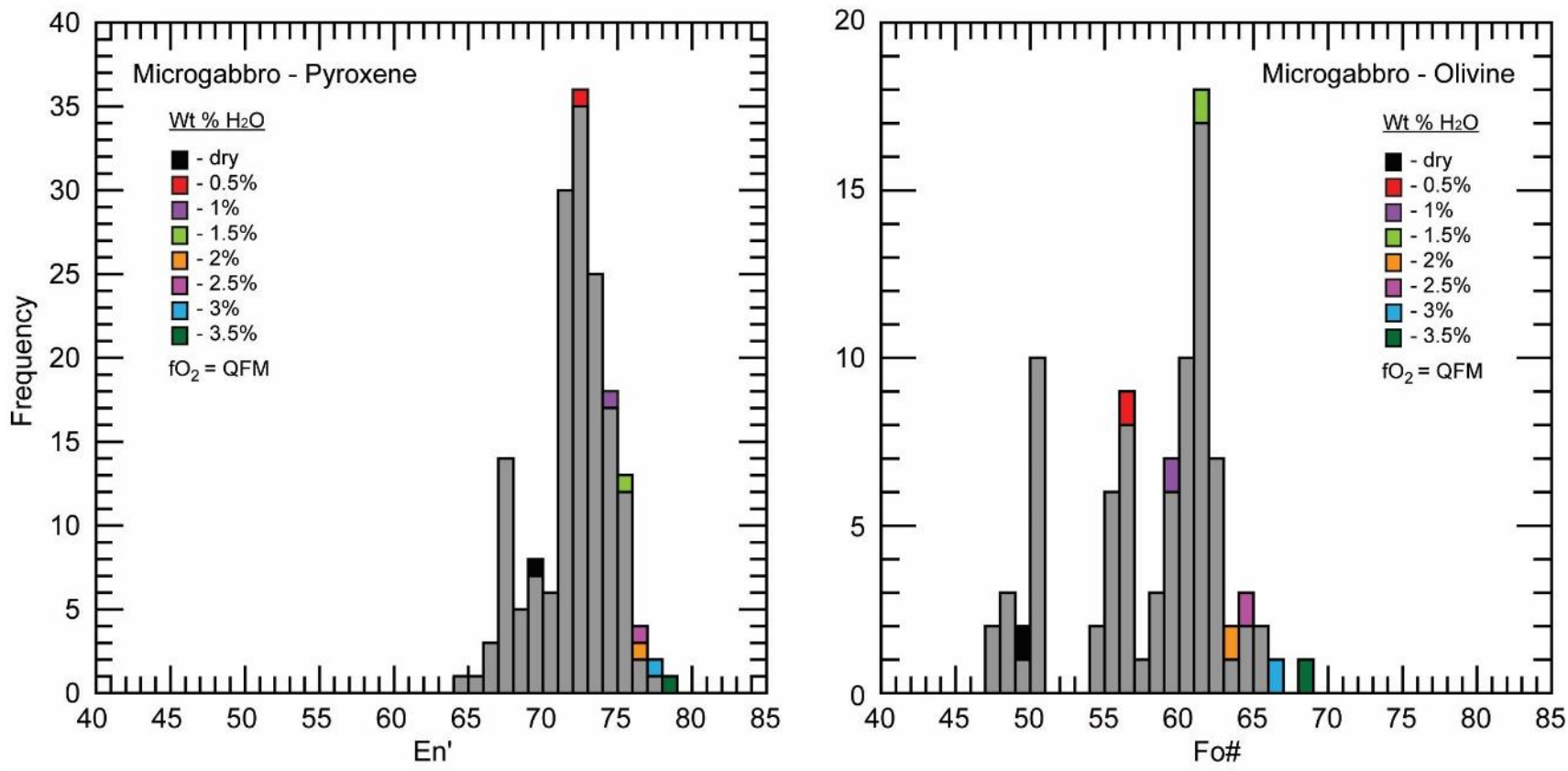


**Figure 45.** Mineral chemistries for augite and olivine determined by PELE at 1500 bar lithostatic pressure and QFM conditions. Grey bins are pyroxene and olivine values determined from SEM-EDS analyses from microgabbro sample

From the first set of runs, it is apparent that presence of water has an effect on mineral compositions by making pyroxene and olivine more magnesian. This presumably occurs because of the oxidation of  $\text{Fe}^{2+}$  to  $\text{Fe}^{3+}$ . Analyzing the results from the first set of runs indicates the chill will produce minerals (pyroxene and olivine) with comparable compositions to the microgabbro at water contents between 0 – 2.5 wt.%  $\text{H}_2\text{O}$ .

The second set of runs were completed by varying not only the water content (0 – 3.5 wt.%) but also the redox conditions between QFM -2 to QFM +2. These results are graphed in Figure 47. These results were consistent with the first run in that between 0 – 2.5 wt.% water, the minerals expected to crystalize from the chill are consistent with those measured in the microgabbro. Figure 47 only shows data from 1 – 2.5 wt.%  $\text{H}_2\text{O}$  since the chill is considered to be hydrous and the DLS parent magma was proposed already contain at least 0.8 wt.%  $\text{H}_2\text{O}$ . From the second run it was also apparent that the redox conditions had a significant effect on mineral chemistries. At lower water conditions (0 – 0.8 wt.%  $\text{H}_2\text{O}$ ; not shown) the full range of redox conditions would produce comparable minerals, falling around the mode of measured pyroxene values. Starting around 1 wt.%  $\text{H}_2\text{O}$ , however, minerals produced under oxidizing conditions begin to deviate from the mode, eventually falling outside of the range. Based on the results from PELE, under reducing conditions, a magma with the composition of the chill containing up to 2.5 wt.%  $\text{H}_2\text{O}$  would crystalize minerals in equilibrium with the microgabbro.



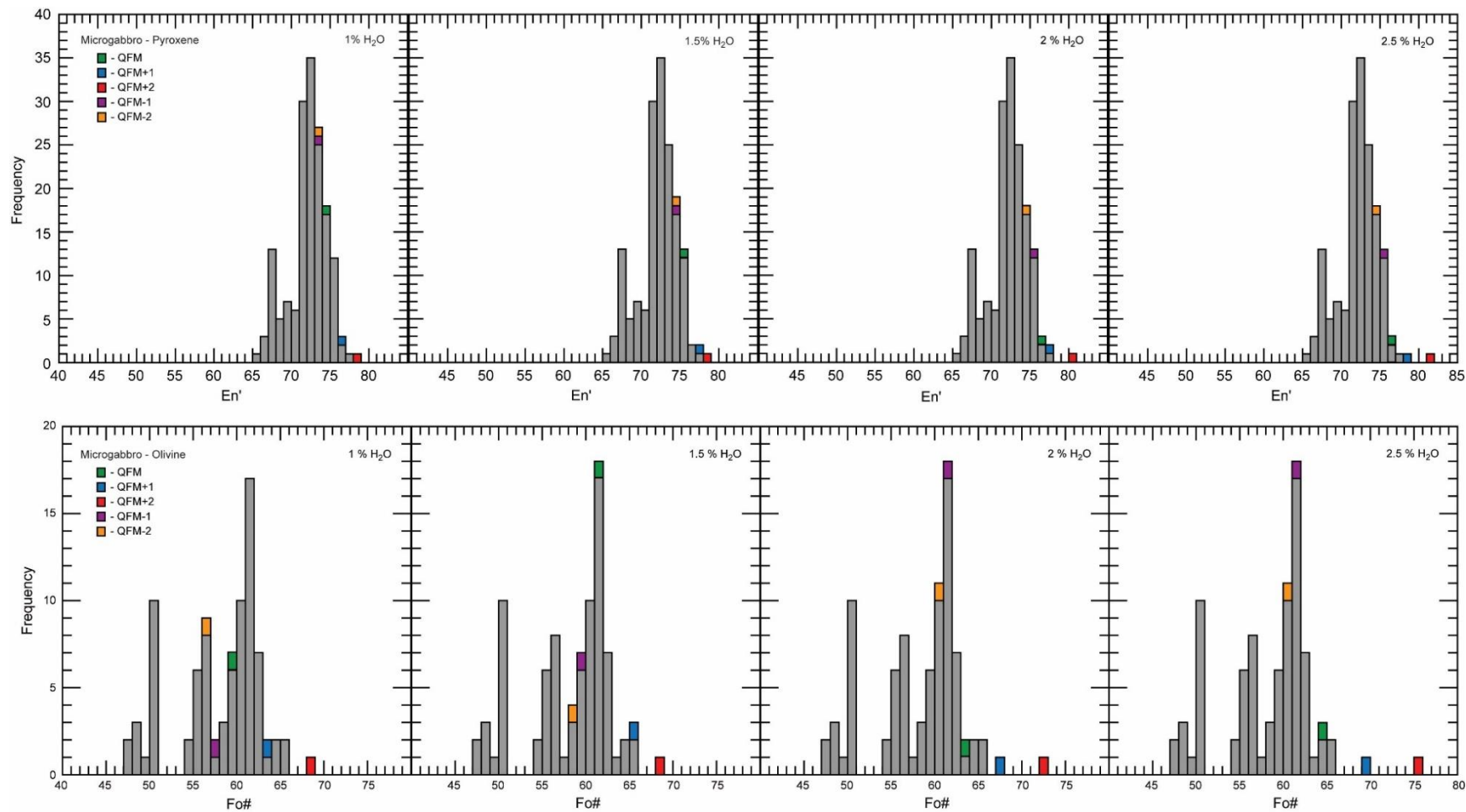


**Figure 46.** Mineral compositions for augite and olivine determined by PELE at 1500 bar lithostatic pressure,  $fO_2$  between QFM -2 to QFM +2 and water content between 1 – 2.5 wt.%  $H_2O$ . Grey bins are pyroxene and olivine values from microgabbro samples determined by SEM-EDS analysis.

## 5.5 Proposed model for the origin of the DLS Chill and Cyclic Zone

The preceding sections presented various lines of evidence supporting the interpretation that processes leading up to and attending magmatic venting better explain the formation of the DLS chill and cyclic zone. A model for the formation of these DLS components resulting from pressure fluctuations related to volatile degassing and magma venting is shown in the six panels of Figure 48.

Panel **A** represents the initiation of cyclic zone formation. Leading up from PO cumulates of the troctolite zone, the DLS magma was saturated in plagioclase and olivine, producing the PO cumulates at the base of macrocycle one. Through progressive crystallization (Panel **B**), volatile species ( $\text{CO}_2$  and  $\text{H}_2\text{O}$ ) concentrate in the magma and under the low lithostatic pressure of the DLS (~1.5 kb), eventually begin to exsolve as a separate gas phase. Through degassing, volatile pressure is added to lithostatic pressure to increase the total pressure of the system. As shown in the Ol-Pl-Cpx phase diagram in Panels **B** & **C**, pressure increase results in expanding the stability field of clinopyroxene relative to olivine and plagioclase. By Panel **C**, through further degassing, the increased pressure expands the liquidus field until the magma encounters the plagioclase-olivine-clinopyroxene eutectic, resulting in the formation of PCO(+F) cumulates. Continued degassing and a complementary decrease in magma density results in overpressurized conditions ultimately leading to roof zone failure, magma venting, devolatilization, and decompression of the magma chamber (Panel **D**). Magmatic venting of water-saturated magma results in rapid crystallization of the roof zone magma thus forming the DLS chill. Whereas most of this crystallization plated to the DAS roof zone, some of the semi-crystallized chill detached, descending through the magma as fine-crystal rich plumes

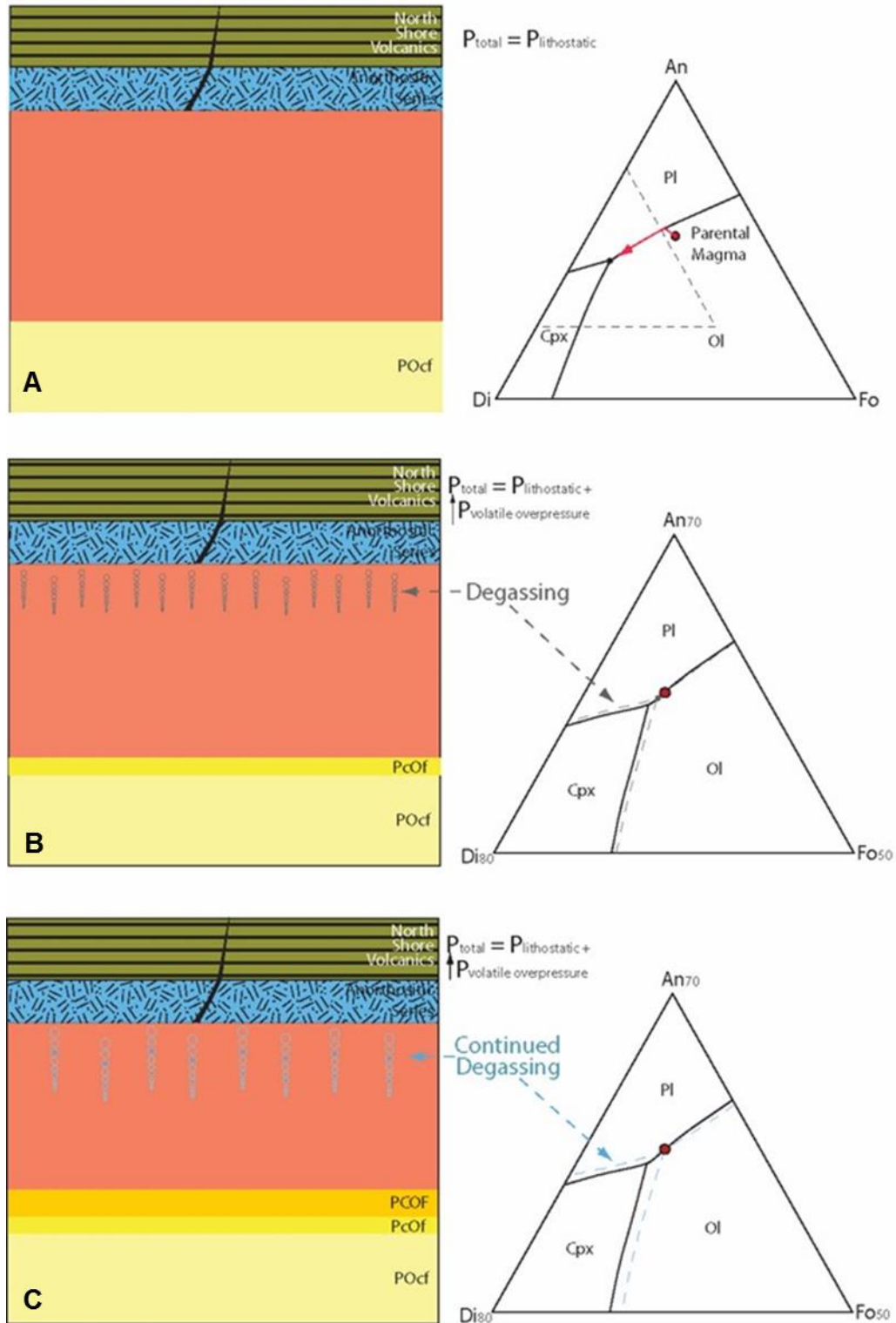


**Figure 47.** Proposed decompression quenching model illustrating macrocyclic phase layering and microgabbro formation in the Cyclic Zone and formation of the DLS chill in the Upper Contact Zone . Panels A-F described in text. After Miller and Ripley (1996)

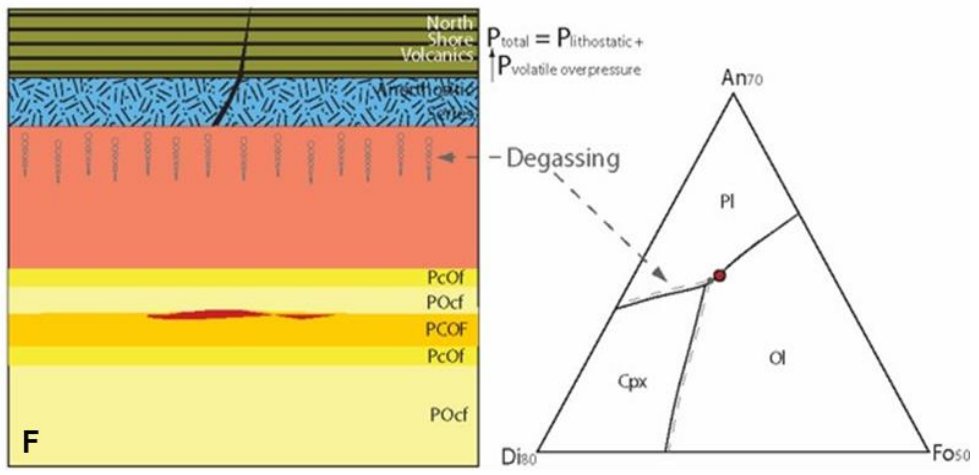
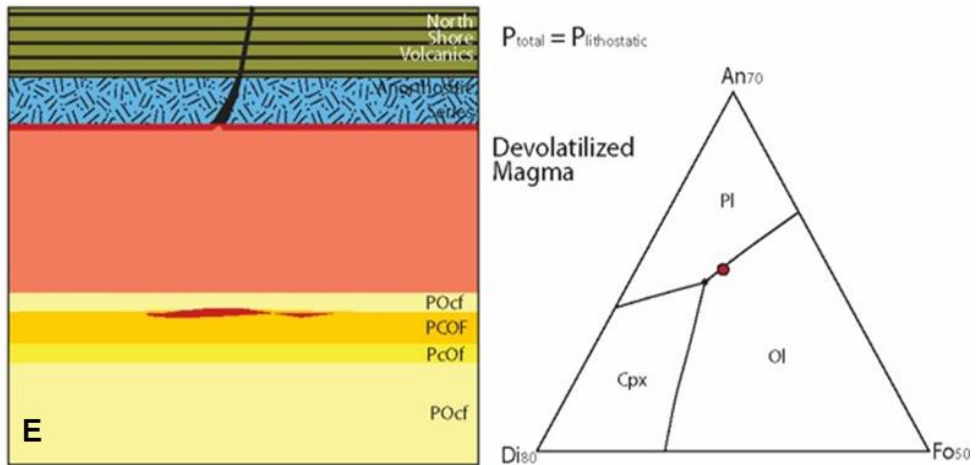
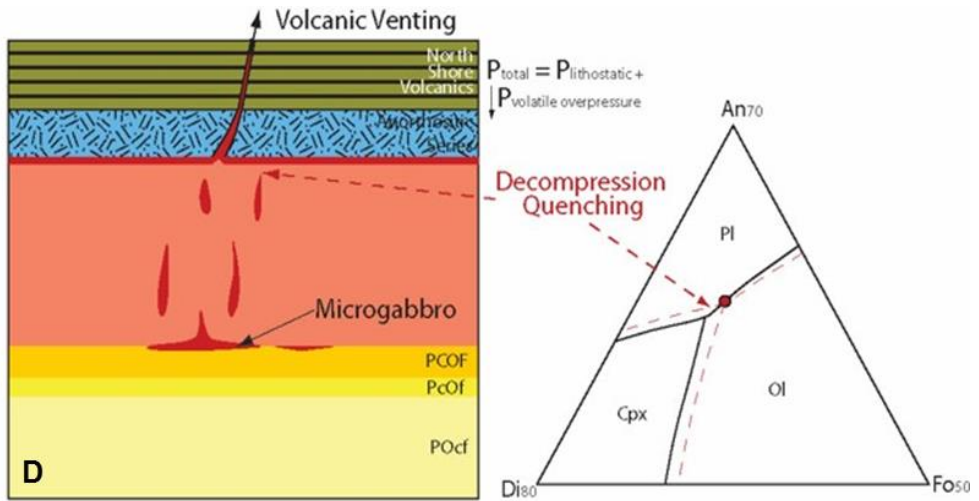
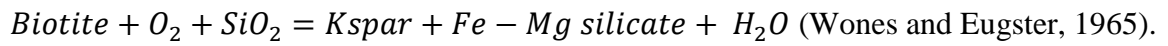


Figure 47. continued.

that settles onto the cumulate floor forming the lenticular layers of microgabbro. The observed lack of olivine in the chill and absence of biotite in the microgabbro suggest that the plume dehydrated as it descended through the hotter and drier interior of the magma chamber. A possible reaction to explain this process is:



The equilibrium tests executed by PELE suggested for the chill to be in equilibrium with the microgabbro, it could have contained up to 2.5 wt.% H<sub>2</sub>O, however, the chill would not be saturated in water until 3.65 – 4.1 wt.% H<sub>2</sub>O (determined by PELE).

Considering this dehydration reaction, it is plausible the chill formed under higher water contents, but lost some of this water as the crystal-rich plume descended through the magma which would account for the lower water contents determined by PELE.

Following volcanic venting and decompression, the chamber experienced a return to lithostatic pressure, shrinking the clinopyroxene stability field and shifting phase equilibrium back to saturation in only plagioclase and olivine (Panel **E**). This results in a phase reversal and crystallization of PO cumulates, marking the base of macrocycle 2. As the PO cumulates in the new macrocycle crystallize, volatiles exsolve, pressure increases and the process repeats (Panel **F**), thus creating the different macrocycles.

## 6. Conclusions

The principle conclusions of this study are as follows:

1. Volatile build-up and magma venting played an important role during the evolution of the DLS system.
2. The fine-grained, biotitic ilmenite ferrodiorite forming the DLS chill, which had been previously interpreted to represent a thermal quench of the DLS parental magma may, instead, represent a decompression quench of a hydrous roof zone magma formed during intermediate stages of DLS differentiation.
3. Salient features within the cyclic zone including 1) cyclic cumulate phase layering, 2) lack of correlation between phase layering and cryptic layering, 3) microgabbro intervals at the tops of most macrocycles, and 4) occurrence of DAS-like gabbroic anorthosite inclusions, represent cyclical changes in pressure, presumably formed by the build-up of volatiles creating overpressures which resulted in magma venting, in turn causing decompression and degassing.
4. The well differentiated nature of flows 58-65 along with their composition and stratigraphic position together indicate that they are the erupted products of magmatic venting from the DLS. If volcanic equivalents of the chill, this would indicate that the top of the DLS was emplaced within the volcanic edifice at a depth of ~4-5 kilometers.

## REFERENCES

- Babcock, R.C., Jr., 1959, Petrogeny of the granophyre and intermediate rock in the Duluth Gabbro of northern Cook County, Minnesota: Madison, Wis., University of Wisconsin, M.S. thesis, 47 p
- Bates, R.L., and Jackson, J.A., 1987, Glossary of Geology, 3rd edition, ed, Robert L. Bates, and Julia A. Jackson, Alexandria, VA, American Geological Institute, 788p.
- Berndt, J., Koepke, J., and Holtz, F., 2004. An Experimental Investigation of the Influence fo Water and Oxygen Fugacity on Differentiation of MORB at 200 MPa. *Journal of Petrology* **46**: 135-167.
- Boerboom, T.J., Green, J.C., and Jirsa, M.A., 2002, Bedrock geology of the French River and Lakewood quadrangles, St. Louis County, Minnesota. Minnesota Geological Survey Miscellaneous Map M-128, scale 1:24,000.
- Botcharnikov, R., Freise, M., Holtz, F., and Behrens, H., 2005. Solubility of C-O-H mixtures in natural melts: new experimental data and application range of recent models. *Annals of Geophysics* **48**: 633-646.
- Boudreau, A.E., 1999, PELE - A version of the MELTS software program for the PC platform: *Computers and Geosciences* **25**, pp. 21-203.
- Brannon, J.C. 1984. Geochemistry of successive lava flows of the Keweenawan North Shore Volcanic Group. Ph.D. thesis, Washington University, St. Louis, Mo.
- Cannon, W.F., 1992. The midcontinent rift in the Lake Superior region with emphasis on its geodynamic evolution. *Tectonophysics* **213**: 41-48.
- Cannon, W.F., 1994. Closing of the Midcontinent rift – A far-field effect of Grenvillian Compression. *Geology* **22**: 155-158.

- Cannon, W.F., and Hinze, W.J., 1992. Speculations on the origin of the North American Midcontinent rift. *Tectonophysics* **213**: 49-55.
- Carroll, M. R., and M. J. Rutherford (1985), Sulfide and sulfate saturation in hydrous silicate melts, *J. Geophys. Res.* **90**: 601–612.
- Davis, D.W., and Paces, J.B., 1990. Time resolution of geologic events on the Keweenaw Peninsula and implications for development of the Midcontinent Rift system: *Earth Planetary Science Letters* **97**: 54-64.
- Davis, D.W., and Green, J.C., 1997. Geochronology of the North American Midcontinent rift in western Lake Superior and implications for its geodynamic evolution. *Canadian Journal of Earth Sciences*, v. 34, pp. 476-488.
- Duan, Xianzhe, 2013. A general model for predicting the solubility behavior of H<sub>2</sub>O – CO<sub>2</sub> fluids in silicate melts over a wide range of pressure, temperature and compositions. *Geochimica et Cosmochimica Acta*, **125**: 582-609.
- Feig, S.T., Koepke, J., Snow, J.E., 2006. Effect of water on tholeiitic basalt phase equilibria: an experimental study under oxidizing conditions. *Contributions to Mineralogy and Petrology* **152**: 611-638.
- Ghiorso, Mark S., and Sack, Richard O., 1995 Chemical Mass Transfer in Magmatic Processes. IV. A Revised and Internally Consistent Thermodynamic Model for the Interpolation and Extrapolation of Liquid-Solid Equilibria in Magmatic Systems at Elevated Temperatures and Pressures. *Contributions to Mineralogy and Petrology*, **119**, 197-212.



- Green, J.C., 1972. North Shore Volcanic Group. *In* Geology of Minnesota – A centennial volume. *Edited by* P.K. Sims and G.B. Morey. Minnesota Geological Survey, St. Paul, pp. 294- 332.
- Green, J.C., 2002. Volcanic and sedimentary rocks of the Keweenawan Supergroup in northeastern Minnesota, in Geology and mineral potential of the Duluth Complex and related rocks of northeastern Minnesota: Minnesota Geological Survey Report of Investigations 59, pp. 94-105.
- Green, J.C., and Miller, J.D., Jr., 2008, Bedrock geology of the Duluth quadrangle, St. Louis County, Minnesota. Minnesota Geological Survey Miscellaneous Map M-182, scale 1:24,000
- Grout, F.F. 1918a. The pegmatites of the Duluth Gabbro: *Economic Geology* **13**: 185-197.
- Grout, F.F. 1918b. The lopolith an igneous form exemplified by the Duluth Gabbro: *American Journal of Science* **96**: 516-522.
- Grout, F.F. 1918c. Internal structures of igneous rocks; their significance and origin with special reference to the Duluth Gabbro: *Journal of Geology* **26**: 439-458.
- Grout, F.F. 1918d. Two-phase convection in igneous magmas: *Journal of Geology* **26**: 481-499.
- Grout, F.F. 1918e. A type of igneous differentiation: *Journal of Geology* **26**: 626-658.
- Heaman, L.M., Easton, R.M., Hart, T.R., Hollings, P., MacDonald, C.A., and Smyk, M., 2007. Further refinement to the timing of Mesoproterozoic magmatism, Lake Nipigon region, Ontario. *Canadian Journal of Earth Sciences*, v. 44, pp. 1055-1086.

- Hinze, W.J., Allen, D.J., Fox, A.J., Sunwood, D., Woelk, T., and Green, A.G., 1992. Geophysical investigations and crustal structure of the North American Midcontinent Rift system. *Tectonophysics*, v. 213, pp. 17-32.
- Hinze, W.J., Allen, D.J., Braile, L.W., and Mariano, John, 1997. The Midcontinent Rift System: A major Proterozoic continental rift. Geological Society of America. pp. 7-35.
- Hoaglund, S.A., 2010, U-Pb zircon geochronology of the Duluth Complex and related hypabyssal intrusions: Investigating the emplacement history of a large, multiphase intrusive complex related to the 1.1 Ga Midcontinent rift: Unpublished Master's Thesis University of Minnesota, Duluth. 103p.
- Hollings, P., Fralick, P., and Cousens, B., 2007a. Early history of the Midcontinent Rift inferred from geochemistry and sedimentology of the Mesoproterozoic Osler Group, northwestern Ontario. *Canadian Journal of Earth Sciences*, v. 44, pp. 389-412.
- Hollings, P., Hart, T., Richardson, A., and MacDonald, C.A., 2007b. Geochemistry of the Midproterozoic intrusive rocks of the Nipigon Embayment northwestern Ontario: evaluating the earliest phases of rift development. *Canadian Journal of Earth Sciences*, v. 44, pp. 1087-1110.
- Holloway J. and Burnham C., 1972. Melting relations of basalt with equilibrium water pressure less than total pressure. *Journal of Petrology* **13**, pp. 1-29
- Hutchinson, D.R., White, R.S., Cannon, W.F., and Shulz, K.J. 1990. Keweenawan hot spot: Geophysical evidence for a 1.1 Ga mantle plume beneath the Midcontinent Rift system. *Journal of Geophysical Research* **95**: 10,869-10,844.

- Johnson, E. R., Wallace, P.J., Cashman, K.V., and Degado Granados, H., Kent, A.J.R., 2008. Magmatic volatile contents and degassing-induced crystallization at Volcán Jorullo, Mexico: implications for melt evolution and the plumbing systems of monogenetic volcanoes. *Earth and Planetary Science Letters*, **269**: 477-486.
- Johnson, E. R., Wallace, P.J., Cashman, K.V., and Degado Granados, H., 2010. Degassing of volatiles (H<sub>2</sub>O, CO<sub>2</sub>, S, Cl) during ascent, crystallization, and eruptions at mafic monogenetic volcanoes in central Mexico. *Journal of Volcanology and Geothermal Research*, **197**: 225-238.
- Klewin, K.W., and Shirey, S.B., 1992. The igneous petrology and magmatic evolution of the Midcontinent rift system. *Tectonophysics*, **213**: pp. 33-40.
- Lightfoot, P.C., and Sutcliffe, R.H., Doherty, W., 1991. Crustal contamination identified in Keweenawan Osler Group tholeiites, Ontario: a trace element perspective. *Journal of Geology*, **99**, pp. 739-760.
- Métrich, Nicole, and Rutherford, M.J., 1998. Low pressure crystallization paths of H<sub>2</sub>O-saturated basaltic-hawaiitic melts from Mt Etna: Implications for open-system degassing of basaltic volcanoes. *Geochimica et Cosmochimica Acta*, **62**, pp. 1195-1205.
- Miller, J.D., 2011, Igneous stratigraphy of the Layered Series at Duluth – Type intrusion of the Duluth Complex. Institute on Lake Superior Geology, Proceedings Vol. 57, Part 2 – Field Trip Guidebook, p. 3-29.

- Miller, J.D., Jr., and Green, J.C., 2008a, Bedrock geology of the Duluth Heights and eastern portion of the Adolph quadrangles, St. Louis County, Minnesota. Minnesota Geological Survey Miscellaneous Map M-181, scale 1:24,000.
- Miller, J.D., Jr., and Green, J.C., 2008b, Bedrock geology of the West Duluth and eastern Portion of the Esko quadrangles, St. Louis County, Minnesota. Minnesota Geological Survey Miscellaneous Map M-183, scale 1:24,000.
- Miller, J.D., Jr., and Ripley, E.M., 1996. Layered intrusions of the Duluth Complex, Minnesota, USA, *in* Cawthorn, R.G., ed., Layered intrusions: Amsterdam, Elsevier Science, p.257-301.
- Miller, J.D., and Severson, M.J., 2002. Geology of the Duluth Complex, in Geology and mineral potential of the Duluth Complex and related rocks of northeastern Minnesota: Minnesota Geological Survey Report of Investigations **59**, pp. 106-153.
- Miller, J.D., Jr., and Weiblen, P.W. 1990. Anorthositic rocks of the Duluth Complex: Examples of rocks formed from plagioclase crystal mush. *Journal of Petrology* **31**, pp. 295-339.
- Miller, J.D., and Vervoort, J.D., 1996. The latent magmatic stage of the Midcontinent rift: a period of magmatic underplating and melting of the lower crust: Institute on Lake Superior geology, 42nd Annual Meeting, Proceedings, v. 42, Program and Abstracts, pt. 1, pp. 33-35.
- Miller, J.D., Jr., Smyk, M., Sage, R.P., and Green, J.C., 1995, Geology, petrology and metallogeny of intrusive igneous rocks of the Midcontinent Rift system. *in* Miller, J.D., Jr. (ed.), Field trip guidebook for the geology and ore deposits of the

- Midcontinent rift in the Lake Superior region. Minnesota Geological Survey Guidebook Series 20 p. 121-216.
- Miller, J.D., Jr., Green, J.C., Severson, M.J., Chandler, V.W., Hauck, S.A., Peterson, D.M., and Wahl, T.E., 2002, Geology and mineral potential of the Duluth Complex and related rocks of northeastern Minnesota: Minnesota Geological Survey Report of Investigations **58**, 207pp.
- Moore, J.G., 1970. Water Content of Basalt Erupted on the ocean floor. *Contributions to Mineralogy and Petrology* **28**: 272-279.
- Nathan, H. D., 1969, The geology of a portion of the Duluth Complex, Cook County, unpublished Ph.D. thesis, Univ. Minnesota.
- Nicholson, S. W., and Shirey, S.B., 1990. Evidence for a Precambrian mantle plum: A Sr, Nd and Pb isotopic study of the Midcontinent Rift System in the Lake Superior Region: *Journal of Geophysical Research*, **95**: p. 10,851-10,868.
- Nicholson, S.W., Shirey, S.B., Schulz, K.J., Green, J.C., 1997. Rift-wide correlation of 1.1 Ga Midcontinent rift system basalts: implications for multiple mantle sources during rift development. *Canadian Journal of Earth Sciences*, v. 34, pp. 504-529.
- Paces, J.B., and Miller, J.D., Jr. 1993. Precise U-Pb ages of Duluth Complex and related Mafic intrusions, northeastern Minnesota: Geochronological insights to physical Petrogenetic, paleomagnetic and tectono-magmatic processes associated with the 1.1 Ga Midcontinent rift system: *Journal of Geophysical Research* **98**: 13,997-14,013.

- Phinney, W.C. 1972. Northwestern part of Duluth Complex. *In* Geology of Minnesota – A Centennial volume. *Edited by* P.K. Sims and G.B. Morey. Minnesota Geological Survey, St. Paul, pp. 335-345.
- Pinkerton, Harry, Wilson, Lionel, MacDonald, Ray, 2002. The transport and eruption of magma from volcanoes: a review. *Contemporary Physics* **43**, pp. 197-210.
- Poulson, S.R. and Ohmoto, H. (1990) An evaluation of the solubility of sulfide sulfur in silicate melts from experimental data and natural samples. *Chemical Geology*, 85, 57-75.
- Ross, B.A. 1985. A petrologic study of the Bardon Peak peridotite, Duluth Complex. M.S. thesis, University of Minnesota, Minneapolis, MN.
- Ryan, M.P. 1987. Neutral buoyancy and the mechanical evolution of magmatic systems. *In* Magmatic processes: Physiochemical principles Edited by B.O. Mysen. The Geochemical Society, Special Publication **1**, pp. 259-287.
- Ryan, M.P. 1988. The mechanics and three-dimensional internal structure of active magmatic systems: Kilauea Volcano, Hawaii. *Journal of Geophysical Research* **93**, pp. 4213–4248.
- Ryan, M.P. 1993. Neutral buoyancy and the structure of mid-ocean ridge magma reservoirs. *Journal of Geophysical Research* **98**, pp. 22321–22338.
- Shirey, S.B., 1997. Re-Os isotopic compositions of Midcontinent rift system picrites: implications for plume - lithosphere interaction and enriched mantle sources. *Canadian Journal of Earth Science*, v. 34, pp. 489-503.
- Shirey, S.B., Klewin, K.W., Berg, J.H., and Carlson, R.W., 1994. Temporal changes in the sources of flood basalts: Isotopic and trace element evidence from the 1100

- Ma old Keweenaw Mamainse Point Formation, Ontario, Canada. *Geochimica Cosmochimica Acta*, v. 58, pp. 4475-4490.
- Shishkina, T.A., Botcharnikov, R.E., Holtz, F., Almeev, R.R., and Portnyagin, M.N., 2010. Solubility of H<sub>2</sub>O- and CO<sub>2</sub> – bearing fluids in tholeiitic basalts at pressures up to 500 MPa. *Chemical Geology* **277**: 115-125
- Sisson T. W. and Grove T. L., 1993a. Temperatures and H<sub>2</sub>O contents of low-MgO high-alumina basalts. *Contributions to Mineralogy and Petrology* **113**, pp. 167–184.
- Sisson T. W. and Grove T. L., 1993b. Experimental investigations of the role of H<sub>2</sub>O in calc-alkaline differentiation and subduction zone magmatism. *Contributions to Mineralogy and Petrology* **113**, pp. 143–166.
- Taylor, R.B. 1964. Geology of the Duluth Gabbro Complex near Duluth, Minnesota. *Minnesota Geological Survey Bulletin* **44**, 63 pp.
- Trehu, A., and 15 others, 1991. Imaging the Midcontinent Rift beneath Lake Superior using large Aperture seismic data: *Geophysical Research Letters* **18**: p.625-628
- Weiblen and Morey 1980. A Summary of the stratigraphy, petrology and structure of the Duluth Complex: *American Journal of Science* **280-A**: 88-133.
- Winchell, A.N., 1900. Mineralogical and petrologic study of the gabbroid rocks of Minnesota, and particularly, of the plagioclasytes: *Am. Geologist* **26**: 151-88, 197-245, 261-306, 348-388.
- Vervoort, J.D., Wirth, K., Kennedy B., Sandland, T., and Harpp, K.S., 2007. The magmatic evolution of the Midcontinent rift: New geochronologic and geochemical evidence from felsic magmatism. *Precambrian Research*, v. 157, pp. 235-268.

Appendix 1: Complete list of sampling locations.

<b>Sample</b>	<b>UTM easting</b>	<b>UTM northing</b>
SSC1A	565415	5181145
SSC1B	565424	5181127
SSC1C	565447	5181119
SSC1D	565443	5181128
SSC2A	564919	5181675
SSCB	564952	5181647
SSC3A	565697	5180055
SSC3B	565577	5180134
SSC3C	565474	5180916
SSC4	565864	5181518
SSC5	564888	5179669
SSC6	563428	5178427
SSC7	564540	5182438
SSC8	564451	5184011
SSC9A	564864	5183915
SSC9B	564950	5183890
SSC9C	964971	5183973
SSC10	563099	5179317
SSC11	563632	5179280
SSC12	563596	5179310
SSMG1	560698	5175340
SSMG2A	560251	5175365
SSMG2B	560253	5175355
SSMG2C	560245	5175385
SSMG3A	559351	5175143
SSMG3B	559361	5175144
SSMG4	559334	5174778
SSMG5	559421	5174909
SSMG6A	560653	5174007
SSMG6B	560643	5174070
SSMG7	560570	5174192
SSMG8	559993	5173207
SSMG9	559872	5173295
SSV1	579752	5190805
SSV2	579962	5190997
SSV3	580023	5191026
SSV4	580112	5191108
SSV5	580234	5191179
SSV6	582240	5192478
SSV7	582432	5192590



**Appendix 2a: SEM-EDS Analyses - Pyroxene**

<b>Sample #</b>	<b>CAT SUM</b>	<b>Si</b>	<b>Ti</b>	<b>Al</b>	<b>Fe</b>	<b>Mn</b>	<b>Mg</b>	<b>Ca</b>	<b>Na</b>	<b>En</b>	<b>Fs</b>	<b>Wo</b>	<b>EN'</b>
SSC1A-Pyx1	2.27	2.03	0.00	0.05	0.46	0.00	0.61	0.80	0.00	32.83	24.52	42.65	57.24
SSC1A-Pyx2	2.28	2.05	0.00	0.02	0.49	0.00	0.59	0.80	0.00	31.32	26.30	42.38	54.36
SSC1A-Pyx3	2.27	2.05	0.00	0.02	0.49	0.00	0.59	0.80	0.00	31.41	26.00	42.59	54.71
SSC1A-Pyx4	2.28	2.04	0.00	0.02	0.48	0.00	0.60	0.80	0.00	31.92	25.42	42.66	55.66
SSC1A-Pyx5	2.27	2.05	0.00	0.03	0.45	0.00	0.61	0.81	0.00	32.52	23.92	43.56	57.62
SSC1A-Pyx6	2.27	2.04	0.00	0.02	0.46	0.00	0.62	0.81	0.00	32.77	24.19	43.04	57.53
SSC1A-Pyx7	2.28	2.05	0.00	0.02	0.49	0.00	0.59	0.79	0.02	31.58	26.32	42.10	54.54
SSC1A-Pyx8	2.28	2.04	0.00	0.04	0.48	0.00	0.58	0.80	0.00	31.23	25.92	42.84	54.64
SSC1A-Pyx9	2.28	2.05	0.00	0.01	0.50	0.00	0.60	0.78	0.00	31.86	26.63	41.51	54.47
SSC1A-Pyx10	2.28	2.05	0.00	0.03	0.50	0.00	0.58	0.80	0.00	30.93	26.52	42.56	53.84
<b>Average</b>	<b>2.27</b>	<b>2.04</b>	<b>0.00</b>	<b>0.02</b>	<b>0.48</b>	<b>0.00</b>	<b>0.60</b>	<b>0.80</b>	<b>0.00</b>	<b>31.84</b>	<b>25.57</b>	<b>42.59</b>	<b>55.46</b>
SSC1C-Pyx1	2.24	2.13	0.00	0.01	0.57	0.00	0.67	0.48	0.00	38.91	33.23	27.86	53.93
SSC1C-Pyx2	2.26	2.05	0.00	0.02	0.43	0.00	0.62	0.82	0.00	33.26	23.11	43.63	59.01
SSC1C-Pyx2.1	2.26	2.05	0.00	0.03	0.44	0.00	0.63	0.80	0.00	33.66	23.77	42.57	58.61
SSC1C-Pyx2.2	2.27	2.03	0.00	0.04	0.46	0.00	0.61	0.80	0.00	32.53	24.47	43.01	57.07
SSC1C-Pyx3	2.26	2.05	0.00	0.03	0.43	0.00	0.63	0.79	0.00	33.90	23.33	42.78	59.24
SSC1C-Pyx4	2.27	2.01	0.02	0.06	0.44	0.00	0.61	0.81	0.00	32.89	23.49	43.62	58.34
SSC1C-Pyx4.1	2.25	2.05	0.00	0.04	0.43	0.00	0.63	0.79	0.00	34.05	23.05	42.90	59.63
SSC1C-Pyx5	2.26	2.04	0.00	0.03	0.43	0.00	0.63	0.80	0.00	34.03	22.94	43.03	59.73
SSC1C-Pyx6	2.26	2.03	0.01	0.03	0.44	0.00	0.63	0.81	0.00	33.48	23.27	43.25	59.00
SSC1C-Pyx7	2.27	1.99	0.02	0.08	0.46	0.00	0.60	0.81	0.00	32.09	24.43	43.47	56.78
SSC1C-Pyx8	2.26	2.02	0.01	0.06	0.43	0.00	0.61	0.80	0.00	33.16	23.26	43.59	58.78
SSC1C-Pyx9	2.26	2.04	0.00	0.03	0.42	0.00	0.61	0.84	0.00	32.79	22.26	44.95	59.56
SSC1C-Pyx9.1	2.27	2.01	0.02	0.07	0.46	0.00	0.60	0.78	0.00	32.70	25.08	42.22	56.60
SSC1C-Pyx9.2	2.27	2.02	0.01	0.05	0.44	0.00	0.61	0.79	0.03	33.34	23.82	42.84	58.32
SSC1C-Pyx10	2.26	2.02	0.00	0.05	0.41	0.00	0.65	0.81	0.02	34.64	22.07	43.29	61.09
<b>Average</b>	<b>2.26</b>	<b>2.04</b>	<b>0.01</b>	<b>0.04</b>	<b>0.44</b>	<b>0.00</b>	<b>0.62</b>	<b>0.78</b>	<b>0.00</b>	<b>33.70</b>	<b>24.10</b>	<b>42.20</b>	<b>58.38</b>
SSC3B-Pyx1	2.26	1.99	0.02	0.08	0.42	0.00	0.63	0.79	0.03	34.26	22.71	43.04	60.14
SSC3B-Pyx1.1	2.26	2.02	0.00	0.05	0.43	0.00	0.65	0.81	0.00	34.27	22.76	42.97	60.09
SSC3B-Pyx1.2	2.26	2.02	0.02	0.05	0.46	0.00	0.65	0.75	0.00	34.87	24.62	40.51	58.61

Appendix 2a: continued

Sample #	CAT SUM	Si	Ti	Al	Fe	Mn	Mg	Ca	Na	En	Fs	Wo	EN'
SSC3B-Pyx2	2.26	2.02	0.02	0.03	0.43	0.00	0.65	0.80	0.00	34.55	22.87	42.58	60.17
SSC3B-Pyx3	2.25	1.99	0.02	0.09	0.39	0.00	0.66	0.78	0.03	36.17	21.20	42.63	63.04
SSC3B-Pyx3.1	2.26	1.98	0.02	0.08	0.42	0.00	0.65	0.78	0.03	35.22	22.66	42.11	60.85
SSC3B-Pyx4	2.25	1.98	0.03	0.09	0.41	0.00	0.66	0.74	0.03	36.51	22.47	41.02	61.90
SSC3B-Pyx5	2.24	1.93	0.04	0.15	0.39	0.00	0.73	0.70	0.03	40.06	21.60	38.34	64.97
SSC3B-Pyx6	2.24	1.98	0.03	0.09	0.37	0.00	0.70	0.76	0.00	38.28	20.32	41.40	65.32
SSC3B-Pyx7	2.25	1.98	0.04	0.08	0.44	0.00	0.72	0.69	0.00	38.95	23.81	37.24	62.06
SSC3B-Pyx8	2.28	2.04	0.00	0.03	0.50	0.00	0.62	0.77	0.00	32.73	26.52	40.75	55.24
SSC3B-Pyx9	2.26	1.98	0.03	0.09	0.41	0.00	0.65	0.78	0.03	35.22	22.13	42.66	61.41
SSC3B-Pyx9.1	2.25	1.97	0.04	0.10	0.40	0.00	0.64	0.79	0.00	35.11	21.98	42.91	61.50
SSC3B-Pyx10	2.25	2.01	0.03	0.05	0.41	0.00	0.65	0.79	0.00	35.14	22.05	42.82	61.45
SSC3B-Pyx10.1	2.25	2.00	0.03	0.07	0.40	0.00	0.68	0.76	0.00	36.92	21.87	41.21	62.79
SSC3B-Pyx11	2.26	1.96	0.03	0.11	0.41	0.00	0.66	0.78	0.03	35.75	22.21	42.03	61.68
SSC3B-Pyx12	2.24	1.94	0.05	0.13	0.35	0.00	0.68	0.78	0.03	37.69	19.29	43.02	66.15
<b>Average</b>	<b>2.26</b>	<b>1.99</b>	<b>0.03</b>	<b>0.08</b>	<b>0.41</b>	<b>0.00</b>	<b>0.66</b>	<b>0.77</b>	<b>0.01</b>	<b>35.98</b>	<b>22.42</b>	<b>41.60</b>	<b>61.61</b>
SSC4-Pyx1	2.26	2.05	0.00	0.03	0.45	0.00	0.61	0.81	0.00	32.68	24.08	43.23	57.58
SSC4-Pyx2	2.26	2.03	0.00	0.04	0.42	0.00	0.64	0.81	0.00	34.44	22.43	43.12	60.56
SSC4-Pyx3	2.27	2.05	0.00	0.00	0.45	0.00	0.64	0.81	0.00	33.89	23.61	42.50	58.94
SSC4-Pyx3.1	2.27	2.04	0.00	0.02	0.44	0.00	0.62	0.80	0.03	33.25	23.77	42.98	58.31
SSC4-Pyx4	2.26	2.05	0.00	0.03	0.44	0.00	0.63	0.78	0.00	33.98	23.89	42.12	58.72
SSC4-Pyx4.1	2.27	2.03	0.01	0.03	0.45	0.00	0.62	0.80	0.00	33.48	23.89	42.64	58.36
SSC4-Pyx5	2.27	2.05	0.00	0.02	0.44	0.00	0.61	0.81	0.03	32.98	23.66	43.36	58.24
SSC4-Pyx6	2.26	2.04	0.00	0.03	0.43	0.00	0.64	0.81	0.00	33.98	23.11	42.91	59.52
SSC4-Pyx6.1	2.26	2.04	0.00	0.03	0.44	0.00	0.63	0.81	0.00	33.66	23.20	43.14	59.20
SSC4-Pyx7	2.27	2.05	0.00	0.00	0.48	0.00	0.62	0.80	0.00	32.60	25.12	42.28	56.48
SSC4-Pyx7.1	2.26	2.03	0.00	0.04	0.44	0.00	0.63	0.80	0.03	33.65	23.52	42.83	58.86
SSC4-Pyx8	2.26	2.01	0.02	0.06	0.44	0.00	0.61	0.80	0.00	32.95	23.62	43.43	58.24
SSC4-Pyx8.1	2.26	2.03	0.02	0.04	0.44	0.00	0.63	0.79	0.00	33.80	23.89	42.31	58.58
SSC4-Pyx9	2.26	2.05	0.00	0.03	0.45	0.00	0.62	0.80	0.00	33.28	24.14	42.58	57.96
SSC4-Pyx10	2.26	2.03	0.00	0.03	0.42	0.00	0.64	0.82	0.00	34.19	22.53	43.28	60.28
SSC4-Pyx11	2.26	2.06	0.00	0.00	0.44	0.00	0.63	0.81	0.00	33.34	23.55	43.11	58.60

Appendix 2a: continued

Sample #	CAT SUM	Si	Ti	Al	Fe	Mn	Mg	Ca	Na	En	Fs	Wo	EN'
SSC4-Pyx12	2.27	2.05	0.00	0.00	0.45	0.00	0.63	0.81	0.00	33.52	23.93	42.56	58.35
SSC4-Pyx13	2.27	2.04	0.00	0.03	0.46	0.00	0.63	0.79	0.00	33.40	24.32	42.28	57.87
SSC4-Pyx13.1	2.27	2.06	0.00	0.00	0.47	0.00	0.63	0.79	0.00	33.27	24.92	41.81	57.18
SSC4-Pyx14	2.26	2.03	0.00	0.03	0.44	0.00	0.64	0.80	0.00	33.83	23.43	42.74	59.07
SSC4-Pyx14.1	2.27	2.02	0.02	0.05	0.45	0.00	0.62	0.79	0.00	33.35	24.15	42.50	57.99
Average	2.26	2.04	0.00	0.03	0.44	0.00	0.63	0.80	0.00	33.50	23.75	42.75	58.52
SSC5-Pyx1	2.26	2.06	0.00	0.00	0.45	0.00	0.63	0.81	0.00	33.45	23.75	42.80	58.47
SSC5-Pyx2	2.26	2.05	0.00	0.03	0.42	0.00	0.62	0.82	0.00	33.30	22.73	43.96	59.43
SSC5-Pyx2.1	2.27	2.05	0.00	0.00	0.45	0.00	0.62	0.83	0.00	32.81	23.77	43.43	57.99
SSC5-Pyx3	2.26	2.06	0.00	0.00	0.44	0.00	0.63	0.81	0.00	33.38	23.27	43.35	58.92
SSC5-Pyx3.1	2.26	2.06	0.00	0.00	0.45	0.00	0.64	0.80	0.00	33.89	23.67	42.45	58.88
SSC5-Pyx3.2	2.27	2.04	0.00	0.03	0.47	0.00	0.62	0.78	0.00	33.14	25.27	41.59	56.74
SSC5-Pyx4	2.26	2.05	0.00	0.03	0.43	0.00	0.62	0.81	0.00	33.15	23.28	43.57	58.74
SSC5-Pyx5	2.26	2.06	0.00	0.00	0.45	0.00	0.64	0.80	0.00	34.10	23.59	42.31	59.10
SSC5-Pyx5.1	2.26	2.04	0.00	0.02	0.43	0.00	0.63	0.82	0.00	33.42	23.09	43.49	59.14
SSC5-Pyx5.2	2.26	2.04	0.00	0.03	0.45	0.00	0.63	0.79	0.00	33.65	24.12	42.22	58.25
SSC5-Pyx6	2.26	2.04	0.00	0.04	0.43	0.00	0.61	0.82	0.00	32.81	23.28	43.91	58.50
SSC5-Pyx6.1	2.27	2.04	0.00	0.03	0.44	0.00	0.62	0.82	0.02	33.27	23.20	43.53	58.92
SSC5-Pyx6.2	2.27	2.04	0.00	0.02	0.44	0.00	0.63	0.83	0.00	33.13	23.11	43.75	58.91
SSC5-Pyx7	2.27	2.05	0.00	0.00	0.45	0.00	0.63	0.82	0.00	33.12	23.60	43.28	58.39
SSC5-Pyx8	2.26	2.04	0.00	0.04	0.44	0.00	0.62	0.81	0.00	33.34	23.41	43.26	58.75
SSC5-Pyx9	2.26	2.03	0.01	0.04	0.44	0.00	0.61	0.80	0.00	33.09	23.66	43.25	58.31
SSC5-Pyx9.1	2.27	2.00	0.02	0.08	0.44	0.00	0.59	0.81	0.00	31.99	23.93	44.08	57.21
SSC5-Pyx10	2.26	2.04	0.00	0.03	0.44	0.00	0.62	0.82	0.00	33.10	23.19	43.71	58.81
SSC5-Pyx10.1	2.27	2.04	0.00	0.03	0.46	0.00	0.62	0.80	0.00	33.11	24.20	42.69	57.77
SSC5-Pyx11	2.26	2.05	0.00	0.02	0.44	0.00	0.63	0.80	0.00	33.62	23.41	42.98	58.95
SSC5-Pyx11.1	2.27	2.05	0.00	0.00	0.46	0.00	0.64	0.80	0.00	33.65	24.04	42.31	58.33
SSC5-Pyx11.2	2.27	2.00	0.02	0.06	0.45	0.00	0.61	0.80	0.03	32.72	24.40	42.88	57.28
SSC5-Pyx12	2.26	2.05	0.00	0.03	0.45	0.00	0.62	0.78	0.00	33.50	24.46	42.03	57.80
SSC5-Pyx12.1	2.27	2.05	0.00	0.00	0.46	0.00	0.64	0.80	0.00	33.73	23.99	42.28	58.44
Average	2.26	2.04	0.00	0.02	0.44	0.00	0.62	0.81	0.00	33.27	23.68	43.05	58.42

Appendix 2a: continued

Sample #	CAT SUM	Si	Ti	Al	Fe	Mn	Mg	Ca	Na	En	Fs	Wo	EN'
SSC5-Opx1	2.34	2.06	0.00	0.00	1.02	0.02	0.82	0.04	0.00	43.11	54.68	2.22	44.58
SSC10A-Pyx1	2.26	2.02	0.02	0.04	0.42	0.00	0.65	0.79	0.00	34.87	22.79	42.34	60.48
SSC10A-Pyx2	2.25	1.98	0.03	0.09	0.38	0.00	0.66	0.81	0.00	35.77	20.53	43.71	63.53
SSC10A-Pyx3	2.24	1.97	0.03	0.12	0.35	0.00	0.67	0.80	0.00	36.63	19.34	44.03	65.45
SSC10A-Pyx4	2.25	2.00	0.02	0.07	0.38	0.00	0.66	0.81	0.00	35.41	20.73	43.85	63.07
SSC10A-Pyx5	2.24	1.96	0.03	0.13	0.33	0.00	0.70	0.80	0.03	38.03	18.16	43.82	67.69
SSC10A-Pyx6	2.25	1.98	0.02	0.11	0.40	0.00	0.64	0.78	0.03	35.33	21.81	42.86	61.82
SSC10A-Pyx7	2.27	1.99	0.03	0.08	0.44	0.00	0.61	0.80	0.00	32.78	23.88	43.34	57.85
SSC10A-Pyx8	2.26	1.99	0.02	0.07	0.43	0.00	0.64	0.79	0.00	34.21	23.04	42.75	59.75
SSC10A-Pyx8.1	2.26	2.00	0.02	0.06	0.42	0.00	0.65	0.80	0.00	34.78	22.28	42.94	60.95
SSC10A-Pyx9	2.26	2.00	0.02	0.06	0.42	0.00	0.65	0.79	0.00	34.95	22.40	42.64	60.94
SSC10A-Pyx10	2.27	2.01	0.01	0.05	0.44	0.00	0.63	0.81	0.00	33.70	23.43	42.87	58.99
SSC10A-Pyx11	2.25	2.06	0.00	0.00	0.39	0.00	0.69	0.81	0.00	36.44	20.90	42.66	63.56
SSC10A-Pyx11.1	2.25	1.98	0.03	0.09	0.38	0.00	0.66	0.80	0.00	36.00	20.37	43.63	63.86
SSC10A-Pyx12	2.27	2.06	0.00	0.00	0.47	0.00	0.61	0.79	0.00	32.55	25.03	42.42	56.53
Average	2.26	2.00	0.02	0.07	0.40	0.00	0.65	0.80	0.00	35.10	21.76	43.13	61.75
SSC10B-Pyx1	2.27	2.03	0.00	0.04	0.46	0.00	0.62	0.81	0.00	32.75	24.33	42.92	57.37
SSC10B-Pyx2	2.27	2.03	0.00	0.04	0.47	0.00	0.61	0.80	0.00	32.34	24.91	42.75	56.49
SSC10B-Pyx2.1	2.27	2.05	0.00	0.04	0.49	0.00	0.56	0.79	0.00	30.48	26.66	42.86	53.34
SSC10B-Pyx2.2	2.28	2.05	0.00	0.02	0.52	0.00	0.57	0.79	0.00	30.35	27.71	41.94	52.27
SSC10B-Pyx3	2.28	2.03	0.00	0.04	0.50	0.00	0.58	0.81	0.00	30.70	26.41	42.89	53.75
SSC10B-Pyx4	2.27	2.03	0.00	0.04	0.47	0.00	0.62	0.80	0.00	32.74	24.90	42.35	56.80
SSC10B-Pyx5	2.28	2.03	0.00	0.04	0.50	0.00	0.59	0.79	0.00	31.36	26.43	42.21	54.26
SSC10B-Pyx6	2.27	2.03	0.00	0.04	0.47	0.00	0.60	0.79	0.00	32.30	25.40	42.30	55.98
SSC10B-Pyx7	2.28	2.01	0.02	0.05	0.49	0.00	0.59	0.79	0.00	31.64	26.01	42.36	54.88
SSC10B-Pyx8	2.27	2.03	0.01	0.03	0.47	0.00	0.62	0.76	0.00	33.37	25.51	41.12	56.67
SSC10B-Pyx9	2.28	2.01	0.02	0.06	0.49	0.00	0.58	0.79	0.00	31.04	26.55	42.41	53.89
SSC10B-Pyx10	2.27	2.02	0.01	0.04	0.47	0.00	0.60	0.79	0.00	32.32	25.42	42.26	55.98
SSC10B-Pyx10.1	2.27	2.02	0.01	0.03	0.47	0.00	0.62	0.79	0.00	32.98	25.12	41.90	56.77
SSC10B-Pyx11	2.28	2.03	0.00	0.04	0.48	0.00	0.60	0.80	0.00	31.93	25.64	42.43	55.47

Appendix 2a: continued

Sample #	CAT SUM	Si	Ti	Al	Fe	Mn	Mg	Ca	Na	En	Fs	Wo	EN'
SSC10B-Pyx12	2.29	2.03	0.00	0.03	0.52	0.00	0.58	0.79	0.00	30.55	27.40	42.05	52.72
Average	2.28	2.03	0.01	0.04	0.48	0.00	0.60	0.79	0.00	31.79	25.89	42.32	55.11
SSC10C-Pyx1	2.28	2.03	0.01	0.05	0.51	0.00	0.57	0.76	0.00	30.97	27.85	41.18	52.65
SSC10C-Pyx2	2.29	2.01	0.02	0.05	0.51	0.00	0.58	0.79	0.00	30.83	27.29	41.88	53.05
SSC10C-Pyx2.1	2.29	2.03	0.00	0.04	0.52	0.00	0.57	0.79	0.00	30.48	27.48	42.04	52.59
SSC10C-Pyx3	2.29	2.03	0.00	0.05	0.52	0.00	0.56	0.79	0.00	29.72	27.81	42.47	51.66
SSC10C-Pyx4	2.28	2.02	0.02	0.04	0.50	0.00	0.58	0.79	0.00	31.00	26.90	42.09	53.54
SSC10C-Pyx5	2.29	2.00	0.02	0.06	0.51	0.00	0.58	0.79	0.00	30.88	27.12	41.99	53.24
SSC10C-Pyx5.1	2.28	2.02	0.02	0.06	0.50	0.00	0.55	0.80	0.00	29.56	27.35	43.09	51.94
SSC10C-Pyx6	2.28	2.02	0.01	0.04	0.49	0.00	0.61	0.77	0.00	32.41	26.30	41.29	55.20
SSC10C-Pyx7	2.29	2.01	0.02	0.05	0.52	0.00	0.56	0.78	0.00	29.98	27.85	42.17	51.85
SSC10C-Pyx8	2.28	2.02	0.02	0.04	0.50	0.00	0.58	0.79	0.00	30.90	26.80	42.30	53.56
SSC10C-Pyx9	2.29	2.01	0.02	0.05	0.52	0.00	0.56	0.78	0.04	30.03	28.00	41.97	51.75
SSC10C-Pyx10	2.29	2.01	0.02	0.05	0.52	0.00	0.55	0.80	0.00	29.69	27.71	42.60	51.73
SSC10C-Pyx10.1	2.28	2.04	0.00	0.04	0.51	0.00	0.56	0.80	0.00	30.10	27.40	42.50	52.35
SSC10C-Pyx11	2.28	2.02	0.02	0.05	0.51	0.00	0.55	0.78	0.00	30.02	27.78	42.20	51.93
SSC10C-Pyx11.1	2.28	2.06	0.00	0.00	0.51	0.00	0.55	0.82	0.00	29.07	26.98	43.95	51.86
SSC10C-Pyx12	2.29	2.01	0.02	0.05	0.51	0.00	0.57	0.79	0.00	30.53	27.05	42.42	53.02
Average	2.29	2.02	0.01	0.04	0.51	0.00	0.57	0.79	0.00	30.39	27.35	42.26	52.62
SSC10C-Opx1	2.37	2.06	0.00	0.00	1.11	0.02	0.72	0.05	0.00	37.89	59.53	2.57	39.29
SSC11-Pyx1	2.26	2.00	0.02	0.08	0.41	0.00	0.61	0.82	0.00	33.13	22.42	44.46	59.64
SSC11-Pyx2	2.25	2.02	0.01	0.06	0.44	0.00	0.66	0.75	0.00	35.55	23.66	40.80	60.04
SSC11-Pyx3	2.26	2.02	0.01	0.04	0.43	0.00	0.63	0.79	0.00	34.07	23.30	42.64	59.39
SSC11-Pyx4	2.26	2.02	0.01	0.05	0.44	0.00	0.64	0.78	0.00	34.28	23.82	41.91	59.00
SSC11-Pyx5	2.26	2.00	0.02	0.07	0.43	0.00	0.61	0.80	0.00	33.29	23.33	43.38	58.80
SSC11-Pyx6	2.26	2.03	0.00	0.04	0.43	0.00	0.64	0.81	0.00	33.78	22.89	43.32	59.61
SSC11-Pyx7	2.26	2.03	0.00	0.05	0.43	0.00	0.63	0.80	0.00	33.98	23.15	42.87	59.48
SSC11-Pyx8	2.26	2.02	0.02	0.04	0.43	0.00	0.63	0.80	0.00	33.69	23.17	43.14	59.25
SSC11-Pyx9	2.26	2.01	0.01	0.05	0.40	0.00	0.66	0.80	0.03	35.60	21.65	42.76	62.19
SSC11-Pyx9.1	2.26	2.03	0.00	0.03	0.41	0.00	0.64	0.82	0.02	34.25	21.91	43.84	60.98

Appendix 2a: continued

Sample #	CAT SUM	Si	Ti	Al	Fe	Mn	Mg	Ca	Na	En	Fs	Wo	EN'
SSC11-Pyx10	2.26	2.03	0.00	0.04	0.44	0.00	0.63	0.81	0.00	33.57	23.19	43.24	59.14
SSC11-Pyx10.1	2.26	2.04	0.00	0.04	0.43	0.00	0.64	0.81	0.00	33.89	22.81	43.29	59.77
SSC11-Pyx11	2.26	2.04	0.02	0.04	0.45	0.00	0.63	0.75	0.00	34.56	24.38	41.05	58.64
SSC11-Pyx12	2.27	1.99	0.02	0.08	0.44	0.00	0.62	0.81	0.00	33.14	23.45	43.41	58.56
SSC11-Pyx12.1	2.26	2.06	0.00	0.00	0.43	0.00	0.65	0.80	0.00	34.63	22.70	42.67	60.40
<b>Average</b>	<b>2.26</b>	<b>2.02</b>	<b>0.01</b>	<b>0.05</b>	<b>0.43</b>	<b>0.00</b>	<b>0.63</b>	<b>0.80</b>	<b>0.00</b>	<b>34.09</b>	<b>23.06</b>	<b>42.85</b>	<b>59.66</b>
SSC11-Opx1	2.32	2.06	0.00	0.00	0.96	0.02	0.88	0.04	0.00	46.31	51.52	2.17	47.95
SSC11-Opx2	2.32	2.06	0.00	0.00	0.97	0.02	0.86	0.05	0.00	45.41	52.02	2.57	47.16
SSC11-Opx3	2.33	2.05	0.00	0.00	0.99	0.02	0.87	0.04	0.00	45.13	52.53	2.34	46.71
SSC11-Opx4	2.32	2.06	0.00	0.00	0.96	0.02	0.88	0.04	0.00	46.08	51.73	2.20	47.71
SSC11-Opx5	2.33	2.05	0.00	0.00	1.00	0.02	0.86	0.04	0.00	44.91	53.11	1.97	46.40
SSC11-Opx6	2.33	2.06	0.00	0.00	0.99	0.02	0.84	0.06	0.00	44.22	52.83	2.95	46.05
SSC11-Opx7	2.34	2.06	0.00	0.00	1.02	0.03	0.81	0.04	0.00	42.59	55.15	2.26	44.27
SSC11-Opx8	2.34	2.05	0.00	0.00	1.00	0.02	0.85	0.05	0.00	44.10	53.07	2.82	45.95
<b>Average</b>	<b>2.33</b>	<b>2.06</b>	<b>0.00</b>	<b>0.00</b>	<b>0.98</b>	<b>0.02</b>	<b>0.86</b>	<b>0.05</b>	<b>0.00</b>	<b>44.84</b>	<b>52.74</b>	<b>2.41</b>	<b>46.53</b>
SSC12-Pyx1	2.26	2.04	0.00	0.04	0.43	0.00	0.62	0.82	0.00	33.31	23.07	43.62	59.08
SSC12-Pyx2	2.26	2.03	0.00	0.04	0.44	0.00	0.66	0.79	0.00	34.84	23.41	41.75	59.81
SSC12-Pyx3	2.26	2.03	0.00	0.03	0.44	0.00	0.63	0.81	0.00	33.60	23.21	43.19	59.15
SSC12-Pyx4	2.26	2.06	0.00	0.00	0.43	0.00	0.64	0.82	0.00	34.05	22.74	43.22	59.96
SSC12-Pyx5	2.26	2.04	0.00	0.03	0.44	0.00	0.64	0.80	0.00	34.22	23.20	42.58	59.59
SSC12-Pyx5.1	2.31	2.06	0.00	0.00	0.98	0.00	0.86	0.05	0.00	45.50	51.64	2.86	46.84
SSC12-Pyx6	2.27	2.02	0.01	0.04	0.48	0.00	0.66	0.73	0.00	35.34	25.74	38.92	57.85
SSC12-Pyx6.1	2.26	2.03	0.00	0.03	0.45	0.00	0.65	0.80	0.00	34.17	23.56	42.26	59.19
SSC12-Pyx7	2.26	2.04	0.00	0.04	0.43	0.00	0.62	0.81	0.00	33.37	22.89	43.74	59.32
SSC12-Pyx8	2.26	2.03	0.00	0.04	0.43	0.00	0.64	0.81	0.00	34.05	22.64	43.31	60.06
SSC12-Pyx9	2.26	2.03	0.00	0.03	0.45	0.00	0.65	0.79	0.00	34.21	23.76	42.03	59.02
SSC12-Pyx9.1	2.26	2.03	0.00	0.02	0.43	0.00	0.65	0.81	0.00	34.43	22.84	42.73	60.12
SSC12-Pyx10	2.32	2.05	0.00	0.00	0.98	0.00	0.87	0.05	0.00	45.69	51.60	2.71	46.96
SSC12-Pyx10.1	2.26	2.01	0.02	0.06	0.44	0.00	0.64	0.79	0.00	34.16	23.45	42.39	59.30
SSC12-Pyx11	2.27	2.00	0.02	0.07	0.45	0.00	0.62	0.79	0.00	33.38	24.02	42.60	58.15
<b>Average</b>	<b>2.27</b>	<b>2.03</b>	<b>0.00</b>	<b>0.03</b>	<b>0.51</b>	<b>0.00</b>	<b>0.67</b>	<b>0.70</b>	<b>0.00</b>	<b>35.62</b>	<b>27.18</b>	<b>37.19</b>	<b>57.63</b>

Appendix 2a. continued

Sample #	CAT SUM	Si	Ti	Al	Fe	Mn	Mg	Ca	Na	En	Fs	Wo	EN'
SSC12-Opx1	2.32	2.05	0.00	0.00	0.97	0.02	0.87	0.05	0.00	45.66	51.48	2.86	47.51
SSC12-Opx2	2.34	2.05	0.00	0.00	1.01	0.02	0.85	0.04	0.00	44.42	53.67	1.91	45.86
SSC12-Opx3	2.33	2.06	0.00	0.00	0.98	0.02	0.84	0.06	0.00	44.28	52.82	2.90	46.16
SSC12-Opx4	2.33	2.06	0.00	0.00	0.99	0.02	0.86	0.05	0.00	44.90	52.70	2.40	46.45
SSC12-Opx5	2.32	2.06	0.00	0.00	0.97	0.02	0.88	0.05	0.00	45.93	51.64	2.43	47.61
SSC12-Opx6	2.33	2.04	0.01	0.00	0.98	0.02	0.87	0.05	0.00	45.27	52.34	2.39	46.80
<b>Average</b>	<b>2.33</b>	<b>2.05</b>	<b>0.00</b>	<b>0.00</b>	<b>0.98</b>	<b>0.02</b>	<b>0.86</b>	<b>0.05</b>	<b>0.00</b>	<b>45.08</b>	<b>52.44</b>	<b>2.48</b>	<b>46.73</b>
SSMG1-Pyx1	2.23	1.97	0.03	0.09	0.30	0.00	0.76	0.79	0.02	41.05	16.09	42.86	71.84
SSMG1-Pyx2	2.22	1.99	0.00	0.09	0.30	0.00	0.77	0.80	0.03	41.29	15.82	42.88	72.30
SSMG1-Pyx2.1	2.23	1.98	0.03	0.08	0.31	0.00	0.77	0.78	0.02	41.26	16.77	41.97	71.10
SSMG1-Pyx2.2	2.23	1.98	0.03	0.08	0.31	0.00	0.77	0.76	0.02	41.80	16.98	41.22	71.11
SSMG1-Pyx3	2.22	1.98	0.03	0.09	0.30	0.00	0.77	0.77	0.00	41.73	16.50	41.77	71.66
SSMG1-Pyx3.1	2.22	1.97	0.03	0.08	0.29	0.00	0.77	0.81	0.00	41.23	15.40	43.37	72.81
SSMG1-Pyx4	2.22	1.98	0.03	0.09	0.28	0.00	0.75	0.82	0.00	40.68	15.24	44.08	72.75
SSMG1-Pyx5	2.22	1.97	0.03	0.09	0.30	0.00	0.76	0.80	0.00	40.99	15.90	43.11	72.06
SSMG1-Pyx6	2.22	1.98	0.03	0.08	0.30	0.00	0.77	0.79	0.02	41.34	15.90	42.77	72.22
SSMG1-Pyx6.1	2.23	1.97	0.03	0.09	0.29	0.00	0.77	0.80	0.02	41.37	15.78	42.86	72.39
SSMG1-Pyx7	2.22	1.98	0.03	0.08	0.28	0.00	0.77	0.82	0.00	41.33	14.84	43.83	73.58
SSMG1-Pyx8	2.22	1.98	0.03	0.09	0.29	0.00	0.76	0.80	0.02	41.00	15.79	43.21	72.19
SSMG1-Pyx9	2.22	1.98	0.03	0.08	0.29	0.00	0.76	0.79	0.00	41.34	15.80	42.86	72.35
SSMG1-Pyx9.1	2.22	1.98	0.03	0.08	0.29	0.00	0.77	0.79	0.00	41.81	15.56	42.63	72.87
SSMG1-Pyx10	2.22	1.98	0.03	0.08	0.29	0.00	0.78	0.80	0.00	41.47	15.73	42.80	72.51
SSMG1-Pyx11	2.22	1.98	0.03	0.08	0.30	0.00	0.77	0.79	0.02	41.47	15.90	42.63	72.28
SSMG1-Pyx12	2.23	1.97	0.04	0.08	0.31	0.00	0.79	0.76	0.00	42.29	16.78	40.93	71.59
SSMG1-Pyx12.1	2.22	2.00	0.02	0.07	0.28	0.00	0.77	0.80	0.00	41.67	15.33	43.00	73.10
<b>Average</b>	<b>2.22</b>	<b>1.98</b>	<b>0.03</b>	<b>0.08</b>	<b>0.29</b>	<b>0.00</b>	<b>0.77</b>	<b>0.79</b>	<b>0.01</b>	<b>41.40</b>	<b>15.89</b>	<b>42.71</b>	<b>72.26</b>
SSMG2C-Pyx1	2.24	1.99	0.02	0.07	0.35	0.00	0.72	0.79	0.00	38.65	18.98	42.37	67.06
SSMG2C-Pyx2	2.24	1.99	0.03	0.07	0.34	0.00	0.72	0.79	0.03	38.99	18.45	42.56	67.87
SSMG2C-Pyx3	2.23	2.01	0.02	0.05	0.32	0.00	0.74	0.80	0.00	39.89	17.33	42.78	69.71
SSMG2C-Pyx3.1	2.23	2.00	0.03	0.06	0.34	0.00	0.72	0.79	0.00	38.86	18.34	42.80	67.93
SSMG2C-Pyx4	2.23	1.99	0.03	0.07	0.33	0.00	0.74	0.79	0.00	39.57	17.92	42.51	68.84

Appendix 2a. continued

Sample #	CAT SUM	Si	Ti	Al	Fe	Mn	Mg	Ca	Na	En	Fs	Wo	EN'
SSMG2C-Pyx5	2.24	1.99	0.02	0.07	0.36	0.00	0.71	0.80	0.00	38.22	19.18	42.60	66.59
SSMG2C-Pyx5.1	2.23	1.99	0.03	0.07	0.34	0.00	0.71	0.80	0.00	38.35	18.18	43.47	67.83
SSMG2C-Pyx6	2.24	1.99	0.03	0.06	0.35	0.00	0.73	0.80	0.00	38.69	18.52	42.79	67.62
SSMG2C-Pyx7	2.24	1.99	0.02	0.06	0.34	0.00	0.73	0.80	0.00	39.17	18.31	42.51	68.15
SSMG2C-Pyx8	2.24	1.98	0.03	0.07	0.35	0.00	0.72	0.80	0.00	38.63	18.53	42.84	67.59
SSMG2C-Pyx9	2.23	1.99	0.03	0.07	0.34	0.00	0.71	0.80	0.00	38.43	18.26	43.31	67.78
SSMG2C-Pyx10	2.23	2.00	0.03	0.07	0.34	0.00	0.72	0.78	0.00	39.06	18.42	42.52	67.96
SSMG2C-Pyx11	2.24	1.99	0.03	0.07	0.35	0.00	0.72	0.80	0.00	38.68	18.81	42.51	67.29
SSMG2C-Pyx12	2.24	1.99	0.03	0.07	0.35	0.00	0.70	0.81	0.00	37.74	18.72	43.54	66.84
<b>Average</b>	2.24	1.99	0.03	0.07	0.34	0.00	0.72	0.80	0.00	38.78	18.43	42.79	67.79
SSMG3B-Pyx1	2.23	1.97	0.03	0.08	0.30	0.00	0.77	0.79	0.00	41.50	16.32	42.18	71.78
SSMG3B-Pyx2	2.22	1.99	0.02	0.08	0.30	0.00	0.77	0.79	0.00	41.64	15.92	42.44	72.34
SSMG3B-Pyx3	2.24	1.98	0.03	0.07	0.40	0.00	0.82	0.66	0.00	43.56	21.45	34.99	67.01
SSMG3B-Pyx4	2.22	1.99	0.02	0.08	0.29	0.00	0.77	0.78	0.03	41.82	15.71	42.46	72.69
SSMG3B-Pyx5	2.22	1.98	0.03	0.09	0.30	0.00	0.75	0.78	0.02	41.16	16.35	42.50	71.57
SSMG3B-Pyx6	2.22	1.98	0.03	0.08	0.28	0.00	0.78	0.78	0.02	42.16	15.31	42.53	73.36
SSMG3B-Pyx6.1	2.23	1.96	0.03	0.08	0.31	0.00	0.77	0.80	0.02	41.13	16.31	42.57	71.61
SSMG3B-Pyx7	2.22	1.98	0.03	0.08	0.29	0.00	0.76	0.80	0.02	41.19	15.64	43.17	72.47
SSMG3B-Pyx8	2.22	1.98	0.03	0.08	0.29	0.00	0.76	0.80	0.00	40.99	15.61	43.40	72.42
SSMG3B-Pyx9	2.23	1.98	0.03	0.07	0.32	0.00	0.79	0.75	0.02	42.40	17.07	40.53	71.29
SSMG3B-Pyx10	2.23	1.97	0.04	0.08	0.30	0.00	0.76	0.79	0.03	40.95	16.26	42.79	71.58
SSMG3B-Pyx11	2.22	1.99	0.03	0.08	0.28	0.00	0.76	0.79	0.00	41.44	15.44	43.12	72.85
SSMG3B-Pyx12	2.23	1.98	0.02	0.08	0.32	0.00	0.79	0.76	0.02	42.20	17.20	40.60	71.04
<b>Average</b>	2.22	1.98	0.03	0.08	0.31	0.00	0.77	0.77	0.01	41.70	16.51	41.79	71.69
SSMG4-Pyx1	2.23	1.98	0.03	0.08	0.30	0.00	0.75	0.80	0.02	40.71	16.14	43.15	71.60
SSMG4-Pyx2	2.22	1.98	0.03	0.08	0.29	0.00	0.75	0.79	0.02	41.09	16.06	42.85	71.90
SSMG4-Pyx3	2.23	1.98	0.03	0.08	0.31	0.00	0.76	0.78	0.00	41.09	16.73	42.18	71.07
SSMG4-Pyx4	2.23	1.96	0.04	0.08	0.30	0.00	0.76	0.80	0.02	41.01	16.10	42.89	71.81
SSMG4-Pyx5	2.23	1.97	0.03	0.09	0.31	0.00	0.76	0.78	0.02	40.82	16.90	42.28	70.72
SSMG4-Pyx6	2.23	1.98	0.03	0.07	0.30	0.00	0.77	0.80	0.02	41.21	15.97	42.82	72.07
SSMG4-Pyx6.1	2.22	1.98	0.03	0.08	0.28	0.00	0.78	0.79	0.02	42.13	15.02	42.86	73.72



Appendix 2a. continued

Sample #	CAT SUM	Si	Ti	Al	Fe	Mn	Mg	Ca	Na	En	Fs	Wo	EN'
SSMG4-Pyx7	2.21	2.03	0.00	0.05	0.29	0.00	0.79	0.78	0.02	42.74	15.41	41.85	73.50
SSMG4-Pyx8	2.22	2.00	0.01	0.08	0.30	0.00	0.76	0.79	0.02	40.98	16.15	42.88	71.73
SSMG4-Pyx9	2.23	1.97	0.03	0.08	0.34	0.00	0.79	0.75	0.02	42.18	17.97	39.85	70.12
SSMG4-Pyx10	2.22	1.98	0.03	0.08	0.29	0.00	0.76	0.78	0.03	41.29	15.96	42.75	72.12
SSMG4-Pyx11	2.23	1.98	0.03	0.08	0.30	0.00	0.74	0.80	0.02	40.36	16.26	43.38	71.29
SSMG4-Pyx12	2.22	1.98	0.03	0.07	0.31	0.00	0.77	0.76	0.02	41.63	16.85	41.52	71.18
<b>Average</b>	<b>2.22</b>	<b>1.98</b>	<b>0.03</b>	<b>0.08</b>	<b>0.30</b>	<b>0.00</b>	<b>0.76</b>	<b>0.78</b>	<b>0.02</b>	<b>41.33</b>	<b>16.27</b>	<b>42.40</b>	<b>71.76</b>
SSMG5-Pyx1	2.22	1.98	0.03	0.08	0.29	0.00	0.75	0.79	0.03	41.12	15.62	43.26	72.47
SSMG5-Pyx2	2.22	1.99	0.03	0.09	0.28	0.00	0.75	0.79	0.03	41.33	15.22	43.45	73.08
SSMG5-Pyx3	2.22	1.98	0.03	0.09	0.29	0.00	0.75	0.80	0.02	41.04	15.55	43.41	72.52
SSMG5-Pyx4	2.22	1.98	0.03	0.09	0.29	0.00	0.79	0.76	0.00	42.56	15.99	41.45	72.69
SSMG5-Pyx5	2.22	1.97	0.04	0.08	0.29	0.00	0.77	0.78	0.02	41.79	15.83	42.37	72.53
SSMG5-Pyx5.1	2.23	1.97	0.03	0.09	0.30	0.00	0.76	0.79	0.02	41.00	16.23	42.77	71.64
SSMG5-Pyx6	2.23	1.97	0.03	0.08	0.30	0.00	0.76	0.79	0.02	40.94	16.15	42.91	71.71
SSMG5-Pyx7	2.22	1.97	0.03	0.09	0.28	0.00	0.77	0.80	0.02	41.30	15.26	43.43	73.02
SSMG5-Pyx7.1	2.21	2.01	0.00	0.07	0.27	0.00	0.81	0.79	0.02	43.33	14.41	42.26	75.04
SSMG5-Pyx8	2.22	1.98	0.03	0.09	0.28	0.00	0.76	0.81	0.03	41.11	15.00	43.89	73.26
SSMG5-Pyx9	2.23	1.98	0.03	0.08	0.29	0.00	0.77	0.80	0.02	41.12	15.65	43.23	72.43
SSMG5-Pyx10	2.22	1.98	0.03	0.09	0.29	0.00	0.76	0.79	0.02	41.15	16.02	42.83	71.98
SSMG5-Pyx11	2.23	1.97	0.03	0.08	0.30	0.00	0.78	0.80	0.00	41.43	16.13	42.45	71.98
SSMG5-Pyx12	2.21	2.02	0.00	0.05	0.27	0.00	0.82	0.79	0.02	43.49	14.43	42.07	75.08
SSMG5-Pyx12.1	2.22	1.97	0.03	0.09	0.29	0.00	0.79	0.77	0.02	42.51	15.79	41.70	72.91
<b>Average</b>	<b>2.22</b>	<b>1.98</b>	<b>0.03</b>	<b>0.08</b>	<b>0.29</b>	<b>0.00</b>	<b>0.77</b>	<b>0.79</b>	<b>0.02</b>	<b>41.68</b>	<b>15.55</b>	<b>42.77</b>	<b>72.82</b>
SSMG6B-Pyx1	2.21	1.98	0.03	0.08	0.28	0.00	0.81	0.75	0.02	43.98	15.32	40.70	74.16
SSMG6B-Pyx2	2.21	1.97	0.03	0.09	0.25	0.00	0.79	0.80	0.03	42.82	13.65	43.52	75.82
SSMG6B-Pyx2.1	2.22	1.96	0.03	0.10	0.26	0.00	0.78	0.81	0.02	41.98	14.10	43.92	74.86
SSMG6B-Pyx3	2.21	1.98	0.03	0.09	0.25	0.00	0.78	0.82	0.00	42.04	13.69	44.28	75.44
SSMG6B-Pyx4	2.21	1.97	0.04	0.09	0.26	0.00	0.78	0.81	0.00	42.35	13.79	43.87	75.44
SSMG6B-Pyx5	2.21	1.98	0.03	0.09	0.25	0.00	0.77	0.82	0.02	41.84	13.83	44.33	75.16
SSMG6B-Pyx6	2.22	1.97	0.03	0.09	0.26	0.00	0.77	0.82	0.00	41.70	14.14	44.15	74.68
SSMG6B-Pyx7	2.22	1.97	0.03	0.09	0.26	0.00	0.76	0.82	0.03	41.28	14.28	44.44	74.30

Appendix 2a. continued

Sample #	CAT SUM	Si	Ti	Al	Fe	Mn	Mg	Ca	Na	En	Fs	Wo	EN'
SSMG6B-Pyx8	2.21	1.98	0.03	0.09	0.33	0.00	0.84	0.67	0.00	45.74	18.06	36.19	71.69
SSMG6B-Pyx9	2.21	1.97	0.04	0.10	0.25	0.00	0.77	0.82	0.00	41.74	13.78	44.47	75.18
SSMG6B-Pyx9.1	2.21	2.00	0.02	0.07	0.26	0.00	0.80	0.79	0.00	42.99	14.22	42.79	75.14
SSMG6B-Pyx10	2.22	1.97	0.03	0.09	0.26	0.00	0.78	0.83	0.00	41.57	14.14	44.29	74.62
SSMG6B-Pyx11	2.22	1.98	0.03	0.09	0.31	0.00	0.80	0.75	0.00	43.21	16.44	40.35	72.44
SSMG6B-Pyx12	2.22	1.98	0.03	0.09	0.28	0.00	0.79	0.78	0.00	42.72	15.24	42.03	73.70
<b>Average</b>	<b>2.22</b>	<b>1.98</b>	<b>0.03</b>	<b>0.09</b>	<b>0.27</b>	<b>0.00</b>	<b>0.79</b>	<b>0.79</b>	<b>0.01</b>	<b>42.57</b>	<b>14.62</b>	<b>42.81</b>	<b>74.47</b>
SSMG7-Pyx1	2.21	1.98	0.03	0.09	0.26	0.00	0.80	0.79	0.00	43.12	14.06	42.82	75.41
SSMG7-Pyx2	2.22	1.99	0.02	0.07	0.27	0.00	0.81	0.80	0.00	43.13	14.46	42.41	74.88
SSMG7-Pyx2.1	2.22	1.98	0.03	0.08	0.27	0.00	0.78	0.81	0.00	41.81	14.42	43.77	74.36
SSMG7-Pyx3	2.22	1.98	0.02	0.08	0.27	0.00	0.79	0.81	0.02	42.21	14.38	43.42	74.59
SSMG7-Pyx4	2.22	1.98	0.03	0.09	0.32	0.00	0.83	0.71	0.00	44.57	17.01	38.43	72.38
SSMG7-Pyx5	2.21	1.99	0.03	0.08	0.27	0.00	0.77	0.81	0.00	41.58	14.46	43.96	74.20
SSMG7-Pyx6	2.21	1.98	0.02	0.09	0.26	0.00	0.79	0.81	0.00	42.37	13.90	43.73	75.29
SSMG7-Pyx7	2.22	1.97	0.03	0.09	0.27	0.00	0.79	0.81	0.02	42.34	14.25	43.41	74.82
SSMG7-Pyx8	2.22	1.97	0.03	0.09	0.28	0.00	0.78	0.80	0.00	41.97	14.89	43.13	73.81
SSMG7-Pyx9	2.22	1.98	0.03	0.09	0.28	0.00	0.78	0.80	0.00	41.89	14.85	43.26	73.83
SSMG7-Pyx10	2.22	1.96	0.03	0.10	0.27	0.00	0.78	0.82	0.00	41.78	14.55	43.67	74.18
SSMG7-Pyx10.1	2.21	1.97	0.03	0.10	0.26	0.00	0.80	0.81	0.00	42.76	13.82	43.43	75.58
SSMG7-Pyx11	2.21	2.01	0.00	0.06	0.25	0.00	0.82	0.81	0.00	43.61	13.44	42.95	76.44
SSMG7-Pyx11.1	2.21	1.97	0.03	0.09	0.26	0.00	0.78	0.81	0.00	42.29	13.87	43.85	75.31
SSMG7-Pyx12	2.21	1.99	0.03	0.07	0.27	0.00	0.81	0.78	0.00	43.48	14.50	42.02	74.99
<b>Average</b>	<b>2.22</b>	<b>1.98</b>	<b>0.03</b>	<b>0.08</b>	<b>0.27</b>	<b>0.00</b>	<b>0.79</b>	<b>0.80</b>	<b>0.00</b>	<b>42.59</b>	<b>14.46</b>	<b>42.95</b>	<b>74.67</b>
SSMG8-Pyx1	2.23	1.96	0.04	0.09	0.29	0.00	0.79	0.79	0.03	42.15	15.31	42.54	73.35
SSMG8-Pyx2	2.22	1.97	0.03	0.08	0.29	0.00	0.79	0.79	0.00	42.18	15.69	42.13	72.89
SSMG8-Pyx3	2.22	1.97	0.04	0.08	0.30	0.00	0.78	0.78	0.02	42.13	16.01	41.86	72.46
SSMG8-Pyx4	2.21	1.99	0.03	0.08	0.28	0.00	0.77	0.79	0.00	41.78	15.09	43.13	73.46
SSMG8-Pyx5	2.22	1.98	0.03	0.08	0.29	0.00	0.78	0.79	0.00	42.15	15.61	42.25	72.98
SSMG8-Pyx6	2.21	1.98	0.04	0.08	0.28	0.00	0.78	0.79	0.00	42.17	15.00	42.83	73.77
SSMG8-Pyx7	2.22	1.98	0.04	0.08	0.29	0.00	0.77	0.77	0.03	42.10	15.99	41.91	72.47
SSMG8-Pyx8	2.22	1.97	0.03	0.09	0.28	0.00	0.78	0.79	0.02	42.02	15.31	42.66	73.29

Appendix 2a: continued

Sample #	CAT SUM	Si	Ti	Al	Fe	Mn	Mg	Ca	Na	En	Fs	Wo	EN'
SSMG8-Pyx9	2.22	1.97	0.03	0.08	0.28	0.00	0.78	0.80	0.02	41.89	14.90	43.21	73.76
SSMG8-Pyx10	2.22	1.98	0.03	0.08	0.29	0.00	0.78	0.78	0.00	42.23	15.54	42.23	73.10
SSMG8-Pyx11	2.22	1.98	0.03	0.08	0.29	0.00	0.79	0.77	0.00	42.90	15.74	41.36	73.15
SSMG8-Pyx12	2.22	1.98	0.03	0.08	0.29	0.00	0.77	0.80	0.00	41.44	15.56	43.00	72.70
<b>Average</b>	2.22	1.98	0.03	0.08	0.29	0.00	0.78	0.79	0.01	42.09	15.48	42.43	73.12
SSMG9-Pyx1	2.20	2.02	0.01	0.04	0.24	0.00	0.82	0.81	0.00	43.75	12.96	43.29	77.14
SSMG9-Pyx1.1	2.21	1.99	0.02	0.08	0.26	0.00	0.78	0.81	0.00	42.15	14.14	43.71	74.89
SSMG9-Pyx2	2.22	1.97	0.04	0.09	0.26	0.00	0.78	0.81	0.00	42.00	14.23	43.77	74.70
SSMG9-Pyx3	2.23	1.97	0.03	0.09	0.27	0.00	0.75	0.83	0.02	40.68	14.72	44.60	73.43
SSMG9-Pyx4	2.22	1.99	0.03	0.08	0.26	0.00	0.76	0.81	0.02	41.58	14.46	43.96	74.20
SSMG9-Pyx5	2.22	1.97	0.03	0.09	0.27	0.00	0.77	0.81	0.00	41.48	14.78	43.74	73.74
SSMG9-Pyx6	2.22	1.97	0.04	0.09	0.28	0.00	0.78	0.79	0.00	41.81	15.33	42.85	73.17
SSMG9-Pyx7	2.23	1.96	0.04	0.10	0.28	0.00	0.75	0.81	0.03	40.83	15.16	44.02	72.93
SSMG9-Pyx8	2.22	1.97	0.03	0.09	0.28	0.00	0.77	0.78	0.02	42.02	15.28	42.70	73.34
SSMG9-Pyx9	2.22	1.96	0.04	0.09	0.27	0.00	0.77	0.83	0.00	41.35	14.40	44.25	74.17
SSMG9-Pyx10	2.22	1.97	0.03	0.09	0.26	0.00	0.77	0.83	0.00	41.12	14.16	44.72	74.38
SSMG9-Pyx10.1	2.20	2.02	0.01	0.05	0.24	0.00	0.80	0.80	0.00	43.20	13.26	43.54	76.52
SSMG9-Pyx11	2.22	1.96	0.04	0.10	0.28	0.00	0.76	0.79	0.02	41.41	15.48	43.11	72.78
SSMG9-Pyx12	2.22	1.98	0.03	0.08	0.27	0.00	0.76	0.82	0.00	41.02	14.83	44.15	73.45
<b>Average</b>	2.22	1.98	0.03	0.08	0.27	0.00	0.77	0.81	0.01	41.74	14.51	43.74	74.20
SSV1-Pyx1	2.24	1.94	0.05	0.12	0.36	0.00	0.75	0.73	0.00	40.70	19.71	39.58	67.37
SSV1-Pyx2	2.25	1.94	0.05	0.12	0.37	0.00	0.72	0.74	0.03	39.35	20.29	40.35	65.97
SSV1-Pyx4	2.25	1.93	0.05	0.13	0.38	0.00	0.72	0.73	0.03	39.40	20.77	39.82	65.48
SSV1-Pyx5	2.23	2.00	0.03	0.06	0.38	0.00	0.76	0.71	0.00	40.98	20.56	38.46	66.60
SSV1-Pyx6	2.24	1.94	0.06	0.13	0.35	0.00	0.71	0.75	0.00	39.19	19.62	41.19	66.64
SSV1-Pyx7	2.26	1.90	0.07	0.15	0.40	0.00	0.69	0.76	0.00	37.39	21.61	41.00	63.37
SSV1-Pyx8	2.26	2.00	0.03	0.06	0.49	0.00	0.71	0.65	0.00	38.45	26.62	34.93	59.09
SSV1-Pyx9	2.25	1.93	0.05	0.13	0.37	0.00	0.69	0.76	0.03	37.98	20.33	41.69	65.13
SSV1-Pyx10	2.24	1.96	0.04	0.10	0.35	0.00	0.74	0.75	0.00	40.04	19.04	40.92	67.78
SSV1-Pyx11	2.24	1.92	0.05	0.13	0.36	0.00	0.73	0.76	0.00	39.51	19.57	40.93	66.88

Appendix 2a. continued

Sample #	CAT SUM	Si	Ti	Al	Fe	Mn	Mg	Ca	Na	En	Fs	Wo	EN'
SSV1-Pyx12	2.24	1.95	0.04	0.12	0.38	0.00	0.76	0.71	0.00	40.96	20.62	38.41	66.51
<b>Average</b>	<b>2.24</b>	<b>1.95</b>	<b>0.05</b>	<b>0.11</b>	<b>0.38</b>	<b>0.00</b>	<b>0.73</b>	<b>0.73</b>	<b>0.01</b>	<b>39.45</b>	<b>20.80</b>	<b>39.75</b>	<b>65.53</b>
SSV2-Pyx1	2.25	1.90	0.06	0.16	0.36	0.00	0.75	0.72	0.03	40.80	19.88	39.32	67.24
SSV2-Pyx2	2.24	1.94	0.05	0.13	0.35	0.00	0.74	0.75	0.00	40.25	18.89	40.86	68.06
SSV2-Pyx3	2.23	1.99	0.02	0.06	0.37	0.00	0.83	0.67	0.00	44.21	19.94	35.85	68.92
SSV2-Pyx4	2.23	1.95	0.04	0.12	0.35	0.00	0.75	0.74	0.00	40.59	19.08	40.33	68.02
SSV2-Pyx5	2.23	1.95	0.04	0.11	0.34	0.00	0.76	0.74	0.00	41.31	18.52	40.17	69.05
SSV2-Pyx6	2.24	1.96	0.04	0.10	0.40	0.00	0.75	0.71	0.00	40.36	21.52	38.12	65.22
SSV2-Pyx7	2.25	1.98	0.04	0.08	0.42	0.00	0.74	0.70	0.00	39.68	22.84	37.48	63.47
SSV2-Pyx8	2.24	1.95	0.04	0.11	0.37	0.00	0.75	0.74	0.00	40.46	19.84	39.70	67.09
SSV2-Pyx9	2.24	1.92	0.05	0.14	0.36	0.00	0.74	0.75	0.00	39.81	19.42	40.76	67.21
SSV2-Pyx10	2.24	1.93	0.05	0.12	0.34	0.00	0.75	0.76	0.03	40.65	18.51	40.84	68.71
SSV2-Pyx11	2.24	1.95	0.04	0.12	0.35	0.00	0.74	0.74	0.03	40.26	19.29	40.44	67.61
SSV2-Pyx12	2.23	2.01	0.03	0.04	0.39	0.00	0.80	0.69	0.00	42.47	20.86	36.67	67.06
<b>Average</b>	<b>2.24</b>	<b>1.95</b>	<b>0.04</b>	<b>0.11</b>	<b>0.37</b>	<b>0.00</b>	<b>0.76</b>	<b>0.73</b>	<b>0.01</b>	<b>40.90</b>	<b>19.88</b>	<b>39.21</b>	<b>67.30</b>
SSV3-Pyx1	2.24	1.97	0.03	0.09	0.40	0.00	0.77	0.68	0.00	41.79	21.50	36.71	66.03
SSV3-Pyx2	2.23	1.99	0.03	0.06	0.39	0.00	0.82	0.66	0.00	43.78	20.91	35.31	67.67
SSV3-Pyx3	2.24	1.96	0.04	0.08	0.36	0.00	0.76	0.73	0.02	41.04	19.63	39.33	67.64
SSV3-Pyx4	2.22	2.00	0.03	0.06	0.36	0.00	0.83	0.67	0.00	44.88	19.19	35.93	70.05
SSV3-Pyx5	2.23	1.96	0.04	0.11	0.35	0.00	0.75	0.74	0.00	40.77	19.06	40.17	68.14
SSV3-Pyx6	2.23	2.00	0.03	0.05	0.37	0.00	0.80	0.70	0.00	43.05	19.61	37.34	68.71
SSV3-Pyx7	2.25	1.91	0.05	0.15	0.38	0.00	0.75	0.71	0.03	40.50	20.67	38.83	66.21
SSV3-Pyx8	2.24	1.95	0.04	0.11	0.38	0.00	0.77	0.70	0.00	41.63	20.68	37.69	66.81
SSV3-Pyx9	2.25	1.98	0.04	0.07	0.43	0.00	0.72	0.70	0.00	38.80	23.19	38.01	62.59
SSV3-Pyx10	2.23	2.00	0.03	0.05	0.39	0.00	0.79	0.68	0.00	42.38	20.89	36.72	66.98
SSV3-Pyx11	2.24	1.92	0.05	0.15	0.38	0.00	0.74	0.71	0.00	40.50	20.80	38.69	66.06
SSV3-Pyx12	2.24	1.96	0.04	0.10	0.36	0.00	0.75	0.74	0.00	40.61	19.61	39.77	67.43
<b>Average</b>	<b>2.24</b>	<b>1.97</b>	<b>0.04</b>	<b>0.09</b>	<b>0.38</b>	<b>0.00</b>	<b>0.77</b>	<b>0.70</b>	<b>0.00</b>	<b>41.64</b>	<b>20.48</b>	<b>37.88</b>	<b>67.03</b>
SSV4-Pyx1	2.23	2.01	0.02	0.05	0.40	0.00	0.83	0.64	0.00	44.34	21.24	34.41	67.61

Appendix 2a. continued

Sample #	CAT SUM	Si	Ti	Al	Fe	Mn	Mg	Ca	Na	En	Fs	Wo	EN'
SSV4-Pyx2	2.22	2.00	0.02	0.05	0.37	0.00	0.84	0.65	0.00	45.12	20.00	34.88	69.29
SSV4-Pyx3	2.23	2.01	0.02	0.05	0.40	0.00	0.84	0.64	0.00	44.70	21.19	34.11	67.84
SSV4-Pyx4	2.22	2.00	0.02	0.06	0.36	0.00	0.85	0.66	0.00	45.58	19.13	35.29	70.44
SSV4-Pyx5	2.23	2.01	0.02	0.05	0.40	0.00	0.82	0.64	0.00	44.02	21.63	34.35	67.05
SSV4-Pyx6	2.25	1.96	0.04	0.10	0.40	0.00	0.76	0.71	0.00	40.52	21.63	37.85	65.19
SSV4-Pyx7	2.24	1.97	0.03	0.09	0.39	0.00	0.75	0.73	0.00	40.03	20.71	39.26	65.91
SSV4-Pyx8	2.24	1.97	0.03	0.09	0.42	0.00	0.80	0.64	0.00	43.13	22.62	34.25	65.60
SSV4-Pyx9	2.24	2.00	0.02	0.05	0.43	0.00	0.82	0.64	0.00	43.45	22.63	33.92	65.76
SSV4-Pyx10	2.24	1.97	0.03	0.09	0.38	0.00	0.77	0.71	0.00	41.54	20.62	37.84	66.82
SSV4-Pyx11	2.22	1.99	0.02	0.07	0.36	0.00	0.85	0.67	0.00	45.13	18.97	35.90	70.41
SSV4-Pyx12	2.23	1.96	0.04	0.10	0.37	0.00	0.75	0.73	0.00	40.53	19.90	39.57	67.07
<b>Average</b>	<b>2.23</b>	<b>1.99</b>	<b>0.03</b>	<b>0.07</b>	<b>0.39</b>	<b>0.00</b>	<b>0.81</b>	<b>0.67</b>	<b>0.00</b>	<b>43.18</b>	<b>20.86</b>	<b>35.97</b>	<b>67.42</b>
SSV5-Pyx1	2.25	1.96	0.04	0.09	0.41	0.00	0.73	0.72	0.00	39.53	21.95	38.52	64.30
SSV5-Pyx2	2.24	1.97	0.03	0.08	0.37	0.00	0.78	0.72	0.00	41.70	19.74	38.56	67.87
SSV5-Pyx3	2.26	1.99	0.03	0.07	0.50	0.00	0.74	0.61	0.00	40.01	27.17	32.81	59.55
SSV5-Pyx4	2.25	1.98	0.03	0.08	0.42	0.00	0.73	0.70	0.00	39.60	22.65	37.75	63.62
SSV5-Pyx5	2.24	1.98	0.04	0.08	0.40	0.00	0.77	0.68	0.00	41.36	21.83	36.81	65.45
SSV5-Pyx6	2.28	2.00	0.03	0.05	0.53	0.00	0.63	0.70	0.00	33.94	28.39	37.67	54.44
SSV5-Pyx7	2.25	1.97	0.04	0.09	0.41	0.00	0.73	0.71	0.00	39.51	22.11	38.38	64.12
SSV5-Pyx8	2.23	1.97	0.04	0.09	0.37	0.00	0.78	0.70	0.00	42.06	20.11	37.83	67.65
SSV5-Pyx9	2.25	1.94	0.05	0.11	0.42	0.00	0.72	0.71	0.00	38.91	22.55	38.54	63.31
SSV5-Pyx10	2.25	1.99	0.04	0.06	0.47	0.00	0.75	0.62	0.00	40.71	25.61	33.68	61.39
SSV5-Pyx11	2.23	1.97	0.03	0.08	0.38	0.00	0.81	0.68	0.00	43.40	20.15	36.45	68.29
SSV5-Pyx12	2.23	1.98	0.04	0.08	0.36	0.00	0.78	0.71	0.00	42.18	19.53	38.29	68.35
<b>Average</b>	<b>2.25</b>	<b>1.98</b>	<b>0.04</b>	<b>0.08</b>	<b>0.42</b>	<b>0.00</b>	<b>0.75</b>	<b>0.69</b>	<b>0.00</b>	<b>40.24</b>	<b>22.65</b>	<b>37.11</b>	<b>64.03</b>
SSV6-Pyx1	2.25	1.93	0.05	0.13	0.38	0.00	0.67	0.79	0.00	36.60	20.66	42.74	63.92
SSV6-Pyx2	2.26	1.97	0.04	0.09	0.42	0.00	0.68	0.75	0.00	36.69	22.58	40.73	61.90
SSV6-Pyx3	2.25	1.94	0.05	0.12	0.38	0.00	0.69	0.77	0.03	37.51	20.69	41.80	64.45
SSV6-Pyx4	2.26	1.94	0.05	0.11	0.40	0.00	0.68	0.77	0.00	36.71	21.54	41.76	63.02
SSV6-Pyx5	2.26	1.95	0.05	0.10	0.40	0.00	0.67	0.76	0.03	36.41	22.01	41.58	62.33

Appendix 2a: continued

Sample #	CAT SUM	Si	Ti	Al	Fe	Mn	Mg	Ca	Na	En	Fs	Wo	EN'
SSV6-Pyx6	2.26	1.94	0.05	0.11	0.39	0.00	0.68	0.77	0.03	36.80	21.18	42.02	63.47
SSV6-Pyx7	2.27	1.92	0.05	0.12	0.40	0.00	0.67	0.79	0.03	36.20	21.35	42.45	62.90
SSV6-Pyx8	2.27	1.97	0.05	0.08	0.46	0.00	0.64	0.75	0.00	34.74	24.68	40.58	58.47
SSV6-Pyx9	2.28	1.98	0.04	0.07	0.49	0.00	0.62	0.75	0.00	33.28	26.42	40.29	55.74
SSV6-Pyx10	2.27	1.99	0.03	0.07	0.48	0.00	0.62	0.73	0.03	33.97	26.05	39.98	56.60
SSV6-Pyx11	2.26	1.93	0.05	0.12	0.39	0.00	0.68	0.76	0.03	37.16	21.43	41.41	63.42
SSV6-Pyx12	2.26	1.94	0.05	0.11	0.41	0.00	0.68	0.76	0.00	36.76	22.02	41.21	62.54
<b>Average</b>	<b>2.26</b>	<b>1.95</b>	<b>0.05</b>	<b>0.10</b>	<b>0.42</b>	<b>0.00</b>	<b>0.67</b>	<b>0.76</b>	<b>0.01</b>	<b>36.07</b>	<b>22.55</b>	<b>41.38</b>	<b>61.56</b>
SSV7-Pyx1	2.24	1.93	0.05	0.13	0.31	0.00	0.74	0.78	0.03	40.32	17.14	42.54	70.17
SSV7-Pyx2	2.24	1.97	0.04	0.09	0.36	0.00	0.74	0.75	0.00	39.75	19.61	40.64	66.96
SSV7-Pyx3	2.24	1.93	0.05	0.12	0.35	0.00	0.75	0.73	0.03	41.08	19.10	39.82	68.26
SSV7-Pyx4	2.23	1.99	0.03	0.06	0.36	0.00	0.82	0.69	0.00	43.82	19.39	36.79	69.32
SSV7-Pyx5	2.24	1.94	0.05	0.12	0.35	0.00	0.74	0.74	0.03	40.30	19.00	40.70	67.96
SSV7-Pyx6	2.24	1.92	0.05	0.15	0.33	0.00	0.72	0.77	0.03	39.70	18.20	42.10	68.57
SSV7-Pyx7	2.23	1.99	0.03	0.05	0.36	0.00	0.80	0.71	0.00	42.87	19.08	38.05	69.20
SSV7-Pyx8	2.24	1.92	0.06	0.14	0.35	0.00	0.74	0.73	0.03	40.52	19.36	40.12	67.66
SSV7-Pyx9	2.24	1.93	0.05	0.13	0.33	0.00	0.74	0.76	0.03	40.08	18.24	41.68	68.72
SSV7-Pyx10	2.24	1.94	0.05	0.12	0.36	0.00	0.75	0.73	0.00	40.92	19.43	39.65	67.81
SSV7-Pyx11	2.23	1.94	0.05	0.12	0.33	0.00	0.75	0.77	0.00	40.67	17.71	41.62	69.66
SSV7-Pyx12	2.24	1.95	0.05	0.10	0.34	0.00	0.75	0.76	0.00	40.67	18.47	40.86	68.77
<b>Average</b>	<b>2.24</b>	<b>1.94</b>	<b>0.05</b>	<b>0.11</b>	<b>0.35</b>	<b>0.00</b>	<b>0.75</b>	<b>0.74</b>	<b>0.01</b>	<b>40.89</b>	<b>18.73</b>	<b>40.38</b>	<b>68.59</b>

## Appendix 2b: SEM-EDS Analyses - Olivine

Sample #	CAT SUM	Si	Fe	Mn	Mg	Fo
SSMG2C-OI1	1.71	1.05	0.98	0.02	0.90	47.88
SSMG2C-OI2	1.71	1.05	0.98	0.01	0.92	48.49
SSMG2C-OI3	1.71	1.04	0.99	0.00	0.92	48.24
SSMG2C-OI4	1.72	1.04	0.99	0.02	0.92	48.04
SSMG2C-OI5	1.72	1.04	1.01	0.00	0.90	47.22
<b>Average</b>	<b>1.71</b>	<b>1.04</b>	<b>0.99</b>	<b>0.01</b>	<b>0.91</b>	<b>47.97</b>
SSMG3B-OI1	1.65	1.04	0.78	0.01	1.13	59.18
SSMG3B-OI2	1.64	1.05	0.76	0.00	1.14	59.83
SSMG3B-OI3	1.63	1.04	0.75	0.00	1.18	61.25
SSMG3B-OI4	1.65	1.04	0.77	0.01	1.15	59.99
SSMG3B-OI5	1.66	1.04	0.81	0.01	1.11	57.82
<b>Average</b>	<b>1.65</b>	<b>1.04</b>	<b>0.77</b>	<b>0.01</b>	<b>1.14</b>	<b>59.62</b>
SSMG4-OI1	1.64	1.04	0.75	0.00	1.18	61.01
SSMG4-OI2	1.64	1.05	0.77	0.00	1.13	59.48
SSMG4-OI3	1.63	1.03	0.73	0.01	1.19	62.05
SSMG4-OI4	1.63	1.04	0.75	0.00	1.17	60.94
SSMG4-OI5	1.64	1.03	0.74	0.01	1.19	61.55
<b>Average</b>	<b>1.64</b>	<b>1.04</b>	<b>0.75</b>	<b>0.00</b>	<b>1.17</b>	<b>61.01</b>
SSMG5-OI1	1.62	1.04	0.71	0.00	1.21	62.90
SSMG5-OI2	1.63	1.04	0.72	0.00	1.20	62.42
SSMG5-OI3	1.62	1.04	0.71	0.00	1.20	62.86
SSMG5-OI4	1.63	1.04	0.73	0.00	1.19	62.16
SSMG5-OI5	1.61	1.04	0.68	0.00	1.25	64.99
<b>Average</b>	<b>1.62</b>	<b>1.04</b>	<b>0.71</b>	<b>0.00</b>	<b>1.21</b>	<b>63.07</b>
SSMG6B-OI1	1.63	1.04	0.73	0.00	1.19	61.97
SSMG6B-OI2	1.63	1.04	0.74	0.00	1.19	61.52
SSMG6B-OI3	1.63	1.03	0.74	0.00	1.19	61.57
SSMG6B-OI4	1.63	1.04	0.73	0.00	1.18	61.82
SSMG6B-OI5	1.64	1.04	0.76	0.00	1.16	60.29
<b>Average</b>	<b>1.63</b>	<b>1.04</b>	<b>0.74</b>	<b>0.00</b>	<b>1.18</b>	<b>61.44</b>
SSMG7-OI1	1.64	1.03	0.74	0.00	1.20	61.66
SSMG7-OI2	1.63	1.04	0.74	0.00	1.19	61.84
SSMG7-OI3	1.63	1.03	0.73	0.00	1.20	62.02
SSMG7-OI4	1.64	1.04	0.75	0.00	1.17	60.97
SSMG7-OI5	1.64	1.04	0.75	0.00	1.18	61.13
<b>Average</b>	<b>1.63</b>	<b>1.04</b>	<b>0.74</b>	<b>0.00</b>	<b>1.19</b>	<b>61.52</b>
SSMG8-OI1	1.62	1.03	0.70	0.00	1.23	63.76
SSMG8-OI2	1.61	1.04	0.66	0.00	1.27	65.77
SSMG8-OI3	1.63	1.03	0.71	0.00	1.22	62.96
SSMG8-OI4	1.61	1.03	0.66	0.00	1.27	65.84
SSMG8-OI5	1.61	1.04	0.68	0.00	1.24	64.53
<b>Average</b>	<b>1.62</b>	<b>1.04</b>	<b>0.68</b>	<b>0.00</b>	<b>1.25</b>	<b>64.57</b>
SSMG9-OI1	1.63	1.04	0.74	0.00	1.18	61.34
SSMG9-OI2	1.63	1.04	0.74	0.00	1.18	61.48
SSMG9-OI3	1.63	1.05	0.72	0.00	1.18	61.95
SSMG9-OI4	1.63	1.04	0.74	0.00	1.18	61.56
SSMG9-OI5	1.63	1.03	0.74	0.00	1.19	61.55
<b>Average</b>	<b>1.63</b>	<b>1.04</b>	<b>0.74</b>	<b>0.00</b>	<b>1.18</b>	<b>61.58</b>

**Appendix 3a.** Whole rock geochemical data for DLS chill and UCZ samples. Major oxides reported in percentages, all others in ppm.

Sample	SSC1A	SSC1B	SSC1C	SSC1D	SSC2A	SSC2B	SSC3A	SSC3B	SSC3C	SSC4	SSC5
SiO2	49.33	44.1	48.57	48.83	46.82	49.83	48.07	50.1	48.49	49.49	49.23
Al2O3	12.89	12.93	13.8	12.21	11.81	11.59	13.57	12.99	12.66	13.19	13.44
Fe2O3*	15.69	18.91	14.89	16.83	19.8	17.95	14.93	14.55	15.77	15.15	14.54
MgO	4.83	4.33	5.25	3.97	3.41	3.21	6.31	4.68	4.6	4.86	5.15
CaO	8.66	8.49	8.72	8.02	7.77	7.33	8.17	8.64	6.42	8.23	8.69
Na2O	2.85	2.82	2.88	2.67	2.92	2.79	2.71	2.73	3.04	3.02	3.06
K2O	1	1.45	0.85	1.6	1.32	1.89	0.61	1.44	1.54	1.49	1.11
TiO2	3.37	3.7	3.08	3.9	3.41	3.38	2.91	3.17	3.53	3.21	3.05
P2O5	0.58	1.18	0.53	0.73	1.5	1.09	0.47	0.53	0.63	0.47	0.5
MnO	0.23	0.24	0.21	0.25	0.29	0.25	0.25	0.22	0.27	0.22	0.19
Cr2O3	0.013	0.005	0.013	0.006	<0.002	<0.002	0.019	0.017	0.011	0.013	0.014
Ni	74	30	85	32	<20	<20	95	50	46	61	79
Sc	35	38	32	36	32	33	33	36	35	34	33
Ba	393	435	265	414	504	549	276	347	631	522	255
Be	<1	5	5	4	1	5	3	<1	5	2	<1
Co	41.5	41.3	43	37.4	39.1	35.7	46.3	38.3	37.3	39.3	45.3
Cs	2	4.4	2	2	2.3	3.2	0.9	2.6	1.2	3.3	2.5
Ga	22.5	23.6	22.7	23.3	24.1	25	22	20.9	21.5	21.3	20.7
Hf	9.7	7.4	8.3	11.8	11	14.5	7.7	9.3	11.4	9.3	8.4
Nb	28.1	36.4	24.4	37.3	38	44.2	22.4	25.4	30.9	25.8	24
Rb	35.2	74.7	35	52.8	42.1	68.8	18.2	57.7	55.3	55.7	50.8
Sn	3	3	3	4	4	5	3	3	4	2	3
Sr	227.2	252.3	225	251.3	251.5	219.1	228.1	236.8	205.5	238.2	229
Ta	1.8	2.5	1.5	2.1	2.4	2.7	1.4	1.9	2	1.4	1.3
Th	5.3	3.2	4.8	6.3	6.7	9.1	4.8	5.9	6.8	4.7	5.4
U	1.5	1.3	1.4	1.9	1.9	2.7	1.5	2	1.9	1.7	1.7
V	336	270	298	299	135	231	299	316	318	323	313
W	<0.5	1	0.9	0.6	1.4	0.7	<0.5	0.6	1	<0.5	0.6
Zr	407.3	294.9	358.5	489.5	470.5	603.4	320.6	385.8	471.3	382	375.7
Y	64.5	82.8	52.9	77.4	94.2	98.7	50.9	59.4	68.4	60.1	53.4
La	46.8	54.7	39.3	50	69.9	71.9	34.3	42.4	49.3	41.6	38.3
Ce	96.1	125	79.9	112.1	147.4	154.1	75.4	90.4	106.5	89.8	81
Pr	12.58	17.69	10.9	14.97	20.51	20.52	9.93	11.8	14.31	11.63	10.61
Nd	53.6	77.6	45.5	66.1	87.5	88.9	42.8	51.3	59.6	51.2	44.9
Sm	12.17	17.68	10.82	15.16	20.46	20.16	10.02	11.46	13.39	11.07	10.47
Eu	3.02	4.24	2.62	3.41	4.6	4.81	2.51	2.7	3.42	2.58	2.61
Gd	13.26	19.38	11.44	16.07	20.81	21.39	10.33	12.33	14.22	11.71	11.52
Tb	2.18	2.97	1.87	2.63	3.45	3.51	1.75	2.08	2.34	1.99	1.87
Dy	13.06	17.22	11.03	15.2	19.44	19	9.64	12.05	14.1	11.82	10.38
Ho	2.57	3.25	2.13	2.87	3.58	3.72	1.92	2.31	2.68	2.28	2.03
Er	6.84	8.65	5.89	8.57	10.11	10.3	5.66	6.23	7.2	6.55	5.8
Tm	0.99	1.17	0.83	1.22	1.36	1.48	0.78	0.87	1.04	0.84	0.83
Yb	6.43	7.26	5.28	7.43	8.52	9.53	5.26	5.84	6.97	6.06	5.21
Lu	0.98	1.12	0.79	1.11	1.25	1.45	0.73	0.91	0.97	0.91	0.82
Mo	0.9	1.6	0.7	2.2	1.6	2	0.9	1	0.9	0.7	0.7
Cu	257	173.4	248.1	445.6	297.1	370.3	260	248.2	347.3	221.2	288.9
Pb	4.8	2.4	2.8	8.2	4.8	5.3	2	3.9	6.5	3.5	4.7
Zn	93	77	94	88	135	102	60	75	116	74	59
Ni	34.7	26.2	50.6	18.2	5.4	9.7	52.9	29.2	35.4	37.2	45.7
As	1.3	<0.5	1.5	0.5	1.8	3	<0.5	1.4	1.1	<0.5	2.2
Cd	0.1	<0.1	0.2	<0.1	0.3	0.2	<0.1	<0.1	<0.1	<0.1	<0.1
Sb	<0.1	<0.1	<0.1	<0.1	<0.1	0.1	<0.1	<0.1	<0.1	<0.1	<0.1
Bi	<0.1	<0.1	<0.1	<0.1	<0.1	<0.1	<0.1	<0.1	<0.1	<0.1	<0.1
Ag	<0.1	<0.1	<0.1	<0.1	<0.1	<0.1	<0.1	<0.1	<0.1	<0.1	<0.1
Au	<0.5	<0.5	1.4	2.8	1	1.8	1.5	0.6	1.1	0.7	0.9
Hg	<0.01	<0.01	0.01	<0.01	<0.01	<0.01	<0.01	<0.01	<0.01	<0.01	<0.01
Tl	0.1	0.2	0.1	<0.1	<0.1	<0.1	<0.1	0.1	<0.1	<0.1	0.1
Se	0.7	1.1	<0.5	1.7	1	0.9	0.5	<0.5	<0.5	0.8	<0.5



Appendix 3a. continued

Sample	SSC6	SSC7	SSC8	SSC9A	SSC9B	SSC9C	SSC10A	SSC10B	SSC10C	SSC11	SSC12
SiO2	45.17	42.35	42.21	43.15	46.38	47.84	49.43	42.84	46.78	49.71	48.5
Al2O3	15.1	10.95	11.27	11.65	13.37	13.6	12.62	11.64	11.61	15.39	14.61
Fe2O3*	17.16	23.29	22.23	19.73	15.48	14.52	14.52	19.88	18.58	13.54	14.34
MgO	6.3	4.31	4.9	5.95	6.84	6.59	5.28	4.83	4.63	4.92	5.17
CaO	10.44	10.04	10.32	10.68	10.51	9.97	9.43	9.84	8.95	9.27	8.85
Na2O	2.66	2.5	2.36	2.3	2.48	2.49	2.77	2.57	2.85	2.87	2.85
K2O	0.13	0.58	0.33	0.39	0.41	0.76	1.2	0.56	0.86	1.04	1.23
TiO2	2.6	4.49	5.14	4.84	3.45	2.91	3.32	4.99	4.62	2.78	3
P2O5	<0.01	1.47	1.11	0.69	0.29	0.33	0.48	0.99	0.87	0.45	0.49
MnO	0.22	0.31	0.3	0.25	0.21	0.2	0.2	0.26	0.25	0.18	0.2
Cr2O3	0.021	0.002	0.002	0.011	0.031	0.033	0.027	0.007	0.008	0.014	0.015
Ni	86	25	41	64	105	103	55	41	49	89	85
Sc	36	44	50	48	39	38	42	44	41	30	31
Ba	114	282	261	189	169	250	335	241	348	313	347
Be	<1	<1	<1	<1	<1	<1	3	<1	<1	<1	3
Co	60.7	48.5	48.1	55.6	52.9	48.8	39.4	47.3	43.5	42.2	40.2
Cs	0.3	0.6	0.3	1	0.8	0.7	2	1	1.2	1.5	2.3
Ga	23.6	24.4	22.4	20.2	17.6	18.4	21.1	21.7	20.9	21.1	20.8
Hf	0.3	5.6	5.2	3.8	3.2	5.6	7.9	8.4	9.8	7.8	7.7
Nb	0.4	30.7	39.5	23.8	15.3	16	23.4	34.4	33.6	21.4	22.9
Rb	1.5	13	3.9	11.4	11.6	21.8	42.8	18.5	24.4	38	44.6
Sn	<1	2	<1	<1	<1	1	3	2	3	3	3
Sr	449.3	262.2	261.6	254.3	255.2	268.2	232.6	222.3	233.8	259.8	267.4
Ta	<0.1	1.6	2.4	1.7	0.9	1.2	1.6	2.2	2.3	1.4	1.2
Th	<0.2	2.4	1	0.5	0.8	2.2	5.7	2.8	4.8	4.5	4.7
U	<0.1	0.6	0.3	0.3	0.4	0.7	1.8	0.8	1.4	1.2	1.2
V	561	288	422	513	398	367	360	422	398	277	296
W	<0.5	<0.5	<0.5	<0.5	<0.5	<0.5	0.6	<0.5	<0.5	<0.5	<0.5
Zr	8.6	221.8	198.6	133.5	135.9	216.2	314.9	317.4	366.7	304.5	323.6
Y	7.6	90.8	76.6	50.1	35.1	45	56.6	76.4	73.9	48.4	49.1
La	1.5	55.4	45.4	21.1	15	23	36.9	47.7	45.6	32.3	35
Ce	3.6	123	101.7	51	35.4	51.7	82.2	107.4	101.7	71.1	71.4
Pr	0.55	17.93	14.84	7.81	4.95	7.23	10.55	14.85	14.09	9.24	9.78
Nd	3.2	83.5	68.6	36.5	22.5	32.9	44.9	65.4	64.5	40.6	44.5
Sm	1.14	19.85	17.51	9.37	5.92	8.16	10.96	15.14	14.4	9.25	9.59
Eu	0.94	5.04	4.44	2.97	2	2.05	2.69	3.67	3.5	2.43	2.55
Gd	1.51	20.65	18.08	10.96	7.04	9.02	11.44	16.73	15.38	10.34	10.65
Tb	0.28	3.25	2.93	1.81	1.12	1.46	1.88	2.67	2.45	1.61	1.67
Dy	1.84	18.25	16.11	10.4	7.01	8.54	11.04	15.15	15.11	9.07	9.65
Ho	0.36	3.43	3.05	1.95	1.3	1.62	2.11	2.95	2.85	1.79	1.82
Er	0.84	9.28	7.74	5.59	3.57	4.49	5.66	7.75	7.29	5.25	5.12
Tm	0.12	1.22	1.11	0.78	0.54	0.63	0.88	1.15	1.13	0.72	0.81
Yb	0.77	7.48	6.87	4.44	3.25	4.37	5.33	7.19	6.68	4.47	4.79
Lu	0.11	1.11	1.04	0.73	0.54	0.65	0.78	1.09	1.06	0.67	0.69
Mo	<0.1	1.9	1.9	0.7	0.2	0.6	0.8	1.7	1.1	0.6	0.7
Cu	97.3	690.9	512.1	397.1	355.8	281.7	307.9	406.4	375.2	196	186
Pb	0.1	1.4	1	0.9	0.8	1.3	3	2	2	2.4	2.7
Zn	59	127	112	76	54	45	62	70	71	47	37
Ni	45.5	17.9	29.3	44.8	65.6	56.7	30	33.2	22	37.5	39.1
As	<0.5	<0.5	<0.5	1.9	<0.5	<0.5	1.6	0.7	0.7	0.6	0.6
Cd	<0.1	0.2	<0.1	<0.1	<0.1	<0.1	0.2	<0.1	0.1	<0.1	<0.1
Sb	<0.1	<0.1	<0.1	<0.1	<0.1	<0.1	<0.1	<0.1	<0.1	<0.1	0.1
Bi	<0.1	<0.1	<0.1	<0.1	<0.1	<0.1	<0.1	<0.1	<0.1	<0.1	<0.1
Ag	<0.1	0.2	0.1	0.1	<0.1	<0.1	<0.1	<0.1	<0.1	<0.1	<0.1
Au	9.9	<0.5	2.2	1.6	1.8	3.3	1.4	0.9	1.4	2.3	<0.5
Hg	<0.01	<0.01	<0.01	<0.01	<0.01	<0.01	<0.01	<0.01	<0.01	<0.01	<0.01
Tl	<0.1	<0.1	<0.1	<0.1	<0.1	<0.1	<0.1	<0.1	<0.1	<0.1	<0.1
Se	<0.5	1.1	0.5	<0.5	<0.5	<0.5	<0.5	<0.5	<0.5	<0.5	<0.5

**Appendix 3b:** Whole rock geochemical data for DLS microgabbro samples. Major oxides reported in percentages, all others in ppm.

Sample	SSMG1	SSMG 2A	SSMG 2B	SSMG 2C	SSMG 3A	SSMG3B	SSMG4	SSMG5	SSMG6A	SSMG6B	SSMG7	SSMG8	SSMG9
SiO2	46.02	42.03	42.09	41.60	41.70	42.49	41.22	37.05	43.81	45.63	42.74	40.42	40.54
Al2O3	9.91	11.72	11.71	11.29	12.95	13.26	12.45	10.09	14.06	17.51	13.13	13.10	12.94
Fe2O3*	12.85	18.94	18.66	19.83	15.74	15.63	16.84	22.32	16.49	11.39	18.10	16.09	16.68
MgO	9.21	6.67	6.72	6.50	7.93	7.27	7.87	11.07	11.10	7.35	12.56	8.32	8.64
CaO	14.64	11.00	11.15	11.33	10.51	10.88	10.68	7.82	8.41	10.29	7.53	10.22	10.03
Na2O	1.55	2.14	2.13	1.96	2.11	2.22	2.08	1.64	2.14	2.76	2.00	2.05	2.02
K2O	0.15	0.20	0.18	0.18	0.16	0.17	0.16	0.13	0.23	0.25	0.22	0.16	0.17
TiO2	4.58	7.20	7.32	7.06	8.61	8.00	8.49	10.29	3.23	4.01	2.70	8.83	9.03
P2O5	0.01	0.01	0.01	0.01	0.01	0.01	0.01	0.01	0.01	0.02	0.04	0.01	0.01
MnO	0.19	0.22	0.22	0.21	0.19	0.18	0.19	0.24	0.19	0.14	0.21	0.18	0.19
Cr2O3	0.05	0.01	0.01	0.01	0.03	0.03	0.03	0.06	0.08	0.05	0.09	0.04	0.05
Ni	151	70	68	68	157	168	151	283	309	185	366	191	199
Sc	79	57	59	62	51	52	52	45	26	30	23	49	50
Ba	53	66	71	70	65	64	62	47	81	92	135	61	68
Be	<1	<1	<1	<1	<1	<1	<1	2	<1	<1	1	<1	<1
Co	50.6	59.1	60.8	58	63.3	59.2	62	98.4	77	54.3	96.3	66.1	70.3
Cs	<0.1	<0.1	<0.1	<0.1	<0.1	<0.1	<0.1	<0.1	0.1	0.1	<0.1	<0.1	<0.1
Ga	12.7	17.6	17.7	18.2	14.2	15.9	14.1	11.5	14.6	18	13.3	14.2	13.9
Hf	1.5	1	1.3	1.1	1.2	1.5	1.5	1.7	0.9	0.9	0.9	1.5	1.5
Nb	5.4	7.4	9.7	7.2	11.2	9.6	10.8	12.1	3.6	5	3.9	10	10.3
Rb	1.1	1.7	1.4	1.1	0.8	0.6	0.7	0.7	3.2	2.1	3.5	1.2	1.1
Sn	<1	<1	<1	<1	<1	<1	<1	<1	<1	<1	<1	<1	<1
Sr	159.6	209.1	227.3	200.4	208.7	217.2	212.8	163.4	211.6	290.9	214.2	196.4	213.8
Ta	0.5	0.7	0.7	0.8	0.8	0.9	0.9	1.1	0.2	0.4	0.3	1.1	1
Th	<0.2	<0.2	<0.2	<0.2	<0.2	<0.2	<0.2	<0.2	<0.2	<0.2	0.3	<0.2	<0.2
U	<0.1	<0.1	<0.1	<0.1	<0.1	<0.1	<0.1	<0.1	<0.1	<0.1	<0.1	<0.1	<0.1
V	839	851	871	710	678	734	691	772	390	353	339	679	737
W	<0.5	<0.5	<0.5	<0.5	<0.5	<0.5	<0.5	<0.5	<0.5	<0.5	<0.5	<0.5	<0.5
Zr	44.8	27.4	38.6	33.1	47.8	42.8	45.6	52.8	29.2	29.7	33.2	43.3	47.3
Y	17.5	10.9	12.4	12.3	8.1	8.6	8.3	5.8	6.4	6.6	6.6	7.2	7.7
La	2.7	1.5	2	1.5	1.7	1.3	1.3	1.8	2.8	2.2	3.4	1.5	1.4
Ce	6.7	3.8	4.6	4.3	3.6	2.7	3.3	2.8	5.2	4.9	7.1	3.4	3.2
Pr	1.26	0.68	0.81	0.78	0.56	0.57	0.54	0.45	0.76	0.74	0.99	0.57	0.49

Appendix 3b: continued

Sample	SSMG1	SSMG 2A	SSMG 2B	SSMG 2C	SSMG 3A	SSMG3B	SSMG4	SSMG5	SSMG6A	SSMG6B	SSMG7	SSMG8	SSMG9
Nd	7.2	4.3	4.7	5	3	3.1	2.6	2.7	3.9	4	4.1	3.3	2.9
Sm	2.27	1.39	1.61	1.6	1.02	1.05	0.98	0.77	0.87	0.95	1.05	0.99	1.01
Eu	0.98	0.98	1.06	0.97	0.73	0.85	0.72	0.53	0.66	0.81	0.72	0.64	0.69
Gd	3.25	1.92	2.33	2.24	1.54	1.61	1.53	1.13	1.14	1.21	1.33	1.21	1.33
Tb	0.57	0.35	0.42	0.39	0.26	0.29	0.27	0.19	0.2	0.2	0.23	0.25	0.23
Dy	3.61	2.15	2.59	2.39	1.79	1.68	1.71	1.27	1.16	1.32	1.24	1.52	1.48
Ho	0.7	0.4	0.48	0.45	0.32	0.33	0.34	0.23	0.24	0.25	0.27	0.3	0.28
Er	1.81	1	1.42	1.18	0.96	0.86	0.89	0.74	0.78	0.68	0.77	0.82	0.78
Tm	0.28	0.15	0.18	0.19	0.12	0.12	0.14	0.09	0.08	0.1	0.09	0.13	0.1
Yb	1.63	0.96	1.06	1.11	0.82	0.88	0.79	0.69	0.59	0.61	0.63	0.79	0.82
Lu	0.26	0.15	0.21	0.18	0.14	0.14	0.13	0.1	0.1	0.1	0.11	0.1	0.13
Mo	<0.1	0.1	0.2	<0.1	<0.1	<0.1	<0.1	<0.1	0.2	0.1	<0.1	<0.1	<0.1
Cu	246.9	644	667.3	644.5	394.7	503.3	512.7	398.1	194.7	207.8	211.1	376.6	407.2
Pb	0.4	0.9	0.7	0.3	1.4	1.9	0.6	0.6	0.6	0.4	0.4	0.6	0.4
Zn	23	52	45	76	31	32	38	69	70	32	81	30	31
Ni	37.4	46	43.6	38.8	89	87	91.4	212.3	261.5	121.7	297.1	99.2	96.3
As	<0.5	<0.5	<0.5	<0.5	<0.5	0.5	<0.5	<0.5	<0.5	<0.5	0.9	<0.5	<0.5
Cd	<0.1	<0.1	<0.1	<0.1	<0.1	<0.1	<0.1	<0.1	<0.1	<0.1	<0.1	<0.1	<0.1
Sb	<0.1	<0.1	<0.1	<0.1	<0.1	<0.1	<0.1	<0.1	<0.1	<0.1	<0.1	<0.1	<0.1
Bi	<0.1	<0.1	<0.1	<0.1	<0.1	<0.1	<0.1	<0.1	<0.1	<0.1	<0.1	<0.1	<0.1
Ag	<0.1	0.2	0.1	0.1	0.1	0.2	0.2	0.2	<0.1	<0.1	<0.1	0.1	0.1
Au	6.2	1.1	0.9	<0.5	3.2	0.9	2.7	2.2	1.9	4.9	3.7	2.9	1.3
Hg	<0.01	<0.01	<0.01	<0.01	<0.01	<0.01	<0.01	<0.01	<0.01	<0.01	<0.01	<0.01	<0.01
Tl	<0.1	<0.1	<0.1	<0.1	<0.1	<0.1	<0.1	<0.1	<0.1	<0.1	<0.1	<0.1	<0.1
Se	<0.5	<0.5	<0.5	<0.5	<0.5	<0.5	<0.5	<0.5	<0.5	<0.5	<0.5	<0.5	<0.5

**Appendix 3c.** Whole rock geochemical data for NSVG samples. Major oxides reported in percentages, all others in ppm.

Sample	SSV1	SSV2	SSV3	SSV4	SSV5	SSV6	SSV7
SiO2	47.81	45.61	45.74	47.05	50.54	44.43	44.61
Al2O3	14.30	14.25	13.58	13.43	12.33	14.53	15.19
Fe2O3*	14.92	15.89	15.50	16.31	15.64	16.71	15.68
MgO	4.51	5.17	5.86	5.40	4.27	5.37	6.18
CaO	9.04	8.86	8.45	7.53	5.45	8.44	9.28
Na2O	2.51	2.45	2.15	2.35	3.61	2.47	2.24
K2O	0.98	0.86	0.79	1.25	2.09	0.66	0.38
TiO2	2.72	2.63	2.62	2.65	2.88	2.61	2.39
P2O5	0.61	0.28	0.26	0.29	0.33	0.30	0.23
MnO	0.23	0.27	0.22	0.18	0.20	0.22	0.15
Cr2O3	0.02	0.01	0.01	0.01	0.00	0.02	0.03
Ni	79.00	96.00	76.00	58.00	31.00	118.00	152.00
Sc	30.00	31.00	31.00	31.00	32.00	30.00	29.00
Ba	311.00	233.00	223.00	322.00	458.00	185.00	174.00
Be	2.00	1.00	1.00	1.00	1.00	1.00	2.00
Co	41.70	52.10	53.40	45.80	40.30	52.70	53.90
Cs	0.50	0.70	0.20	37.00	2.00	1.00	0.60
Ga	23.40	23.30	23.80	23.60	21.70	24.40	21.40
Hf	7.90	5.90	6.30	7.90	8.60	5.40	4.20
Nb	22.10	15.70	17.00	20.80	22.00	14.50	11.20
Rb	30.50	21.10	15.20	80.70	75.30	18.50	5.30
Sn	2.00	2.00	2.00	3.00	3.00	1.00	2.00
Sr	235.50	240.60	215.90	255.50	371.50	236.90	234.40
Ta	1.20	1.20	1.00	1.20	1.40	0.80	0.80
Th	4.20	3.00	3.20	4.40	5.30	1.90	1.60
U	1.30	1.10	1.10	1.40	1.60	0.70	0.50
V	215.00	301.00	285.00	298.00	278.00	223.00	274.00
W	0.70	0.50	0.50	0.50	0.60	0.50	0.50
Zr	314.60	235.00	256.30	309.60	327.30	212.50	167.80
Y	55.60	37.30	40.80	47.30	54.60	37.80	30.60
La	33.70	24.50	24.70	29.10	34.40	19.80	15.60
Ce	81.50	56.80	59.20	70.70	77.50	48.70	36.60
Pr	10.45	6.89	7.42	8.70	9.77	6.02	4.76
Nd	45.90	29.80	33.80	36.70	42.60	28.00	22.00
Sm	11.26	7.22	7.61	8.73	9.66	6.71	5.26
Eu	3.07	2.33	2.25	2.47	2.56	2.16	1.79
Gd	11.61	7.98	8.45	9.55	10.43	7.69	6.24
Tb	1.85	1.28	1.39	1.56	1.67	1.27	0.99
Dy	10.45	7.57	7.98	9.08	10.17	7.30	6.00
Ho	2.18	1.66	1.73	2.04	2.19	1.60	1.31
Er	6.36	4.52	4.90	5.45	6.00	4.41	3.48
Tm	0.87	0.64	0.67	0.82	0.85	0.63	0.53
Yb	5.44	3.98	4.33	5.16	5.68	4.13	3.05
Lu	0.88	0.61	0.68	0.74	0.84	0.62	0.49
Mo	1.10	0.80	0.40	0.70	0.50	0.60	0.20
Cu	150.20	52.90	57.60	208.40	99.00	72.60	119.00
Pb	3.90	4.40	2.70	6.10	6.30	2.10	1.20
Zn	89.00	107.00	92.00	115.00	123.00	87.00	73.00
Ni	49.70	63.50	49.60	37.00	17.10	103.10	120.40
As	1.40	0.70	<0.5	0.70	1.00	<0.5	<0.5
Cd	<0.1	<0.1	<0.1	<0.1	<0.1	<0.1	<0.1
Sb	<0.1	<0.1	<0.1	<0.1	<0.1	<0.1	<0.1
Bi	<0.1	<0.1	<0.1	<0.1	<0.1	<0.1	<0.1
Ag	<0.1	<0.1	<0.1	<0.1	<0.1	<0.1	<0.1
Au	1.50	5.10	3.30	2.00	4.00	2.70	4.20
Hg	<0.01	<0.01	<0.01	<0.01	<0.01	<0.01	<0.01
Tl	<0.1	<0.1	<0.1	<0.1	<0.1	<0.1	<0.1
Se	<0.5	<0.5	<0.5	<0.5	<0.5	<0.5	<0.5